A. Mutzke, X. Bonnin, J. Nührenberg, R. Schneider

Calculation of magnetic coordinates for stellarator fields

IPP 12/2
May 2003

Calculation of magnetic coordinates for stellarator fields

A. Mutzke, X. Bonnin, J. Nührenberg, R. Schneider

May 27, 2003

Abstract

We present an extension of the Nemov algorithm to compute magnetic coordinates in stellarators and their associated metric coefficients using only field line tracing, and covering not only the core of the plasma, but also island chains and scrape-off layer regions in the plasma edge. The algorithm is tested against both analytic and numerical benchmarks, and then applied on the full W7–X vacuum field geometry. The method has been optimized for numerical accuracy by minimizing recourse to derivatives of derived quantities. The only requirements are the foreknowledge of the magnetic field and its topological structure.

Contents

1 General algorithm

1.1 Goal and procedure

The magnetic coordinate system for a given magnetic field plays a fundamental role in the study of magnetic fields for plasmas in stellarator machines. For example, the 3-D plasma fluid modelling code `BoRiS` [1] is based on magnetic coordinates.

Here we give a brief overview of the method we are about to follow and give a listing of the quantities we are trying to compute. We then introduce sequentially each step to be taken and emphasize what quantities are known at the end of each of these steps. We use both a Cartesian (x, y, z) and a cylindrical coordinate system (R, φ, z) for the spatial variables. The Boozer coordinate system is noted (ψ, θ, ζ) and the `BoRiS` coordinate system (s, ϑ, ϕ). We assume the magnetic field (and only the magnetic field) is given on a cylindrical grid within a annular box domain $[\mathcal{B}]$ ranging over $[R_{min} \dots R_{max}; 0 \dots 2\pi; Z_{min} \dots Z_{max}]$. In essence, we will be mapping the spatial box $[\mathcal{B}]$ to $m + 1$ boxes in Boozer space, with m domains ranging over $\left[0 \dots F_T(\Psi_{sep}^{island}); 0 \dots 2\pi; 0 \dots 2\pi\right]$ for the islands and one domain, which includes both the core and SOL regions, covering $[0 \dots F_T(\Psi_{SOL}); 0 \dots 2\pi; 0 \dots 2\pi]$. These domains then will get renormalized into $m + (1 + \varepsilon_{SOL})$ unit cubes in `BoRiS` coordinates. This mapping and the calculation of the metric coefficients describing it are the goal of this work. We will thus compute:

- The rotational tranform: $\iota(\psi)$
- The flux surface function: $F_T \equiv \psi \to s$ and its radial derivative $\left.\dfrac{\partial F_T}{\partial R}\right|_{\substack{z=0 \\ \varphi=0}}^{\pm}$
- The flux surface derivatives: F_T' and F_P'
- The toroidal and poloidal currents: $J(\psi)$ and $I(\psi)$ respectively
- The Boozer and `BoRiS` Jacobians: $\mathcal{J}[\psi, \theta, \zeta]$ and $\sqrt{g}$
- The angle-like coordinates: $\theta = 2\pi\vartheta$ and $\chi \to \zeta = 2\pi\phi$
- The Clebsch vectors: $\nabla\psi$ and $(\nabla\theta - \iota\nabla\zeta)$
- Secondary metric coefficients: $\tilde{\beta}$, $\tilde{\sigma}$, $g_{\vartheta s}$, g^{ss}, $g^{\vartheta s}$ and $g^{\phi s}$.

In Step I, we define some of the indices used to refer to the flux surfaces and magnetic axes. In Step II, we do a first pass at field-line tracing, in which we find where the magnetic axes are, as well as identify the islands and SOL regions. This step also yields the χ toroidal-like coordinate. In Step III, we re-arrange the field-line data so as to define the flux surfaces. In Step IV, we compute the rotational transform ι. Step V yields the toroidal flux function F_T and its radial derivative. In Steps VI and VII respectively, we

calculate the toroidal (J) and poloidal (I) currents. In Step VIII, we deduce the angle-like coordinates θ, ϑ, ζ and ϕ. In Step IX, we resort to the Nemov algorithm in order to determine the Clebsch components of the field: $\nabla\psi$ and its conjugate $(\nabla\theta - \iota\nabla\zeta)$. In Step X, we obtain the ∇s and g^{ss} information. In Step XI, the Jacobians for both the Boozer and the `BoRiS` coordinate systems are calculated. Step XII takes care of determining the covariant component of the magnetic field, $\tilde{\beta}$. Finally, Step XIII gives the relations necessary to complete the set of needed physical quantities.

1.2 Step I: How many flux surfaces?

We define $N = N_c + m(N_i + 1) + N_s$ where m is the number of islands to be considered (from 4 to 6 in W7–X, depending on the ι value, but most commonly $m = 5$), and N_c, N_i and N_s are the number of flux surfaces we wish to determine in the core, one island, and the SOL, respectively. Typical values may be $N_c \sim 75$, $N_i \sim 25$ and $N_s \sim 10$, for an average distance of 5 mm between neighbouring flux surfaces. We then define the index Ψ to run from 0 to N. This will be the final flux surface index for all the arrays to follow in this Section. Since the actual position of the separatrix is not known *a priori*, the actual values of N_c, N_i and N_s are not pre-determined. See Step II for their evaluation. The index $\Psi = 0$ corresponds to the core magnetic axis, and m other axes are included for the islands by using $(N_i + 1)$ surfaces per island.

1.3 Step II: Following the field lines

We wish to define the flux surfaces by following one field line per flux surface, long enough so that the field line gives us enough Poincaré puncture points in the $(\varphi = 0)$ half-plane (or any other symmetry plane, e.g. for W7–X, $(\varphi = \pi/5)$ is also possible) to appropriately define the flux surface (see Step III). This may mean several hundred toroidal turns. This can however be reduced by a factor m (or N_{per}) if one takes advantage of the field symmetries. The number of field line following steps is thus a surface-dependent quantity and will be noted $N_{step}(\Psi)$. The position of the magnetic axes and X-points is found by minimizing the distance between two successive Poincaré puncture points. We then differentiate by hand between O- and X-points, using the knowledge that the core magnetic axis and one of the island axes are somewhere on the outer half of the $(\varphi = 0, z = 0)$ half-line (which we refer to as the "axes-line"). We then go around the plasma envelope alternating O- and X-points. Other geometries would lead to a different choice of "axes-line" and thus of field-line-following starting points. Along this "axes-line", we choose a resolution spacing ΔR, for example 5 mm, from which we start each flux surface field line.

We note the flux surface index Ψ. Then, we attempt to follow a field line. We set the starting point to be $(R_0 = R_{O_{pt}} + \Psi\Delta R; \varphi_0 = 0; z_0 = 0)$. As long as we can follow field lines for many toroidal turns without getting outside the box $[\mathcal{B}]$, we increment Ψ and

proceed from field line to field line. This procedure is done for the core flux surfaces and the outer island. In order to reach the other islands, we move the startpoints toroidally by multiples of $2\pi/m$. As we follow the field lines, we store the arrays:

$$\chi(\Psi, istep) = \chi(\Psi, istep-1) + \int_{istep-1}^{istep} \vec{B} \cdot d\vec{\ell} \cdots \text{with } \vec{\ell} \text{ along the field line;} \tag{1.1}$$

$$\Theta_p(\Psi, istep) = \text{number of poloidal turns made since start;} \tag{1.2}$$

$$\Phi_t(\Psi, istep) = \text{number of toroidal turns made since start.} \tag{1.3}$$

These arrays need only be stored at regular toroidal spacings, with a resolution $\Delta\varphi \equiv 2\pi/n_{tor}$, where, for example $n_{tor} \equiv 32 \times N_{per}$, and N_{per} is the number of toroidal field periods. In W7-X, we have $N_{per} = 5$. One should use a multiple of both m and N_{per} for n_{tor} so as to take advantage of the field symmetries. Since in most cases $m = N_{per}$, this is not a very limiting constraint. Then, formally: $N_{step}(\Psi) = n_{tor} \times \Phi_t\left(\Psi, N_{step}(\Psi)\right)$. This computation can be performed in parallel for each field line start point. Note, that the direction of fieldline defines the kind of magnetic coordinate system (left handed or right handed system).

1.4 Step III : Form flux surfaces

Using a least-squares approximation method, we can form the flux surfaces and obtain an ordered set of angles $\xi(\Psi) = \{\theta\left(\Psi, \Phi_t(\Psi, istep)\right)\}$ for each Poincaré section of a flux surface. This ordered set is chosen to be in the $(\varphi = 0)$ plane for simplicity and the curve it forms will be noted $C(\Psi)$. This step can be undertaken for each Ψ index value in parallel.

1.5 Step IV : Compute the rotational transform ι

For simplicity, we will use the relation:

$$\iota(\Psi) = \frac{\Theta_p\left(\Psi, N_{step}(\Psi)\right)}{\Phi_t\left(\Psi, N_{step}(\Psi)\right)}. \tag{1.4}$$

Here, the rotational transform ι is computed as a running average of the ratio above (see Section 2.3). This method guarantees an accuracy of at least $\Delta\theta/(2\pi\Phi_t)$, where we use $\Phi_t = 400$ and typically the individual angular excursion of a point $\Delta\theta$ is of the order of degrees. We have found this to be sufficient, with the possible exception of the immediate neighbourhood of small island chains within the core plasma (e.g. at $\iota = 10/11$), where adjustements by hand were necessary (see Section 2.8). Although other methods exist to compute ι, mostly through Fourier decomposition, they are either not adapted to the problem at hand, where one needs to compute ι across region boundaries, or do not provide significantly greater accuracy without significant additional effort.

1.6 Step V : Compute the toroidal flux function F_T

We can now compute the toroidal flux coordinate:

$$\psi \equiv F_T = \text{toroidal flux} = F_T(\Psi) = F_T(\Psi - 1) + \oint\limits_{C(\Psi)-C(\Psi-1)} \vec{B} \cdot d\vec{A}. \tag{1.5}$$

Thus, the toroidal flux is computed by adding the flux from the last enclosed flux surface already known and adding the contribution of the current plasma shell.

We may now compute the radial derivative $\left.\dfrac{\partial F_T}{\partial R}\right|^{\pm}_{\substack{z=0\\ \varphi=0}}$, which will be needed as an initial condition in the Nemov algorithm when computing $\nabla\psi$. This derivative is to be computed along the "axes-line" we chose for our starting points in the field-line tracing step (i.e. at $\theta = 0, -\pi$). Since we will use staggered flux surfaces for the Nemov step, we need to compute the radial derivative of F_T at the mid-points between our field-line tracing starting points.

1.7 Step VI : Compute the toroidal current J

Using Stokes' theorem and Maxwell's equations, one can readily obtain the toroidal current $J(\Psi)$:

$$\oint\limits_{C(\Psi)} \vec{B} \cdot d\vec{\ell} = \mu_0 J(\Psi), \tag{1.6}$$

where μ_0 is the magnetic permittivity of vacuum.

1.8 Step VII : Compute the poloidal current I

As above, but using a toroidal-like path loop, one can enclose the poloidal current $I(\Psi)$:

$$\oint\limits_{\Gamma(\Psi)} \vec{B} \cdot d\vec{\ell} = \mu_0 I(\Psi) = \int\limits_{\vec{R}_0(\Psi)}^{\vec{R}(\Psi,n_{tor})} \vec{B} \cdot d\vec{\ell} + \int\limits_{\vec{R}(\Psi,n_{tor})}^{\vec{R}_0(\Psi)} \vec{B} \cdot d\vec{\xi}(\Psi). \tag{1.7}$$

The toroidal path $\Gamma(\Psi)$ is constructed by starting at the flux surface Ψ at the point $\vec{R}_0(\Psi)$(in the $(\varphi = 0)$ plane), then following the field line once toroidally, ending at the point $\vec{R}(\Psi, n_{tor})$ and closing along the flux surface contour $\xi(\Psi)$ from Step III, towards $\vec{R}_0$ in the direction opposite to the projection of $\vec{B}$ in the $(\varphi = 0)$ plane.

1.9 Step VIII : Computation of $\mathcal{J}$

We turn now to the evaluation of the Jacobian $\mathcal{J}$ in Boozer coordinates, which we must also compute it for the `BoRiS` coordinate system. The appropriate relations are:

$$\mathcal{J}_{Boozer} \equiv \mathcal{J}[\psi,\theta,\zeta] = -\frac{(2\pi)^2 \cdot \mu_0(I+\iota J)\cdot\left(F_T(\Psi_{sep})\right)^2}{B^2}, \tag{1.8a}$$

$$\sqrt{g} \equiv \mathcal{J}_{BoRiS} \equiv \mathcal{J}[s,\vartheta,\phi] = \frac{\mathcal{J}[\psi,\theta,\zeta]}{(2\pi)^2 F_T(\Psi_{sep})} = -\frac{\mu_0(I+\iota J)F_T(\Psi_{sep})}{B^2}, \tag{1.8b}$$

where $F_T(\Psi_{sep})$ is the total toroidal flux enclosed within the relevant separatrix.

1.10 Step IX : Compute the angle-like coordinate pairs (θ,ζ) and (ϑ,ϕ)

We now have all the necessary pieces to define the θ, ζ, ϑ and ϕ coordinates:

$$\theta(\Psi,istep)/(2\pi) \equiv \vartheta(\Psi,istep) = \theta_0 + \frac{\iota(\Psi)\chi(\Psi,istep)}{\mu_0(I(\Psi)+\iota(\Psi)J(\Psi))} \pmod 1; \tag{1.9a}$$

$$\zeta(\Psi,istep)/(2\pi) \equiv \phi(\Psi,istep) = \frac{\chi(\Psi,istep)}{\mu_0(I(\Psi)+\iota(\Psi)J(\Psi))} \pmod 1; \tag{1.9b}$$

where θ_0 is the poloidal angle-like coordinate of the starting point of the field-line following, here $\theta_0 \equiv 0$. Having established those coordinates, we can now also build equivalency relations between space and magnetic coordinates (see Section 2.10).

1.11 Step X : Nemov algorithm

We now follow the Nemov algorithm [2], using the Clebsch description of the magnetic field: $\vec{B} = \nabla\psi \times (\nabla\theta - \iota\nabla\zeta)$. This will allow us to obtain the flux gradient $\nabla\psi$ as well as the angle gradient combination $(\nabla\theta - \iota\nabla\zeta)$. We define $P = \dfrac{\partial\psi}{\partial R}$, $Q = \dfrac{\partial\psi}{\partial\varphi}$, $G = \dfrac{\partial\psi}{\partial z}$, $U = \dfrac{\partial\theta}{\partial R} - \iota\dfrac{\partial\zeta}{\partial R}$, $V = \dfrac{\partial\theta}{\partial\varphi} - \iota\dfrac{\partial\zeta}{\partial\varphi}$ and $W = \dfrac{\partial\theta}{\partial z} - \iota\dfrac{\partial\zeta}{\partial z}$, such that:

$$\nabla\psi = P\hat{e}_R + \frac{Q}{R}\hat{e}_\varphi + G\hat{e}_z, \tag{1.10a}$$

$$\nabla\theta - \iota\nabla\zeta = U\hat{e}_R + \frac{V}{R}\hat{e}_\varphi + W\hat{e}_z. \tag{1.10b}$$

Then the following sets of differential equations hold:

$$\frac{dP}{d\varphi} = -\frac{R}{B_\varphi}\left(\frac{\partial B_R}{\partial R}P + \frac{\partial}{\partial R}\left(\frac{B_\varphi}{R}\right)Q + \frac{\partial B_z}{\partial R}G\right), \tag{1.11a}$$

$$\frac{dQ}{d\varphi} = -\frac{R}{B_\varphi}\left(\frac{\partial B_R}{\partial\varphi}P + \frac{1}{R}\frac{\partial B_\varphi}{\partial\varphi}Q + \frac{\partial B_z}{\partial\varphi}G\right), \tag{1.11b}$$

$$\frac{dG}{d\varphi} = -\frac{R}{B_\varphi}\left(\frac{\partial B_R}{\partial z}P + \frac{1}{R}\frac{\partial B_\varphi}{\partial z}Q + \frac{\partial B_z}{\partial z}G\right), \tag{1.11c}$$

$$\frac{dU}{d\varphi} = -\frac{R}{B_\varphi}\left(\frac{\partial B_R}{\partial R}U + \frac{\partial}{\partial R}\left(\frac{B_\varphi}{R}\right)V + \frac{\partial B_z}{\partial R}W\right), \tag{1.12a}$$

$$\frac{dV}{d\varphi} = -\frac{R}{B_\varphi}\left(\frac{\partial B_R}{\partial \varphi}U + \frac{1}{R}\frac{\partial B_\varphi}{\partial \varphi}V + \frac{\partial B_z}{\partial \varphi}W\right), \tag{1.12b}$$

$$\frac{dW}{d\varphi} = -\frac{R}{B_\varphi}\left(\frac{\partial B_R}{\partial z}U + \frac{1}{R}\frac{\partial B_\varphi}{\partial z}V + \frac{\partial B_z}{\partial z}W\right). \tag{1.12c}$$

We choose as initial conditions for $\nabla\psi$: $P_0 = \left.\frac{\partial F_T}{\partial R}\right|^{\pm}_{\substack{z=0\\ \varphi=0}}$ and $G_0 = 0$. The initial conditions for $(\nabla\theta - \iota\nabla\zeta)$ are, by the same token: $U_0 = 0$, $V_0 = RB_z \Big/ \left(\frac{\partial F_T}{\partial R}\right)\Big|^{\pm}_{\substack{z=0\\ \varphi=0}}$ and $W_0 = -B_\varphi \Big/ \left(\frac{\partial F_T}{\partial R}\right)\Big|^{\pm}_{\substack{z=0\\ \varphi=0}}$. These initial conditions correspond to the fact that at the starting points we chose, the magnetic field has no radial component by symmetry, hence the vector $\nabla\psi$ points in the radial direction and $(\nabla\theta - \iota\nabla\zeta)$ is tangent to an (R = cst) cylinder. In order to properly follow the equation sets (1.11)-(1.12), arrays of the relevant partial derivatives of $\vec{B}$ should be built beforehand. This step is expected to be the most computer-time intensive and can therefore be very advantageously parallelized. The starting points are chosen along the "axes-line" where the values of P_0, V_0 and W_0 are known, i.e. at the mid-points between the starting points used in Step II. For some geometries, for example the ring test case in Section 3, the second set of differential equations has a zero determinant and cannot be used (specifically the V equation collapses to $0 = 0$). Moreover, the numerical integration of these equations is numerically sensitive, as they are exponential in character and thus likely to be unstable. This is detailed in Section 2.9.

1.12 Step XI: Computation of ∇s and g^{ss}

In order to compute s, one need only divide ψ by the value it takes at the relevant separatrix (noted $F_T(\Psi_{sep})$), since s is normalized to run from 0 to 1. When computing ∇s, one obtains:

$$\nabla s = \frac{\nabla\psi}{F_T(\Psi_{sep})} \tag{1.13}$$

and thus

$$g^{ss} = \|\nabla s\|^2 = \frac{1}{F_T(\Psi_{sep})^2}\left(P^2 + \left(\frac{Q}{R}\right)^2 + G^2\right). \tag{1.14}$$

1.13 Step XII : Covariant component $\tilde{\beta} = \vec{B}\cdot\vec{e}_s$

We must also compute, in cases of non-zero plasma pressure (otherwise we have the trivial identity $\tilde{\beta} = 0$), the first covariant component of $\vec{B}$, noted $\tilde{\beta}$, which is the dot

product of the magnetic field vector with the covariant basis vector $\vec{e}_s$. We have, by definition:

$$\vec{e}_s = \frac{\partial \vec{R}}{\partial s} = \frac{\Delta R}{\Delta s}\hat{e}_R + R\frac{\Delta \varphi}{\Delta s}\hat{e}_\varphi + \frac{\Delta z}{\Delta s}\hat{e}_z. \tag{1.15}$$

$$\vec{e}_\vartheta = \frac{\partial \vec{R}}{\partial \vartheta} = \frac{\Delta R}{\Delta \vartheta}\hat{e}_R + R\frac{\Delta \varphi}{\Delta \vartheta}\hat{e}_\varphi + \frac{\Delta z}{\Delta \vartheta}\hat{e}_z. \tag{1.16}$$

The covariant basis vectors can be readily obtained from the coordinate equivalency relations deduced from Section 1.10.
Then, noting $\vec{e}_s = \tilde{x}\hat{e}_R + \tilde{y}R\hat{e}_\varphi + \tilde{z}\hat{e}_z$, we simply get $\tilde{\beta}$ as:

$$\tilde{\beta} = \vec{B} \cdot \vec{e}_s = \tilde{x}B_R + \tilde{y}RB_\varphi + \tilde{z}B_z. \tag{1.17}$$

1.14 Step XIII : Other constitutive relations

Now that we have the three independent quantities $\sqrt{g}$, g^{ss} and $(\nabla\theta - \iota\nabla\zeta)$ or $\tilde{\beta}$, we can now compute all the other quantities we need by using the following constitutive relations:

$$F'_T \equiv \frac{dF_T}{ds} = F_T(\Psi_{sep}), \tag{1.18a}$$

$$F'_P \equiv \frac{dF_P}{ds} = \iota F'_T = \iota F_T(\Psi_{sep}), \tag{1.18b}$$

$$g_{s\vartheta} = \vec{e}_\vartheta \cdot \vec{e}_s, \tag{1.19}$$

$$\tilde{\sigma} = -\frac{F'_T}{B}\left((\nabla\theta - \iota\nabla\zeta)\cdot\nabla s\right), \tag{1.20a}$$

$$\tilde{\sigma} = -\frac{1}{F'_T \cdot B}\left[B^2 \cdot g_{s\vartheta} - \mu_0 J \cdot \tilde{\beta}\right], \tag{1.20b}$$

$$g^{\phi s} = -\frac{F'_T \cdot \tilde{\beta} \cdot g^{ss} + J \cdot \tilde{\sigma} B}{\mu_0 (F'_T \cdot I + F'_P \cdot J)}, \tag{1.21a}$$

$$g^{\vartheta s} = -\frac{F'_P \cdot \tilde{\beta} \cdot g^{ss} - I \cdot \tilde{\sigma} B}{\mu_0 (F'_T \cdot I + F'_P \cdot J)}. \tag{1.21b}$$

2 Comparison with numerical results from the VMEC program

2.1 The magnetic field and fieldlinetracing

The assumption is that we have the components of a magnetic field (B_x, B_y, B_z) on a grid. R, φ, z are cylindrical coordinates.

$$B_x = f(R, \varphi, z) \quad B_y = f(R, \varphi, z) \quad B_z = f(R, \varphi, z) \tag{2.1}$$

The solutions of the following sets of differential equations give the fieldline of the magnetic field.

$$B_x = \frac{\partial x}{\partial h} \quad B_y = \frac{\partial y}{\partial h} \quad B_z = \frac{\partial z}{\partial h} \tag{2.2}$$

The fieldlines can be calculated with the help of the three-dimensional Runge-Kutta method. For the interpolation of components between the grid points, the method of cubic splines is used.

$$\begin{aligned} K_{1,x} &= \Delta h \cdot B_x(x_i, y_i, z_i) \\ K_{1,y} &= \Delta h \cdot B_y(x_i, y_i, z_i) \\ K_{1,z} &= \Delta h \cdot B_z(x_i, y_i, z_i) \end{aligned} \tag{2.3}$$

$$\begin{aligned} K_{2,x} &= \Delta h \cdot B_x\left(x_i + 0.5 \cdot K_{1,x}, y_i + 0.5 \cdot K_{1,y}, z_i + 0.5 \cdot K_{1,z}\right) \\ K_{2,y} &= \Delta h \cdot B_y\left(x_i + 0.5 \cdot K_{1,x}, y_i + 0.5 \cdot K_{1,y}, z_i + 0.5 \cdot K_{1,z}\right) \\ K_{2,z} &= \Delta h \cdot B_z\left(x_i + 0.5 \cdot K_{1,x}, y_i + 0.5 \cdot K_{1,y}, z_i + 0.5 \cdot K_{1,z}\right) \end{aligned} \tag{2.4}$$

$$\begin{aligned} K_{3,x} &= \Delta h \cdot B_x\left(x_i + 0.5 \cdot K_{2,x}, y_i + 0.5 \cdot K_{2,y}, z_i + 0.5 \cdot K_{2,z}\right) \\ K_{3,y} &= \Delta h \cdot B_y\left(x_i + 0.5 \cdot K_{2,x}, y_i + 0.5 \cdot K_{2,y}, z_i + 0.5 \cdot K_{2,z}\right) \\ K_{3,z} &= \Delta h \cdot B_z\left(x_i + 0.5 \cdot K_{2,x}, y_i + 0.5 \cdot K_{2,y}, z_i + 0.5 \cdot K_{2,z}\right) \end{aligned} \tag{2.5}$$

$$\begin{aligned} K_{4,x} &= \Delta h \cdot B_x\left(x_i + K_{3,x}, y_i + K_{3,y}, z_i + K_{3,z}\right) \\ K_{4,y} &= \Delta h \cdot B_y\left(x_i + K_{3,x}, y_i + K_{3,y}, z_i + K_{3,z}\right) \\ K_{4,z} &= \Delta h \cdot B_z\left(x_i + K_{3,x}, y_i + K_{3,y}, z_i + K_{3,z}\right) \end{aligned} \tag{2.6}$$

$$\begin{aligned} x_{i+1} &= x_i + \frac{1}{6}\left(K_{1,x} + K_{2,x} + K_{3,x} + K_{4,x}\right) \\ y_{i+1} &= y_i + \frac{1}{6}\left(K_{1,y} + K_{2,y} + K_{3,y} + K_{4,y}\right) \\ z_{i+1} &= z_i + \frac{1}{6}\left(K_{1,z} + K_{2,z} + K_{3,z} + K_{4,z}\right) \end{aligned} \tag{2.7}$$

If $\Delta h > 0$ the magnetic coordinate system is a left-handed system. Otherwise, we get a right-handed system.

Figure 1 shows the accuracy of the solution dependent on resolution and step value Δh of the Runge-Kutta method. The vacuum magnetic field of the W7–X stellarator (variant hs5v10u), was used. The grid distance has a range of 0.110 m to 0.013 m and the coefficient Δh has a variation of 0.5 to 0.001. If the resolution or the step value is too large then it is possible that the coordinates of fieldlines be calculated incorrectly or wrongly.

For the vacuum magnetic field of the W7–X stellarator (standard), the field components and the core separatrix position (as Fourier coefficients) are given.
The magnetic coordinates and Fourier coefficients were calculated with the 3-D ideal MHD equilibrium code `VMEC_2000`, the mapping (`JMC`) and the `interface_stability`. The `VMEC` program works with fixed boundary conditions. The input were the core separatrix position, the absolute value of the magnetic field at the magnetic axis at $\varphi = 0$ ($|B| = 3.13\ T$) and the stellarator geometry. This computation required a resolution of 500 radial grid points, 80 poloidal grid points and 60 toroidal grid points per period, 20 poloidal and 15 toroidal harmonics, in order to properly resolve the edge region

The input for the program `aam10` (the used methods are described in this paper) was only the magnetic field in cylindrical (R, φ, z) coordinate. The grid resolution of the magnetic field is $81 \times 124 \times 81$ points:

- 81 points between $R = 4.25$ m and $R = 6.45$ m ($\Delta R = 0.0275$ m)
- 124 points between $\varphi = 0$ and $\varphi = 2\pi/5$ ($r \cdot \Delta\varphi = 0.0430$ m $\ldots 0.0653$ m)
- 81 points between $z =$ -1.30 m and $z = 1.30$ m ($\Delta z = 0.0325$ m)

2.2 Calculation of Poincaré sections

A step value of $h = 0.0005$ for the Runge-Kutta method is used to calculate the fieldlines and points of Poincaré sections.
The closed Poincaré curves were calculated with the method of least-square approximation (Core with Fourier coefficients and islands with polynomials).
Figure 2.1 a shows the Poincaré section with the Poincaré puncture points at $\varphi = 0°$ and Figure 2.1 b shows only the Poincaré sections, calculated with 400 toroidal turns. The scrape-off layer surrounds the core and the five islands.
The comparison of the given core separatrix and the calculated separatrix with the program `aam10` is shown in Figure 2.1 c.

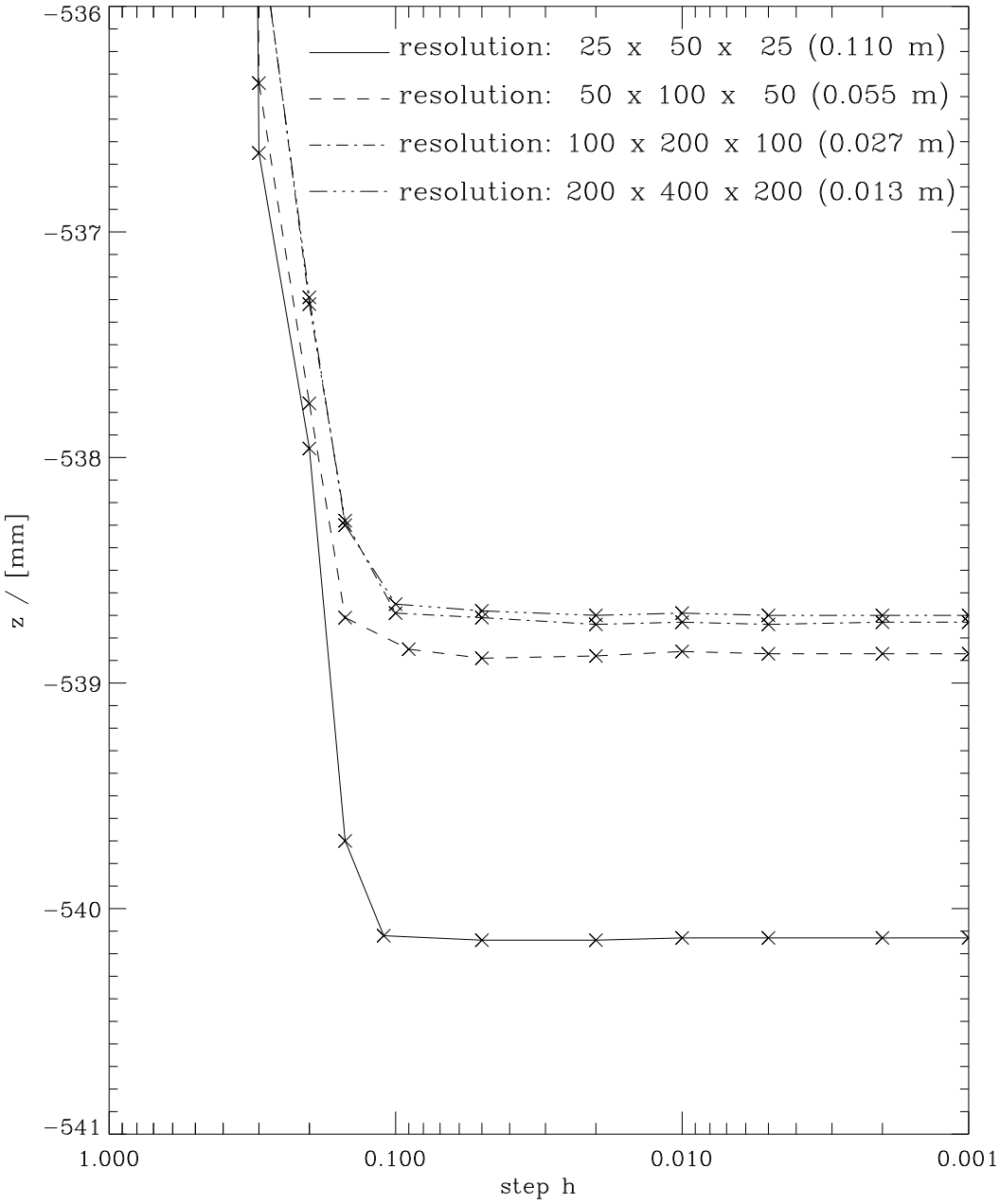

Fig. 1 Absolute endpoint (z) with variation of step h

10 turns (start: x = 6.1 m, y = 0 m, z = 0 m)

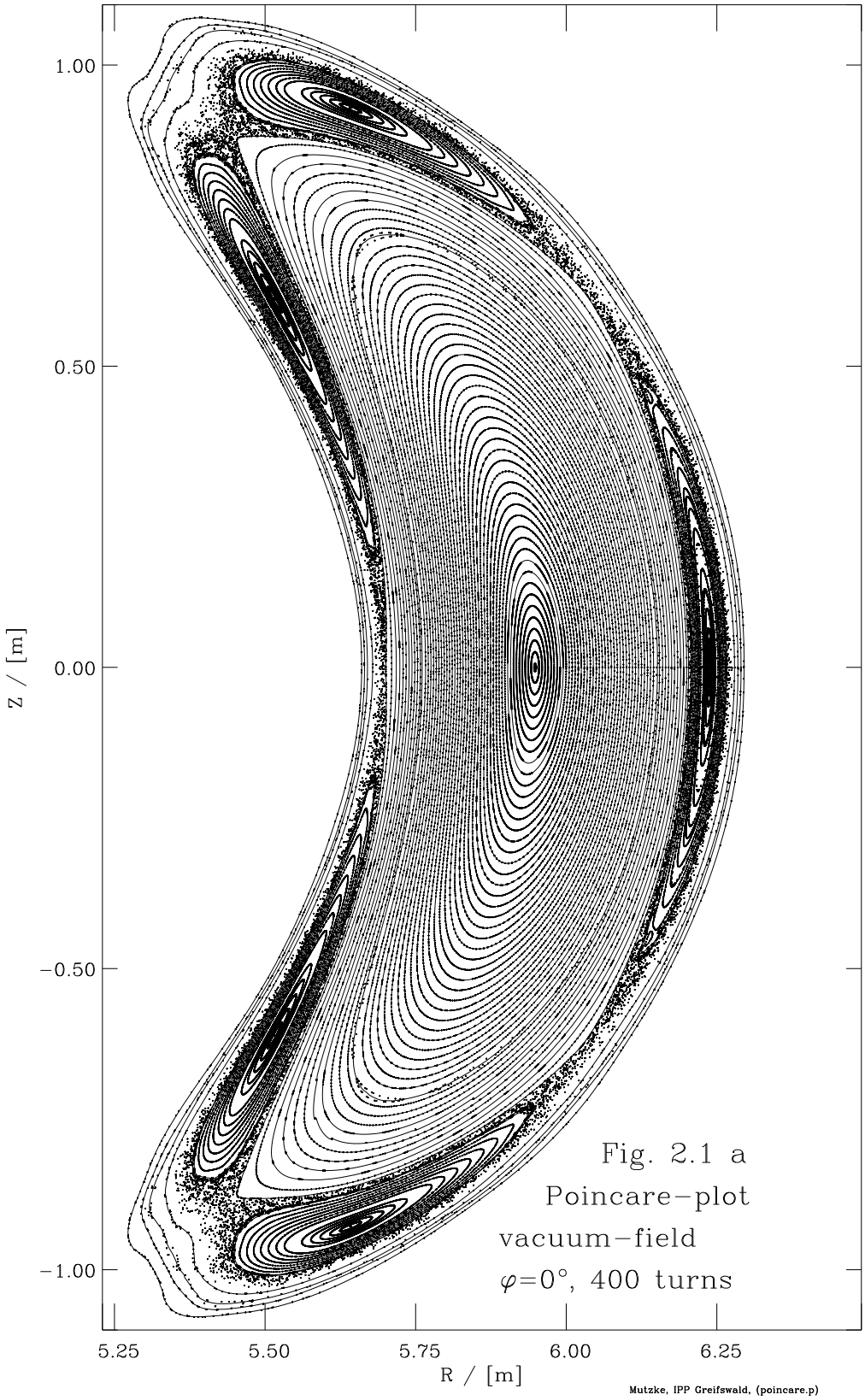
1.00
0.50
0.00
−0.50
−1.00
Z / [m]
5.25
5.50
5.75
6.00
6.25
R / [m]
Fig. 2.1 a
Poincare−plot
vacuum−field
φ=0°, 400 turns
Mutzke, IPP Greifswald, (poincare.p)

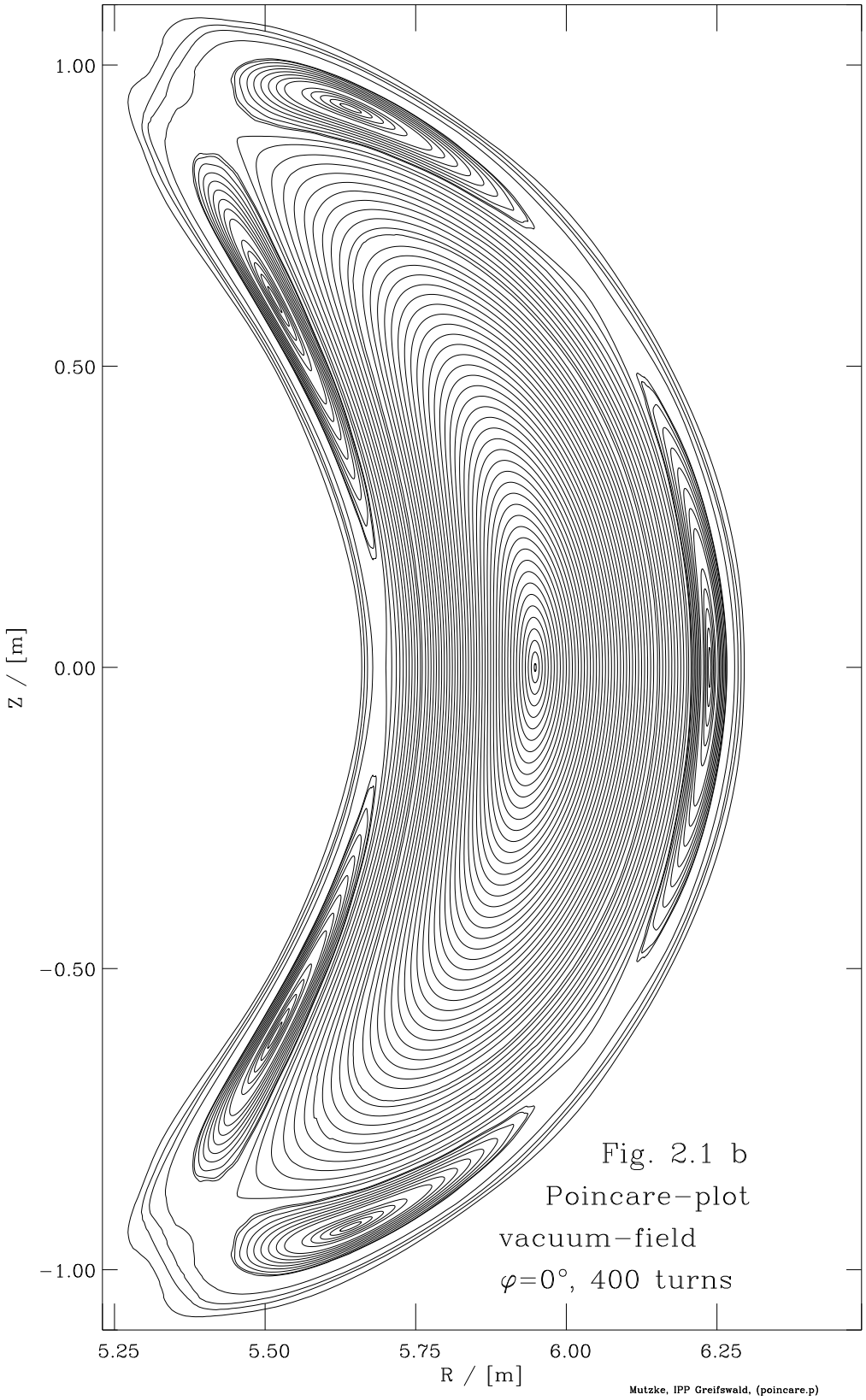
1.00
0.50
0.00
−0.50
−1.00
Z / [m]
5.25
5.50
5.75
6.00
6.25
R / [m]
Fig. 2.1 b
Poincare−plot
vacuum−field
φ=0°, 400 turns
Mutzke, IPP Greifswald, (poincare.p)

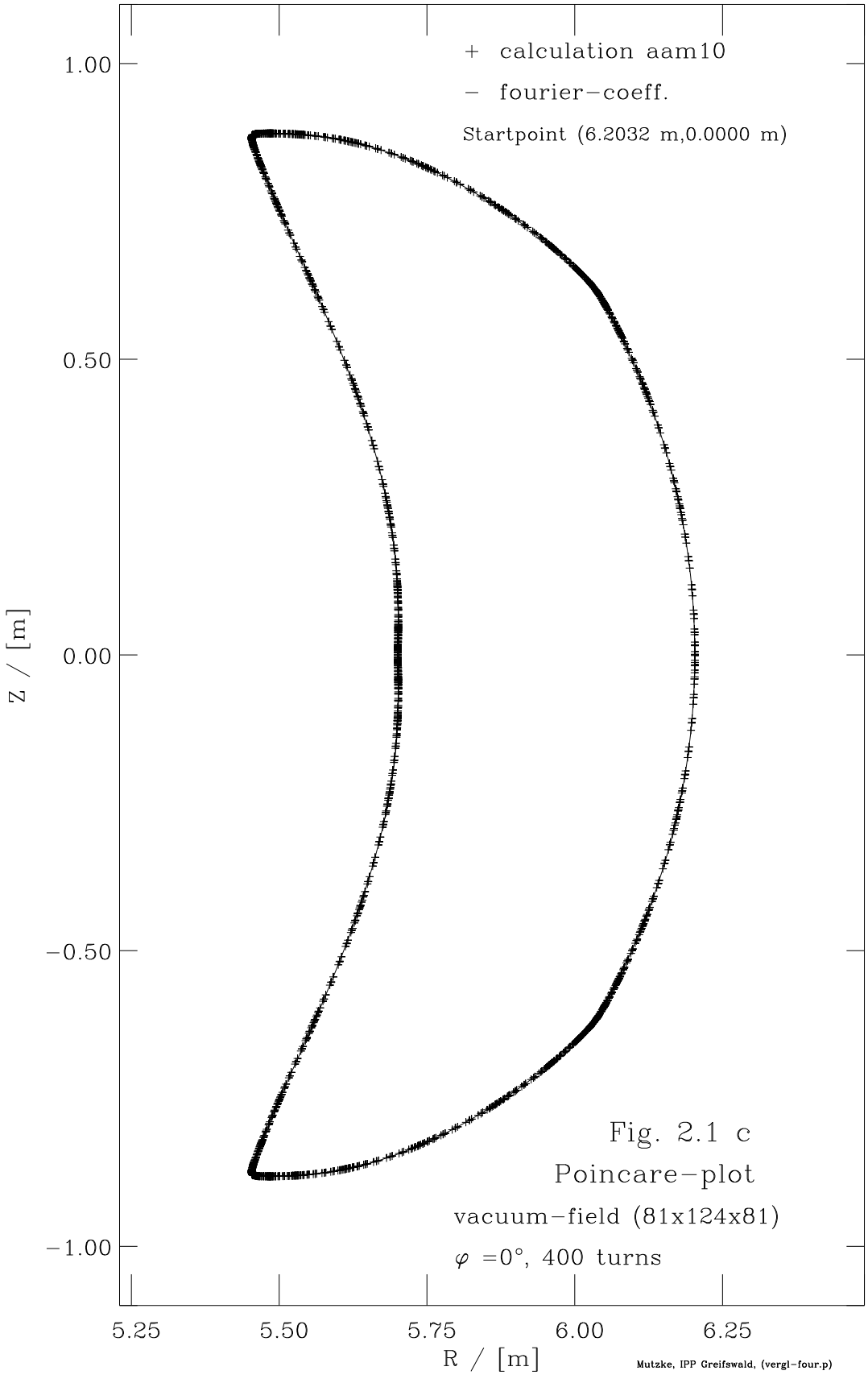
+ calculation aam10
− fourier−coeff.
Startpoint (6.2032 m,0.0000 m)
1.00
0.50
0.00
−0.50
−1.00
Z / [m]
5.25
5.50
5.75
6.00
6.25
R / [m]
Fig. 2.1 c
Poincare−plot
vacuum−field (81x124x81)
φ =0°, 400 turns
Mutzke, IPP Greifswald, (vergl−four.p)

2.3 Calculation of ϑ_{real}, ι and χ

As a first step to get the values ϑ_{real} and ι, we performed the calculation for the fieldline of magnetic axis $x_0(i)$, $y_0(i)$, $z_0(i)$. ϑ_{real} is the angle in real coordinates relative to the magnetic axis. The other fieldlines have got the coordinates $x(j)$, $y(j)$, $z(j)$.

The angle of the start point ϑ_0 at $\varphi = 0°$ is:

$$\vartheta_0 = arctan\left(\frac{z_{start} - z_{0start}}{x_{start} - x_{0start}}\right) \tag{2.8}$$

The poloidal angle ϑ_{real} is :

$$\vartheta_{real}(j) = arctan\left(\frac{z(j) - z_0}{r(j) - r_0}\right) - \vartheta_0 + \Theta_p \cdot 360° \quad \Theta_p \ldots \text{number of poloidal turns} \tag{2.9}$$

with:

$$r(j) = \sqrt{x(j)^2 + y(j)^2} \tag{2.10}$$

$$r_0 = \sqrt{x_0^2 + y_0^2} \tag{2.11}$$

$$\varphi(j) = arctan\left(\frac{y(j)}{x(j)}\right) \tag{2.12}$$

$$\varphi_0 = arctan\left(\frac{y_0}{x_0}\right) \tag{2.13}$$

If the maximum numbers of turns is 400 then the rotational transform ι is:

$$\iota_t(\Phi_t) = \frac{\vartheta_{real}(\Phi_t)}{\Phi_t \cdot 360°} \quad \Phi_t \ldots \text{number of toroidal turns} \tag{2.14}$$

$$\iota = \frac{1}{50} \cdot \sum_{\Phi_t=350}^{400} \iota_t(\Phi_t) \tag{2.15}$$

r_0 and z_0 are interpolated by x_0, y_0, z_0, so that is $\varphi(j) = \varphi_0$.
Figure 2.2 a shows the average angle ϑ_{real} dependent on the distance to the magnetic axis. Radii under 260 mm represent the core region and greater than 330 mm the scrape-off layer.
Within each calculated fieldline turn (there are 400 turns), the poloidal rotational transform has a variation on each turn, see Figure 2.3.

The calculation of an exact rotational transform ι is difficult. The average after 400 turns is not constant, see Figure 2.3 b. Therefore the average of the last 50 averages was used to compute ι, Equation 2.15.
The average values of χ after 400 turns are shown in Figure 2.2 b.
The integral, see 1.3, is:

$$\chi_{real} = \int \vec{B} \cdot d\vec{\ell} \quad \vec{\ell} \ \ldots \text{ along a fieldline} \tag{2.16}$$

the numerical realisation is:

$$\chi_{real} = \sum \left(B_x \cdot \Delta x + B_y \cdot \Delta y + B_z \cdot \Delta z \right) \tag{2.17}$$

$$\vec{\ell} = \Delta x \cdot \hat{e}_x + \Delta y \cdot \hat{e}_y + \Delta z \cdot \hat{e}_z \qquad \hat{e}_x, \hat{e}_y, \hat{e}_z \ \ldots \text{ unit vectors} \tag{2.18}$$

$$\chi_t(\Phi_t) = \frac{\chi_{real}}{\Phi_t} \qquad \Phi_t \ldots \text{number of toroidal turns} \tag{2.19}$$

$$\chi_m = \frac{1}{50} \cdot \sum_{\Phi_t=350}^{400} \chi_t(\Phi_t) \tag{2.20}$$

The average of χ after 400 turns is not constant. Therefore the average of the last 50 averages was used to compute χ_m, Equation 2.20.

Because $\Delta h > 0$ the results of ι and χ are calculated for a left-handed magnetic coordinate system.

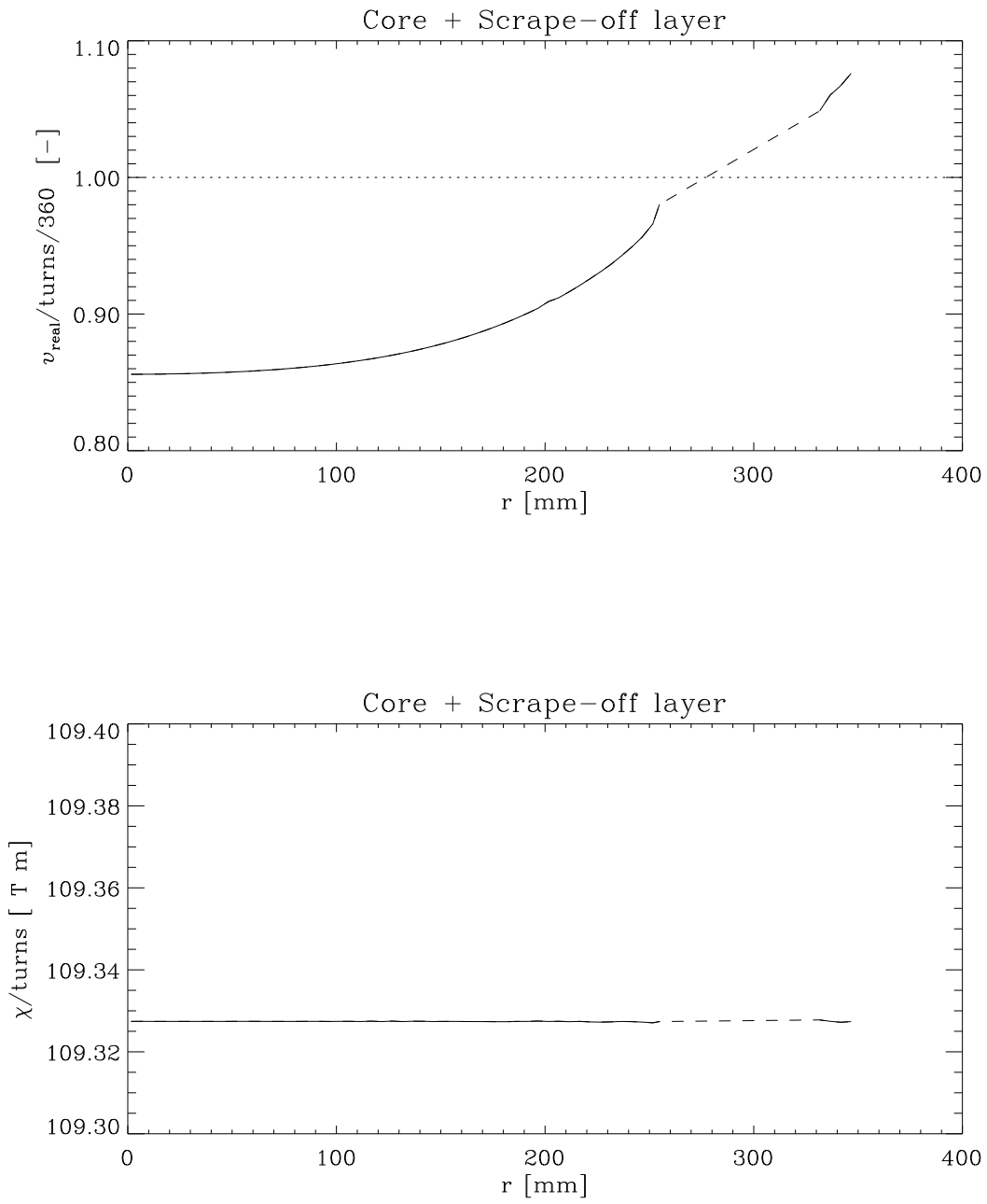

Fig. 2.2 υ_{real}/turns and χ_{real}/turns vacuum magnetfield
step: h=0.0005, 400 turns (81x124x81, ca. 5.0cm)

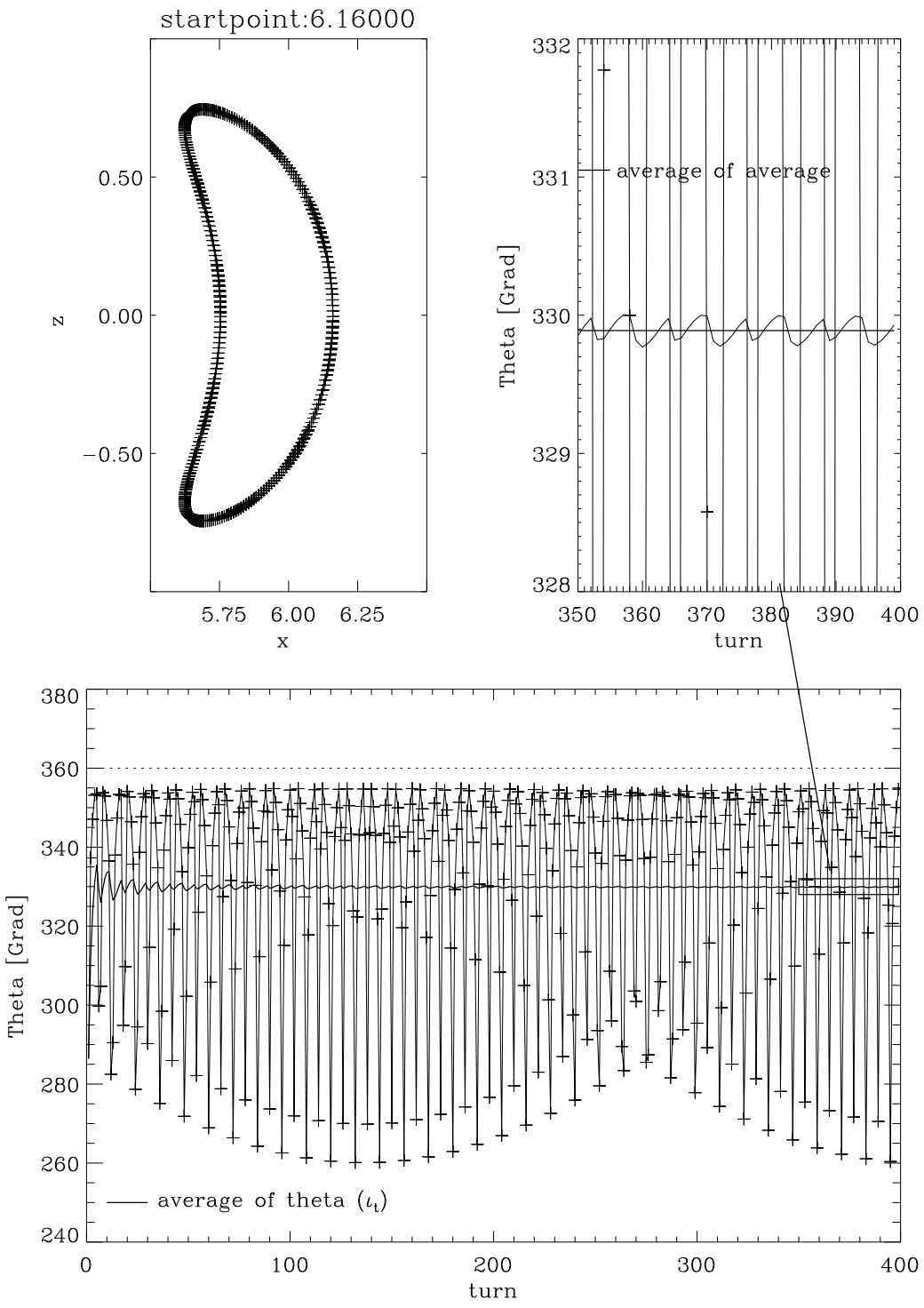

Fig. 2.3 Variation of theta per turn, $\varphi = 0°$

Step: h=0.0005, 400 turns (81x124x81, ca. 5.0 cm)

2.4 Calculation of the flux functions F_T, F'_T, F_P, F'_P and magnetic coordinate s

F_T and F_{Tr}, see 1.6, are determined by:

$$F_T = \oint \vec{B} \cdot d\vec{A} \quad \vec{A} \ \ldots \text{ normal area to the Poincaré section} \tag{2.21}$$

$$F_{Tr} = \frac{dF_T}{dr} \tag{2.22}$$

The finite formulations are:

$$F_T = \sum B_y \cdot \Delta x \cdot \Delta z \tag{2.23}$$

$$F_{Tr}\Big|_i = \frac{F_T(i+1) - F_T(i-1)}{x(i+1) - x(i-1)} \tag{2.24}$$

where i is the index of start point r_i or index of toroidal flux F_{Ti}.

Figure 2.5 shows the components of magnetic field B_y with Poincaré sections of the core and the islands.
The values of $F_T(r)$ and $F_{Tr}(r)$ may be found from Figure 2.6 a. The values $r > 0$ (r^+) are the startpoint of the fieldline. The values $r < 0$ (r^-) are the second intersection of the Poincaré section with the x-axis. These points are to the left of the magnetic axis, therefore is r negative.
There are :

$$r_i^- \neq -r_i^+ \tag{2.25}$$

$$F_{Ti}^- = F_{Ti}^+ \tag{2.26}$$

The derivatives F_{Tr} were calculated with the help of the centered finite difference quotient (+ sign) and the derivative of a polynomial (line).
The form of polynomial is :

$$F_T = a_2 \cdot x^2 + a_2 \cdot x^3 + a_2 \cdot x^4 + a_5 \cdot x^5 + a_6 \cdot x^6 + a_7 \cdot x^7 \tag{2.27}$$

The coefficients a_i were calculated with the least-squares approach.
The derivatives F_{tr} is :

$$F_{Tr} = 2 \cdot a_2 \cdot x + 3 \cdot a_2 \cdot x^2 + 4 \cdot a_2 \cdot x^3 + 5 \cdot a_2 \cdot x^4 + 6 \cdot a_6 \cdot x^5 + 7 \cdot a_7 \cdot x^6 \tag{2.28}$$

The best way to estimate the derivatives is the polynomial method (line).

The magnetic coordinate s and its derivative, see 1.6, are calculated :

$$s = \frac{F_T}{F_T(\Psi_{sep})} \tag{2.29}$$

$$F'_T = \frac{dF_T(s)}{ds} \tag{2.30}$$

$F_T(\Psi_{sep})$ is the end value of the core curve of F_T.

The comparison of values $F_T(s)$ and F'_T calculated with programs `VMEC` and `aam10` may be found in Figure 2.6 c.

$$F_P = F_T \cdot \iota \tag{2.31}$$
$$F'_P = F'_T \cdot \iota \tag{2.32}$$

The values of $F_P(s)$ and F'_P may be found in Figure 2.6 d.
The values of rotational transform ι and χ (see Section 2.3) and their spline approximation may be found in Figure 2.6 f.
The Figure 2.6 g shows the dependence of the value r on s. The line is the spline approximation.
The way to get F_T as a function of s consists of two steps:

- The coordinates r, $F_T(r)$ and $s(r)$ are given.
    1. With the help of the polynomial interpolation we get $F_T(r)$, see Figure 2.6 a.
    2. With the help of the spline interpolation we get $s(r)$, see Figure 2.6 g.
- Then we find $F_T(s)$.

Figure 2.6 g shows the comparison of value F_{Tr} dependent on s calculated with the `VMEC` program (line) and `aam10` (points). Near the X-Point of magnetic field ($F^-_{Tr}(s = 1)$) there are great differences.

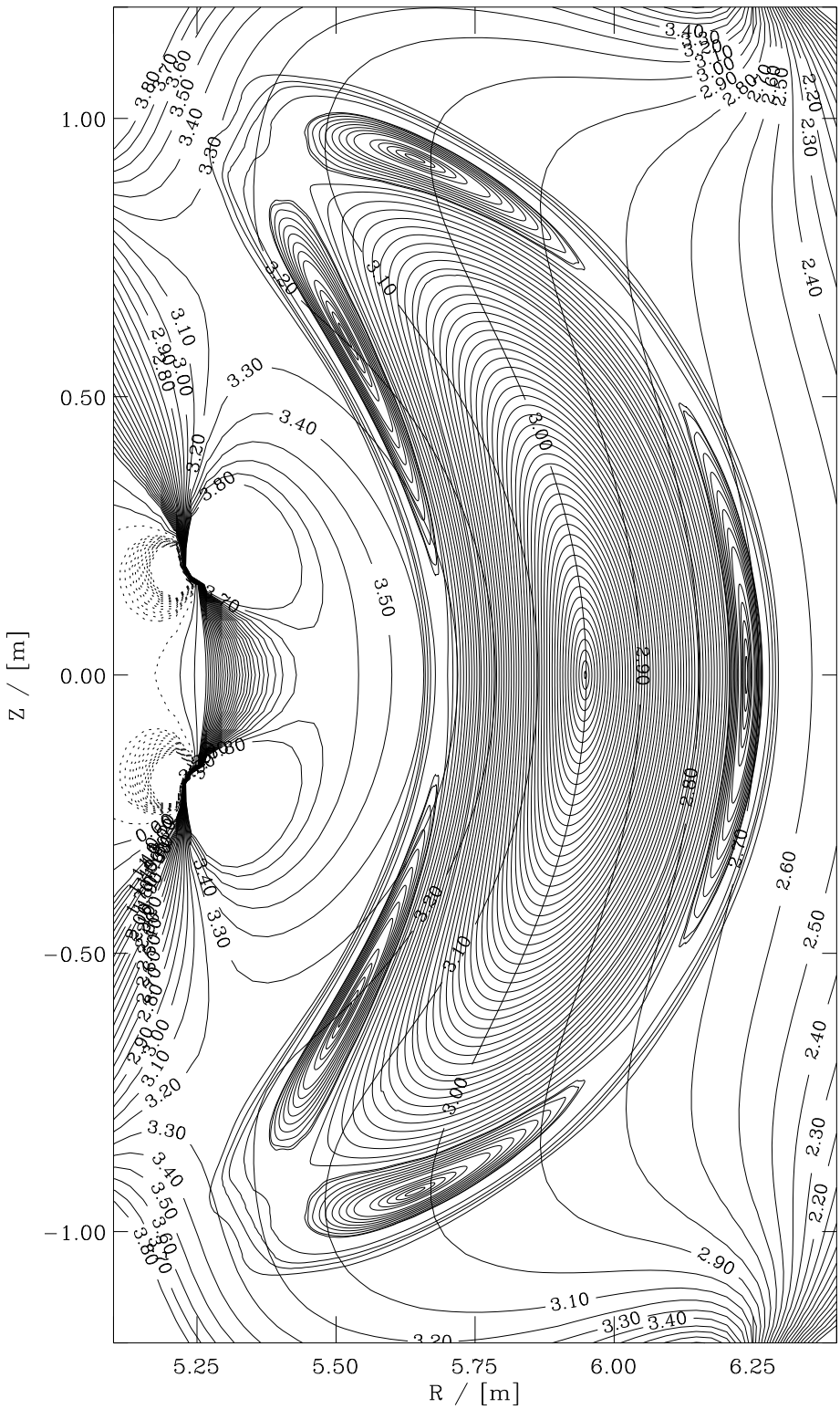

Fig. 2.5 Poincare−plots with By of vacuum magnetic field, φ =0°
Step: h=0.0005, 400 turns (resolution: 81x124x81, ca. 5.0 cm)

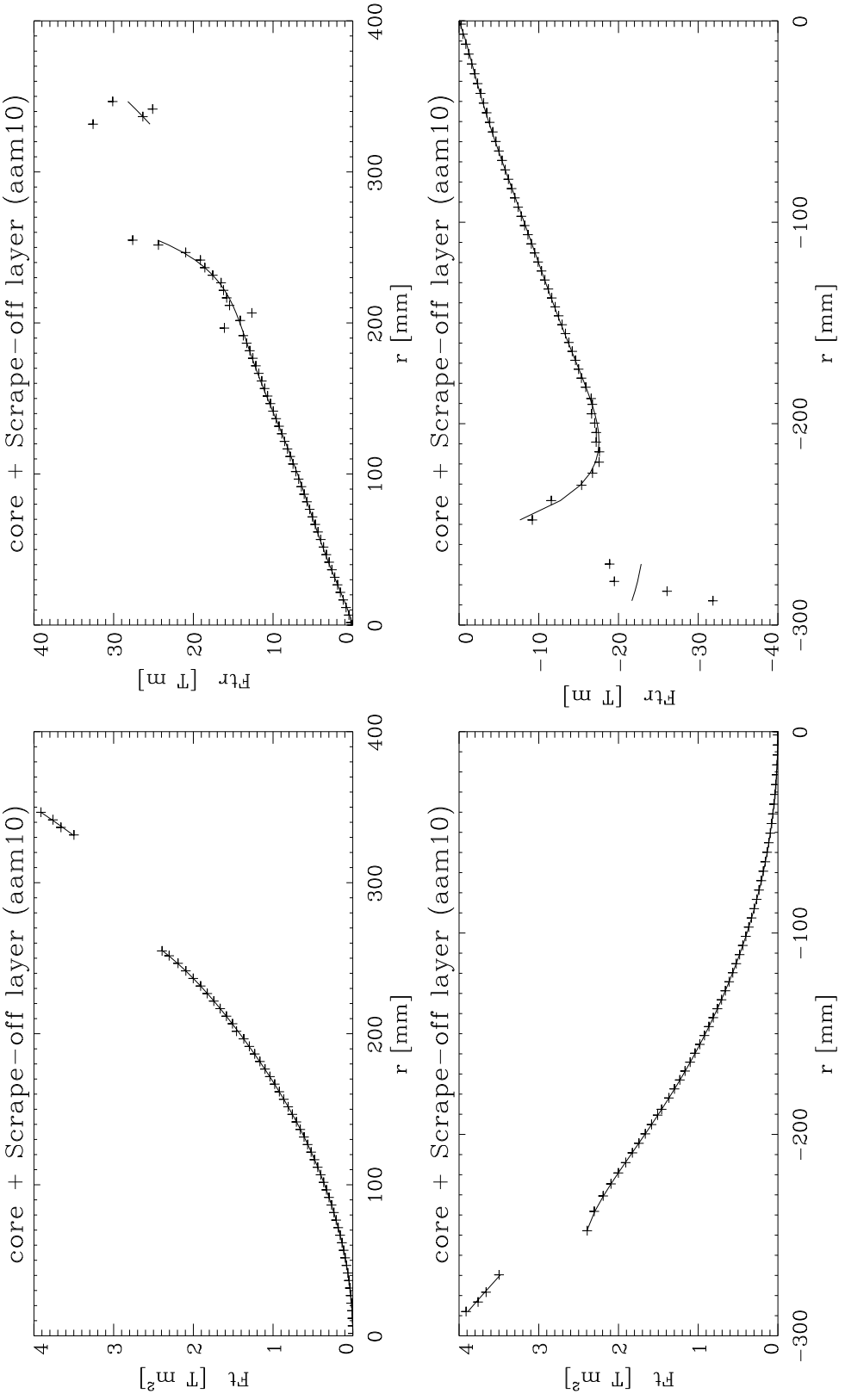

Fig. 2.6 a $\quad Ft_r = d\left(\int By\ dx\ dz\right)/dr \qquad Ft = \int By\ dx\ dz$

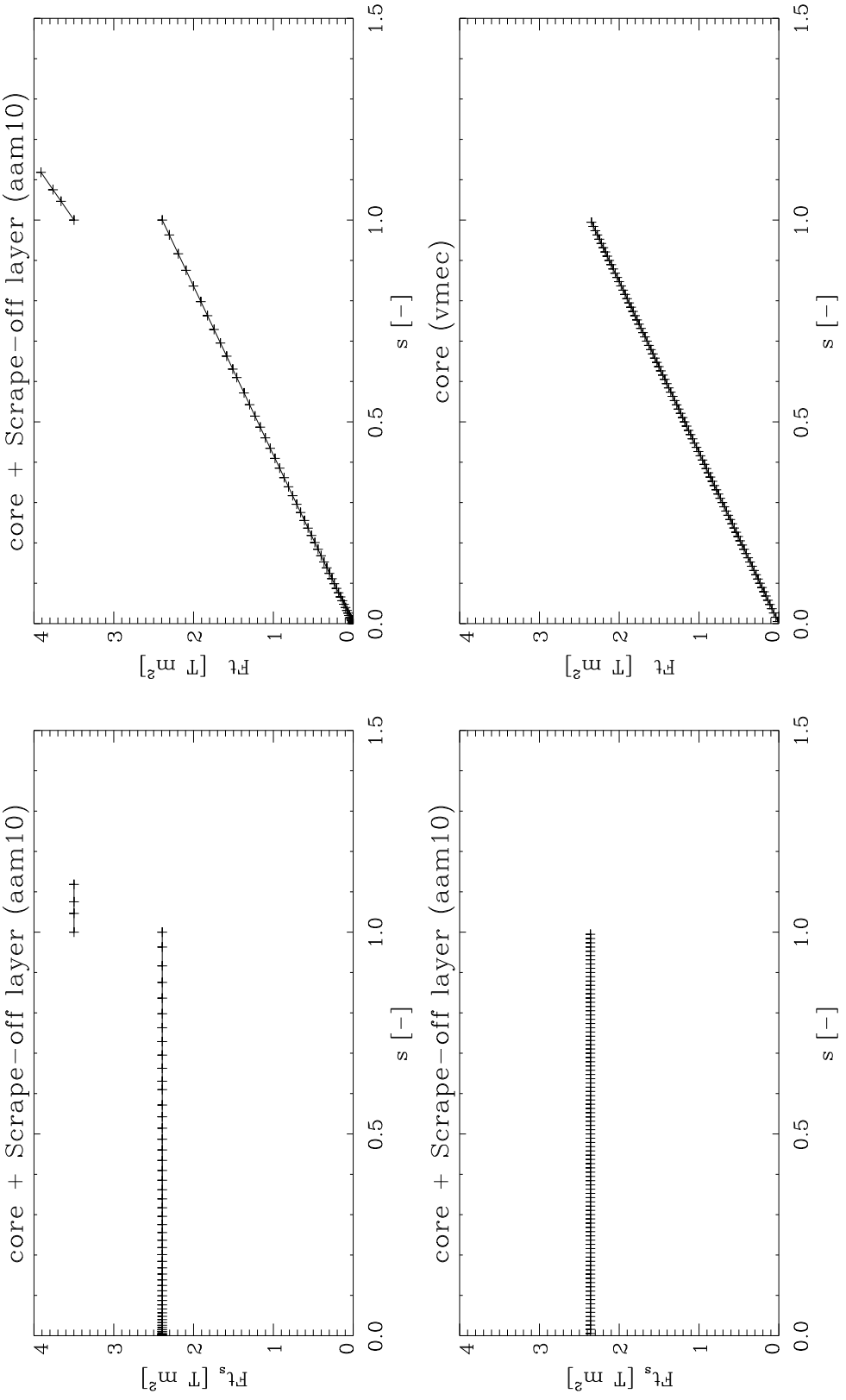

Fig. 2.6 c Compare of $Ft_s(s)$ and $Ft(s)$

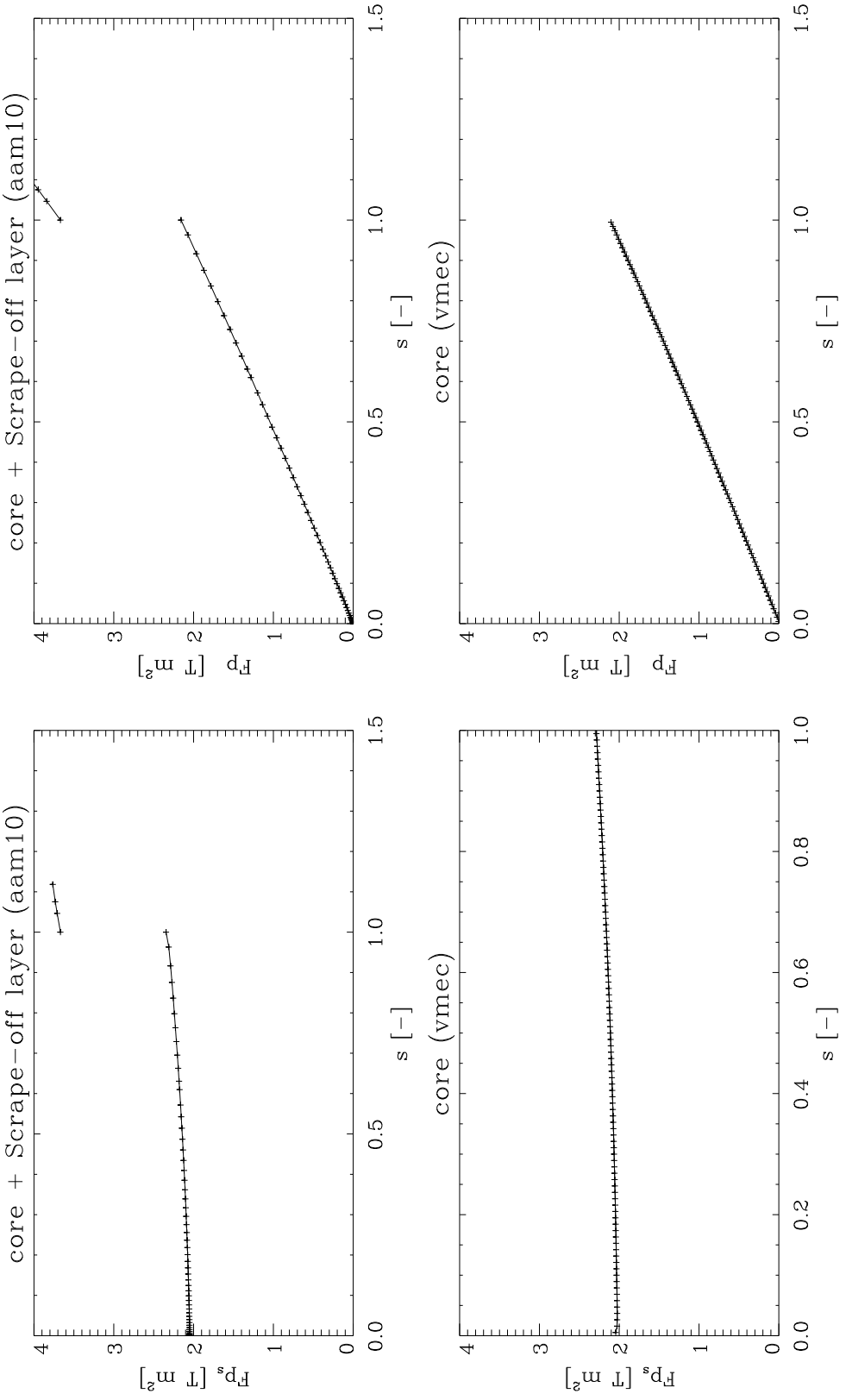

Fig. 2.6 d Compare $Fp_s(s)$ and $Fp(s)$

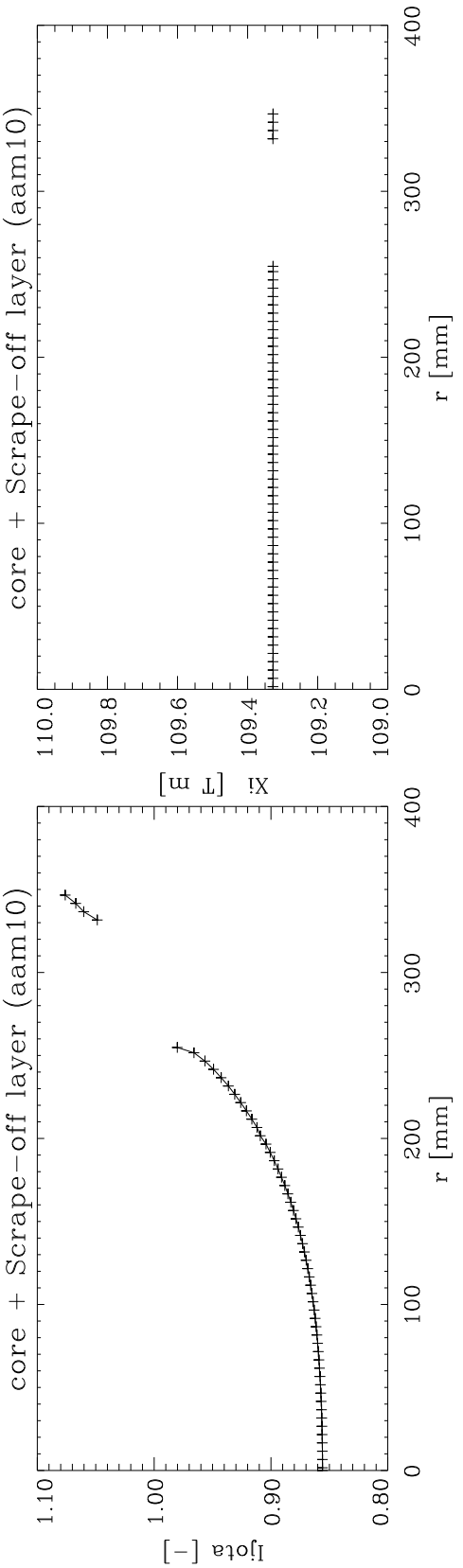

Fig. 2.6 f Ijota(r,φ=0,z=0) Xi(r,φ=0,z=0)

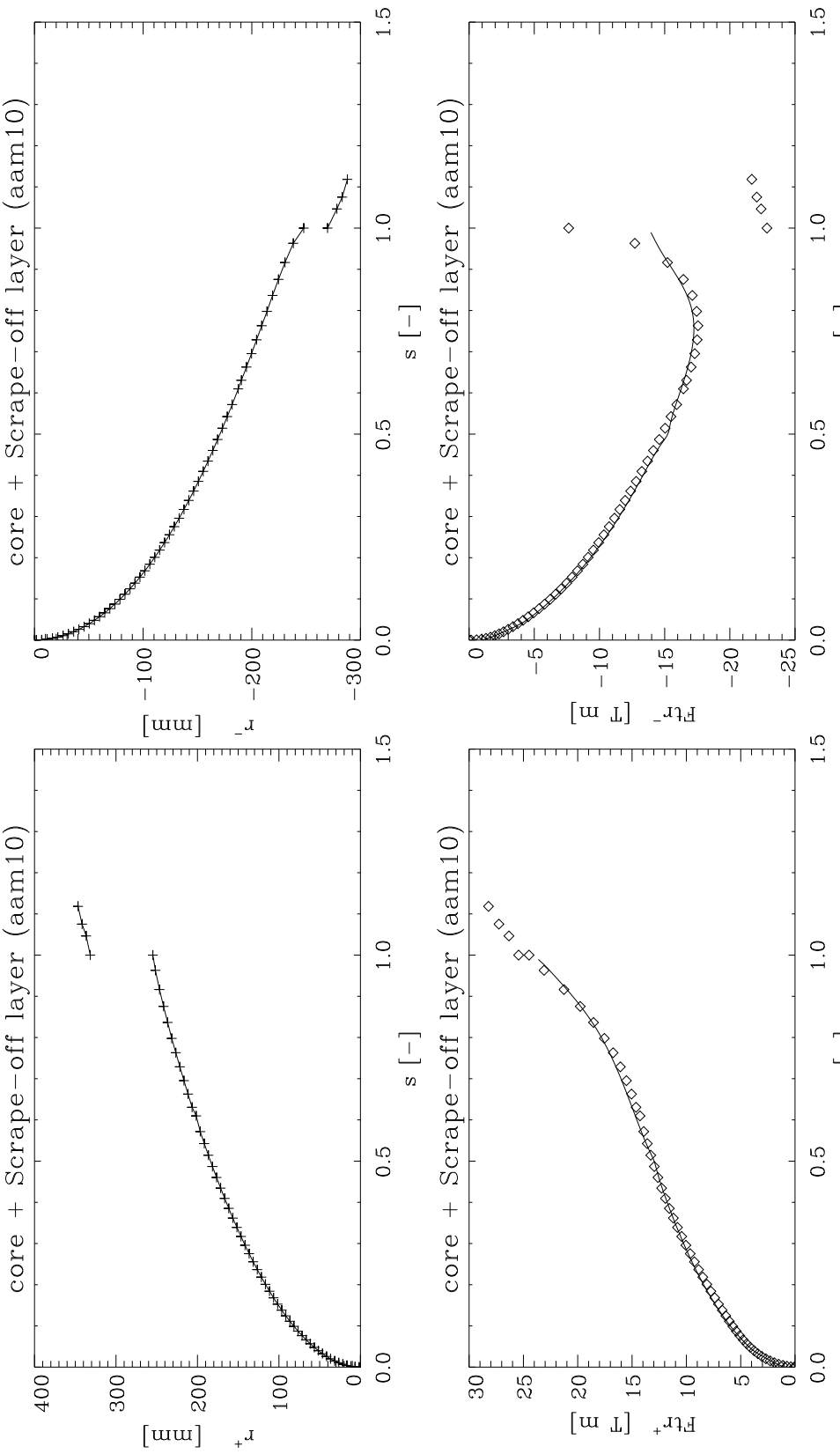

Fig. 2.6 g $r|_{\varphi=0,z=0} = f(s)|_{\upsilon=0,\phi=0}$, compare Ft_r=f(s) [vmec(−) aam10(◇)]

2.5 Compute the toroidal current J

The next step is the calculation of the values of toroidal current J, see Section 1.7:

$$J \cdot \mu_0 = \oint \vec{B} \cdot d\vec{\ell} \quad \vec{\ell} \ \ldots \text{ along the Poincaré sections} \tag{2.33}$$

$$J = \frac{1}{\mu_0} \oint B_{x,z} \, dx \, dz \tag{2.34}$$

The numerical formulation is:

$$J = \frac{1}{\mu_0} \sum (B_x \cdot \Delta x + B_z \cdot \Delta z) \tag{2.35}$$

The components of magnetic field B_x and B_z with Poincaré sections of the core are shown in Figure 2.7.
The comparison of values J calculated with program `VMEC` and `aam10` may be found in Figure 2.8. The values of J are esentially zero. The `VMEC` output includes the factor μ_0.

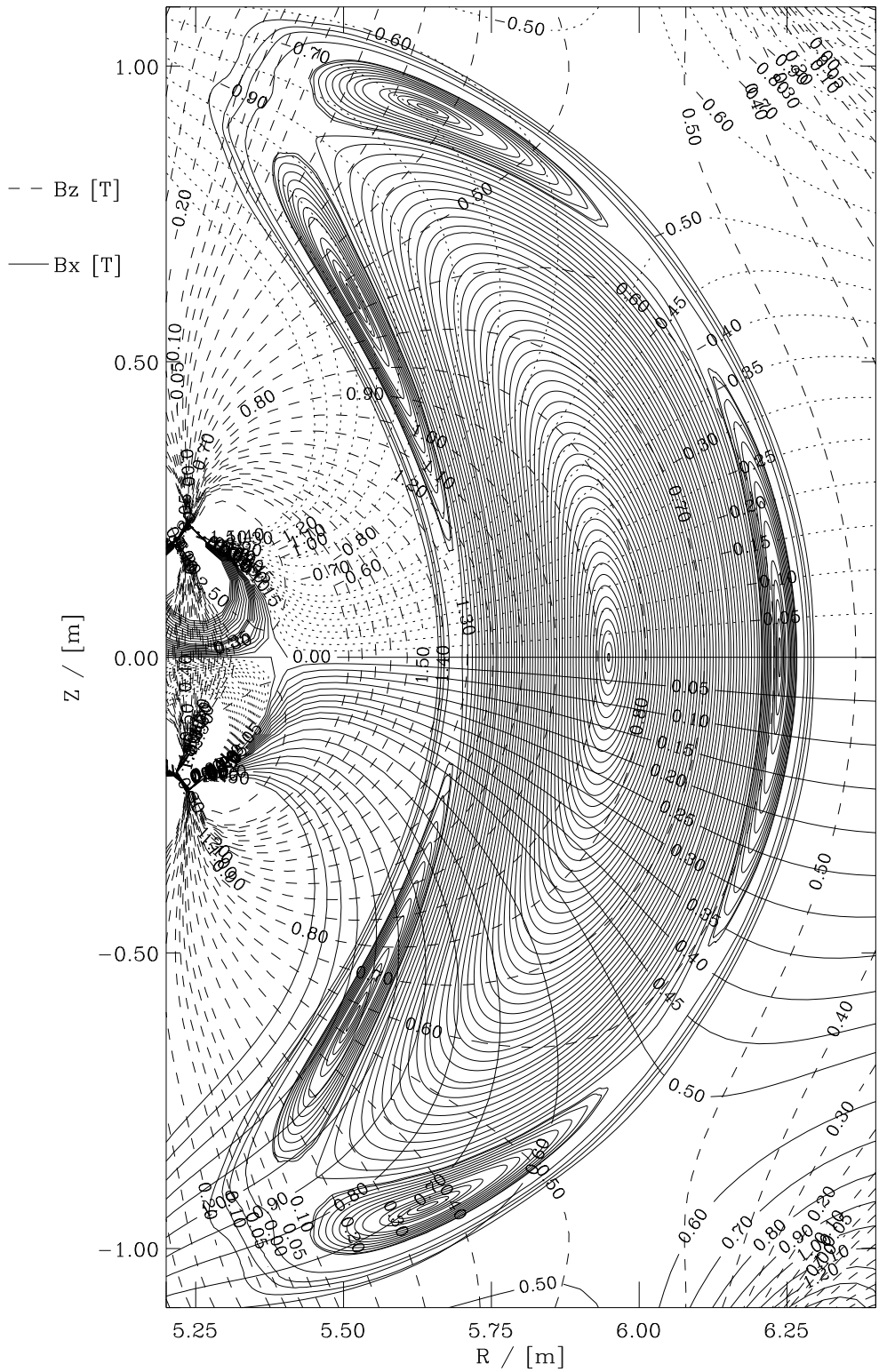

Fig. 2.7 Poincare−plots with Bx and Bz of magnetic field, φ =0° step: h=0.0005, 400 turns (81x124x81, ca. 5.0 cm)

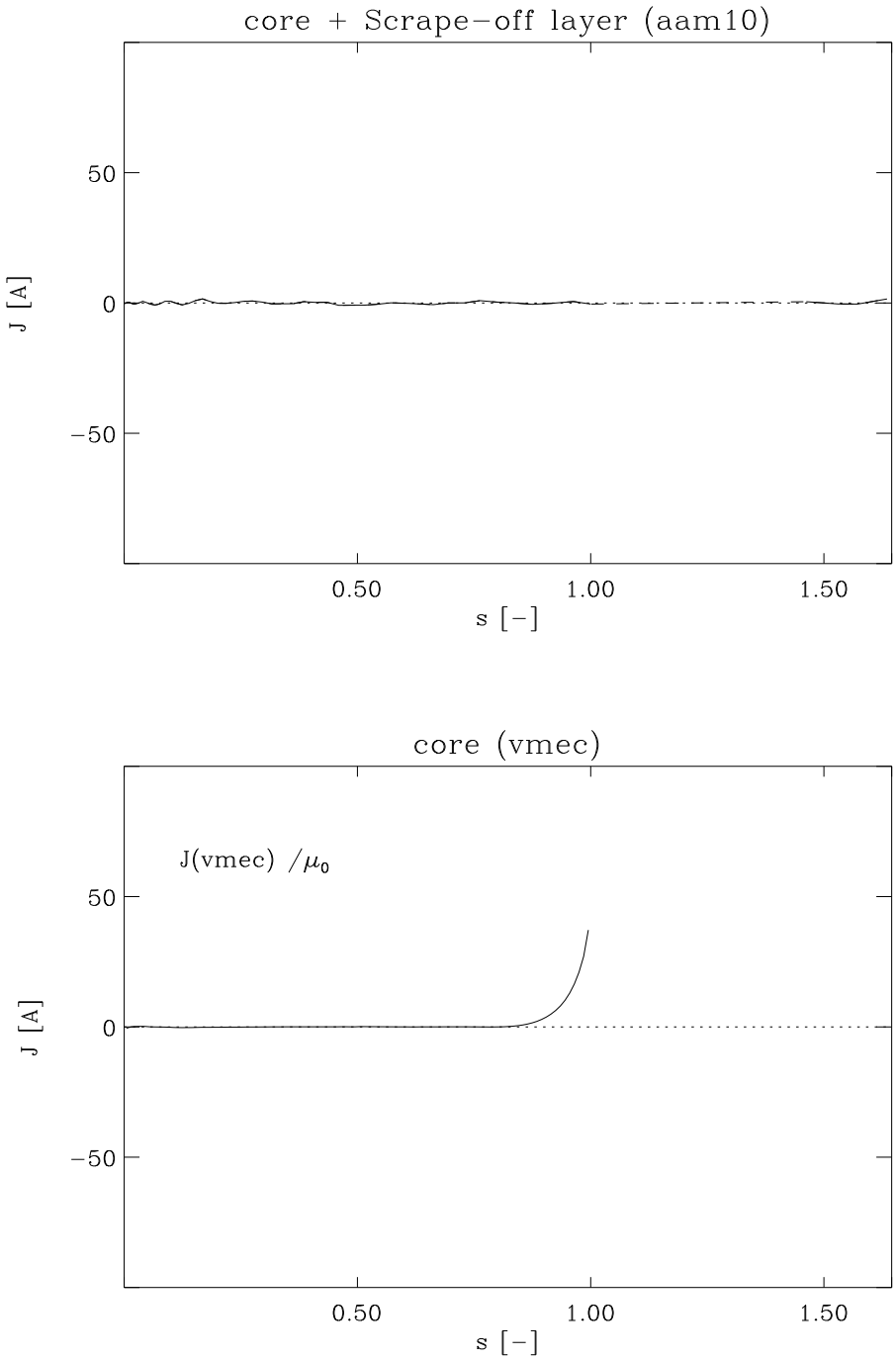

Fig. 2.8 Compare current J

2.6 Compute the current I

I is a sum of 2 integrals, see Section 1.8. The total path of these integrals is closed.

$$I \cdot \mu_0 = \int \vec{B} \cdot d\vec{\ell_1} + \int \vec{B} \cdot d\vec{\ell_2} \tag{2.36}$$

ℓ_1 along the fieldline (toroidally) from the start-point to the end-point of one turn

ℓ_2 along the Poincaré sections (poloidally backwards) from end-point to the start-point

The first integral is χ (see Section 2.3) for one turn. The second integral is a part of J (see Section 2.5).

The numerical formulation is:

$$I = \frac{1}{\mu_0} \Big[\sum \left(B_x \cdot \Delta x + B_y \cdot \Delta y + B_z \cdot \Delta z \right) \mid \ell_1 + \sum \left(B_x \cdot \Delta x + B_z \cdot \Delta z \right) \mid \ell_2 \Big]$$

Figure 2.9 shows the calculated current I. In the vacuum magnetic field, I is the sum of the currents in the coils. The `VMEC` output includes the factor μ_0 and is reduced to one period.

Because $\Delta h > 0$ the results of I is calculated for a left-handed magnetic coordinate system.

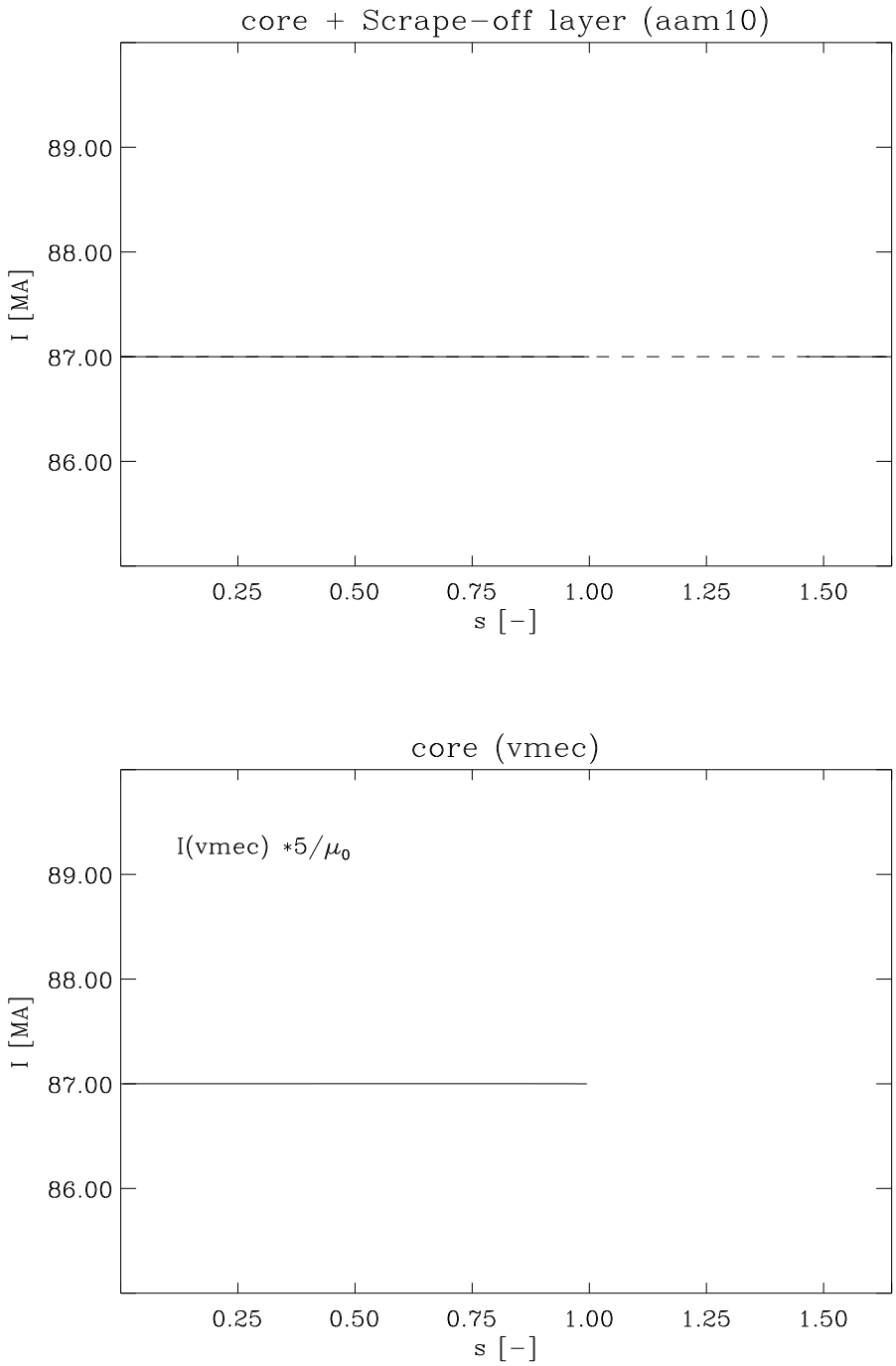

Fig. 2.9 Compare current I

2.7 Calculation of coefficient $\sqrt{g}$

The next step is the calculation of the coefficient $\sqrt{g}$, see Section 1.9. The magnetic coordinates has a ranging over $[0 \ldots 1; 0 \ldots 1; 0 \ldots 1]$ and because $\Delta h > 0$ the formular is for a left-handed magnetic coordinate system.

The start-points $r_p(R,\ \varphi\ =\ 0,\ z\ =\ 0)$ of Poincaré sections fix the values of $I(r_p)$, $J(r_p)$, $\iota(r_p)$ and $F_T(\Psi_{sep})$. With the help of the transformation from r to s, see Figure 2.6 g, are also given $r_p(s,\ \vartheta\ =\ 0,\ \Phi\ =\ 0)$, $I(s)$, $J(s)$ and $\iota(s)$.
In this case, the current I is constant and J is zero. Therefore $\sqrt{g}$ is only a function of magnetic field B.

$$\sqrt{g}(R,\varphi,z) = -\frac{[I(r_p)\cdot\mu_0 + \iota(r_p)\cdot J(r_p)\cdot\mu_0]\cdot F_T(\Psi_{sep})}{B^2(R,\varphi,z)}. \tag{2.37}$$

or

$$\sqrt{g}(s,\varphi,z) = -\frac{[I(s)\cdot\mu_0 + \iota(s)\cdot J(s)\cdot\mu_0]\cdot F_T(\Psi_{sep})}{B^2(s,\varphi,z)}. \tag{2.38}$$

or

$$\sqrt{g}(s,\vartheta,\Phi) = -\frac{[I(s)\cdot\mu_0 + \iota(s)\cdot J(s)\cdot\mu_0]\cdot F_T(\Psi_{sep})}{B^2(s,\vartheta,\Phi)}. \tag{2.39}$$

The Figures 2.10 show the comparison of the coefficient $\sqrt{g}$ dependent on s for the start point at $\varphi\ =\ 0$, $z\ =\ 0$ or $\vartheta\ =\ 0$, $\Phi\ =\ 0$.
The `VMEC` output is reduced to one period.

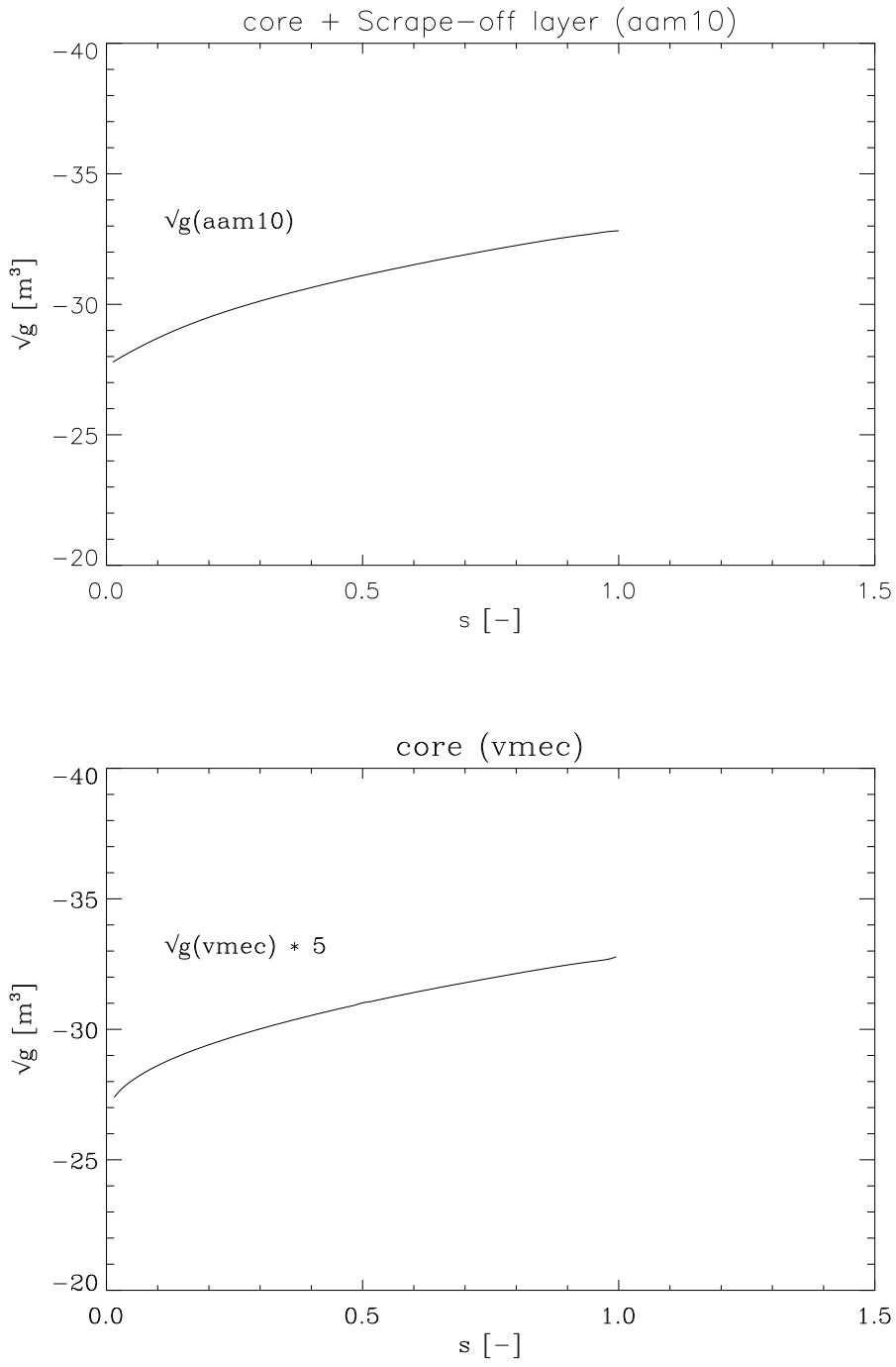

Fig 1.10 Compare √g depend of s

2.8 Calculation of magnetic coordinates

The start point in magnetic coordinates $r_p(s,\, \vartheta \,=\, 0,\, \Phi \,=\, 0)$ is given. The equivalent real coordinates are $r_p(R,\, \varphi \,=\, 0,\, z \,=\, 0)$.
The algorithm, see Section 1.10, to calculate the magnetic coordinates ϑ and Φ are :

$$\vartheta(\ell) \;=\; \frac{\iota(s)\cdot\chi(\ell)}{\mu_0\cdot[I(s)+\iota(s)\cdot J(s)]} \;(\text{mod } 1) \quad \ell \;\ldots \text{ along a fieldline} \tag{2.40}$$

$$\Phi(\ell) \;=\; \frac{\chi(\ell)}{\mu_0\cdot[I(s)+\iota(s)\cdot J(s)]} \;(\text{mod } 1) \quad \ell \;\ldots \text{ along a fieldline} \tag{2.41}$$

or

$$\vartheta(\ell) \;=\; \frac{\iota(s)\cdot\chi(\ell)}{\chi_m(s)} \;(\text{mod } 1) \quad \ell \;\ldots \text{ along a fieldline} \tag{2.42}$$

$$\Phi(\ell) \;=\; \frac{\chi(\ell)}{\chi_m(s)} \;(\text{mod } 1) \quad \ell \;\ldots \text{ along a fieldline} \tag{2.43}$$

ℓ is a function of R, φ and z. Now it is possible to estimate the real coordinates R, φ and z for given magnetic coordinates s, ϑ, Φ. The range of s, ϑ, Φ is from 0 to 1.
The Figures 2.11 show the comparison of the real coordinates on the (x, z) plane at $s \,=\, 1$, $\Phi \,=\, 0$ and at $s \,=\, 0.4$, $\Phi \,=\, 0$.
The Figures 2.12 show the comparison of the real coordinates on the (y, z) plane at $s \,=\, 1$, $\Phi \,=\, 0$ and at $s \,=\, 0.4$, $\Phi \,=\, 0$.

To reduce the length of the fieldline and the numeric errors it was started at two points into two directions. The start points are the intersections of Poincaré curve with the x-axis and the directions are towards positive φ and negative φ.
The Figures 2.13 a and 2.14 a show the points of a Poincaré section in the (R, z) plane, the z values dependent on ϑ and the y values dependent on ϑ. The quality of the Poincaré sections is good. The method of Runge-Kutta yields good results to calculate x, y and z values of the fieldlines.
In the neighbourhood of the separatrix of near small island chains, one must be more careful. The quality of z and y values dependent on ϑ are insufficient. When crossing an island chain, one must adapt the fitted ι profile to the local value. Otherwise, significant differences appear between subsequent toroidal passes of the field-line tracing. This case occurs near $s = 0.6$, where we find a 10/11 island chain, see Figure 2.20. Similarly, the separatrix $s = 1.0$ is at the edge of the ergodic range, where many small island chains are also present. The sensitivity on the exact ι value is illustrated by Figures 2.13 b and 2.14 b. One can clear see that a minute change in ι (and of the start-point) can dramatically improve results.
ι and the second start point according to the method in Section 2.3 (old) and after fine-tuning (new):

s	ι (fit)	ι (adjusted)	x-start (fit)	x-start (adjusted)
1.0	0.9805	0.9789	5.7006 m	5.7011 m
0.6	0.9087	0.9079	5.7622 m	5.7622 m

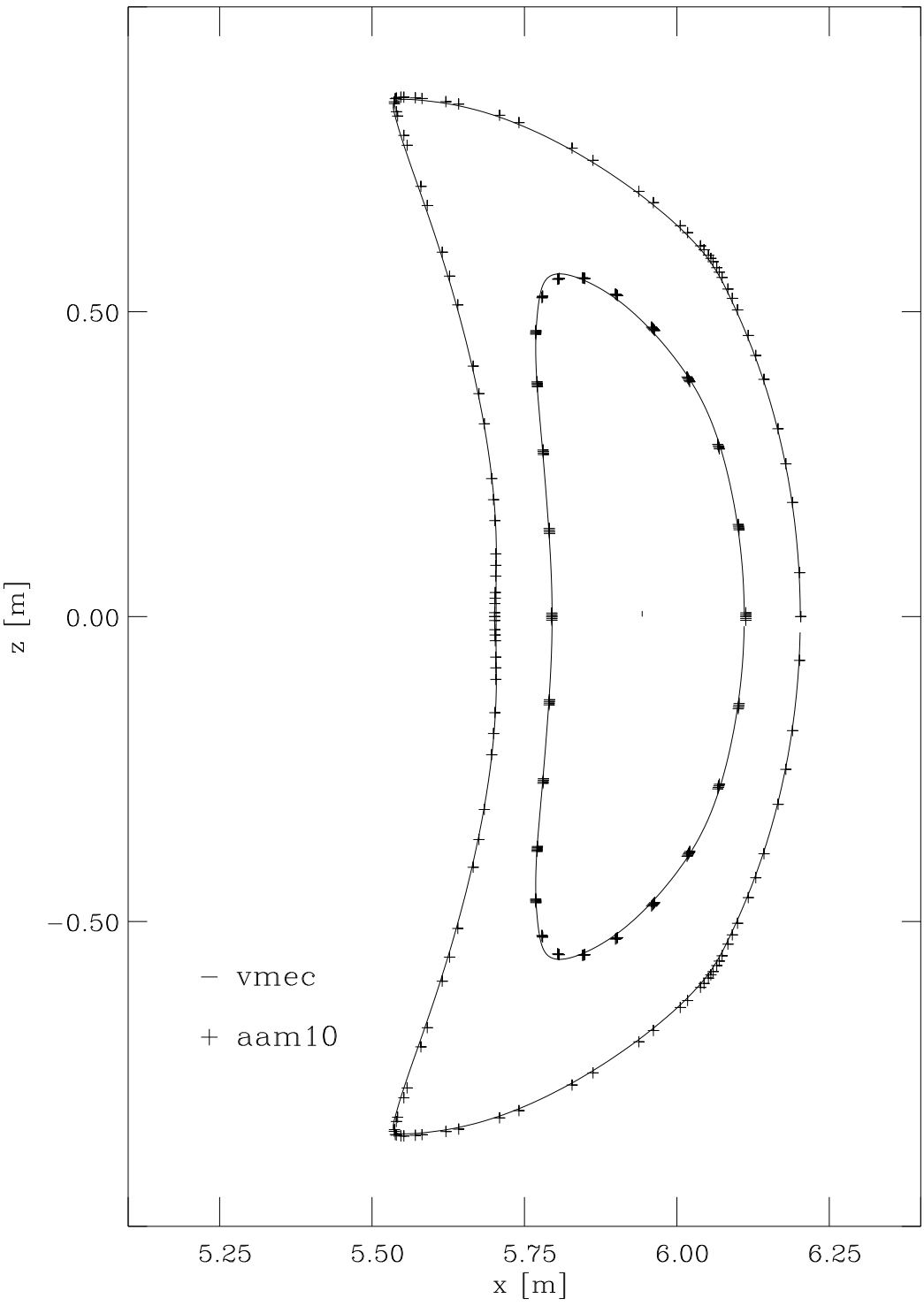

Fig 2.11 Poincare−plot s=1.00 and s=0.4, Φ=0

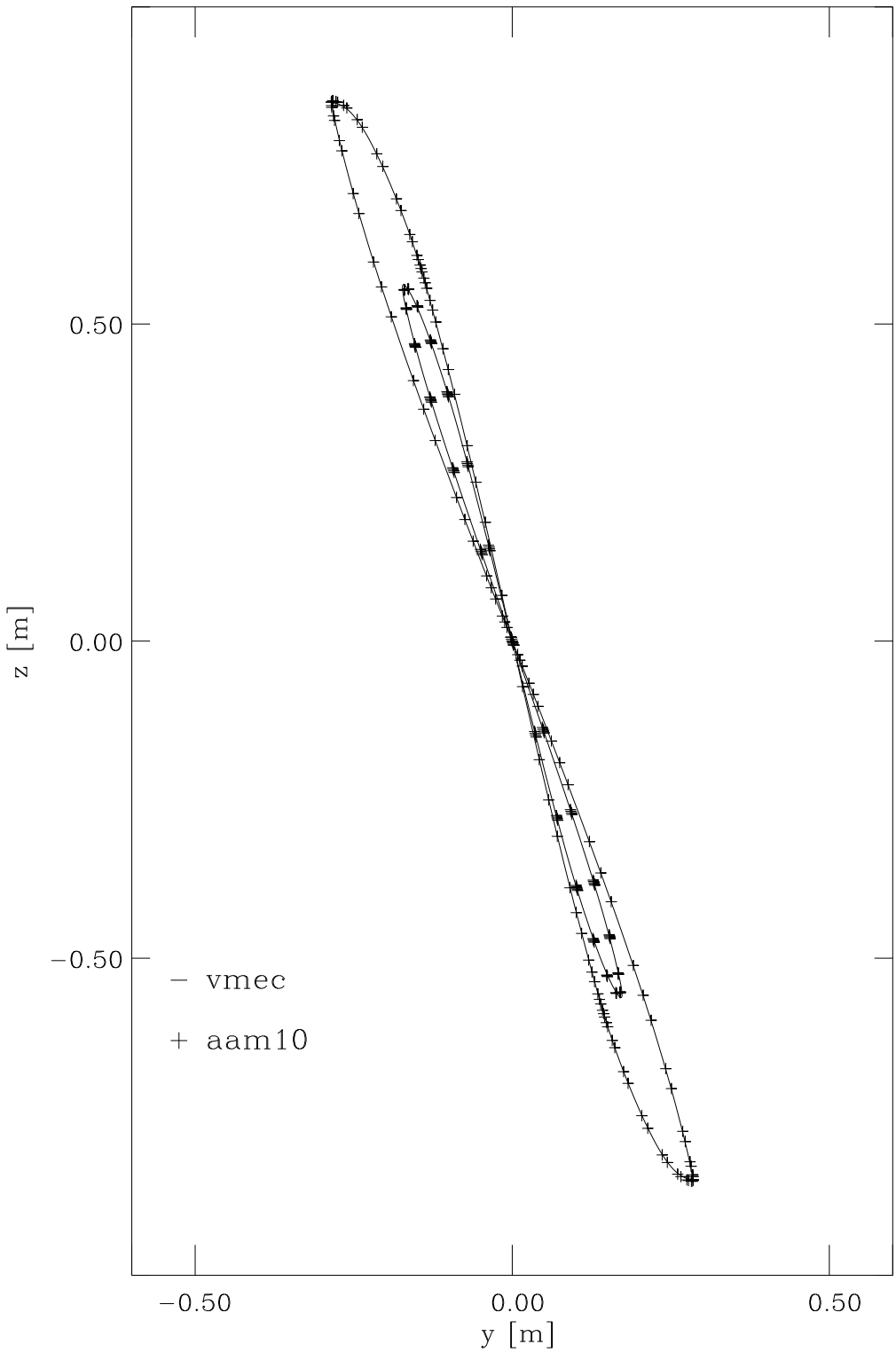

Fig 2.12 Poincare−plot s=1.00 and s=0.4, Φ=0

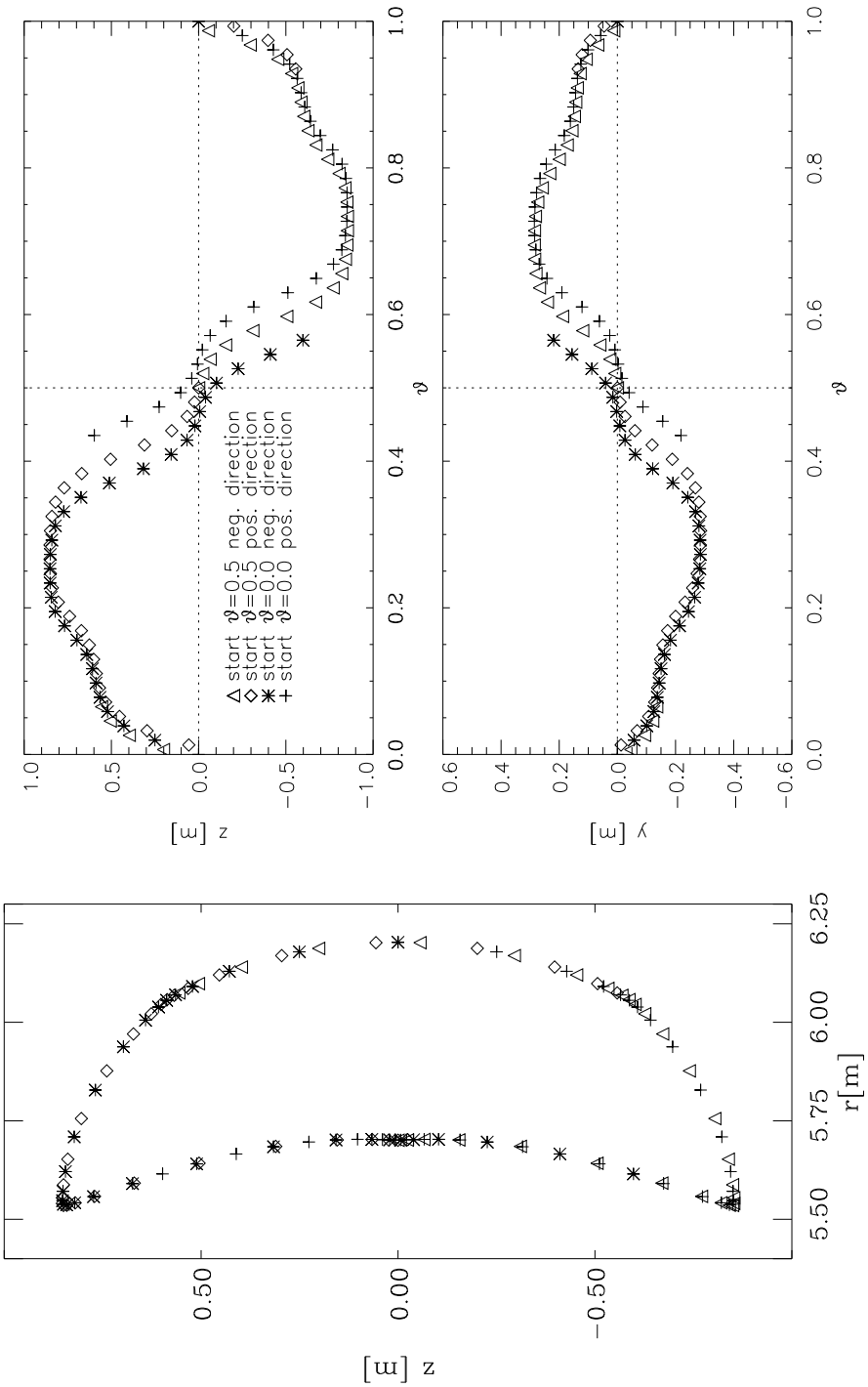

Fig. 2.13 a coordinates of poincareplot z=f(r), z=f(ϑ), y=f(ϑ)

ι= 0.9805 s= 0.6250 startpoints: r_1= 6.2031m r_2= 5.7006m

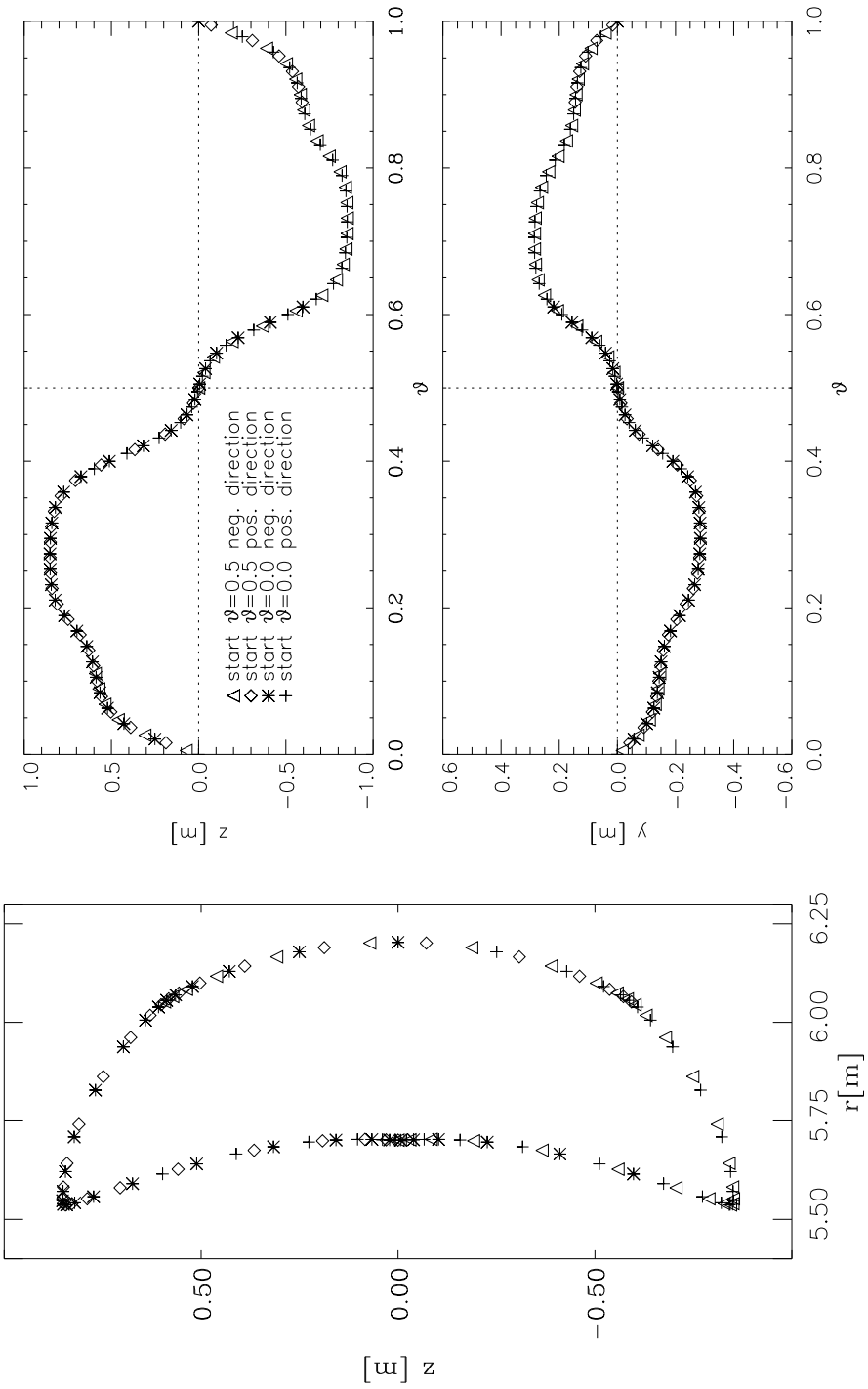

Fig. 2.13 b coordinates of poincareplot z=f(r), z=f(ϑ), y=f(ϑ)

ι= 0.9789 s= 0.6250 startpoints: r_1= 6.2031m r_2= 5.7011m

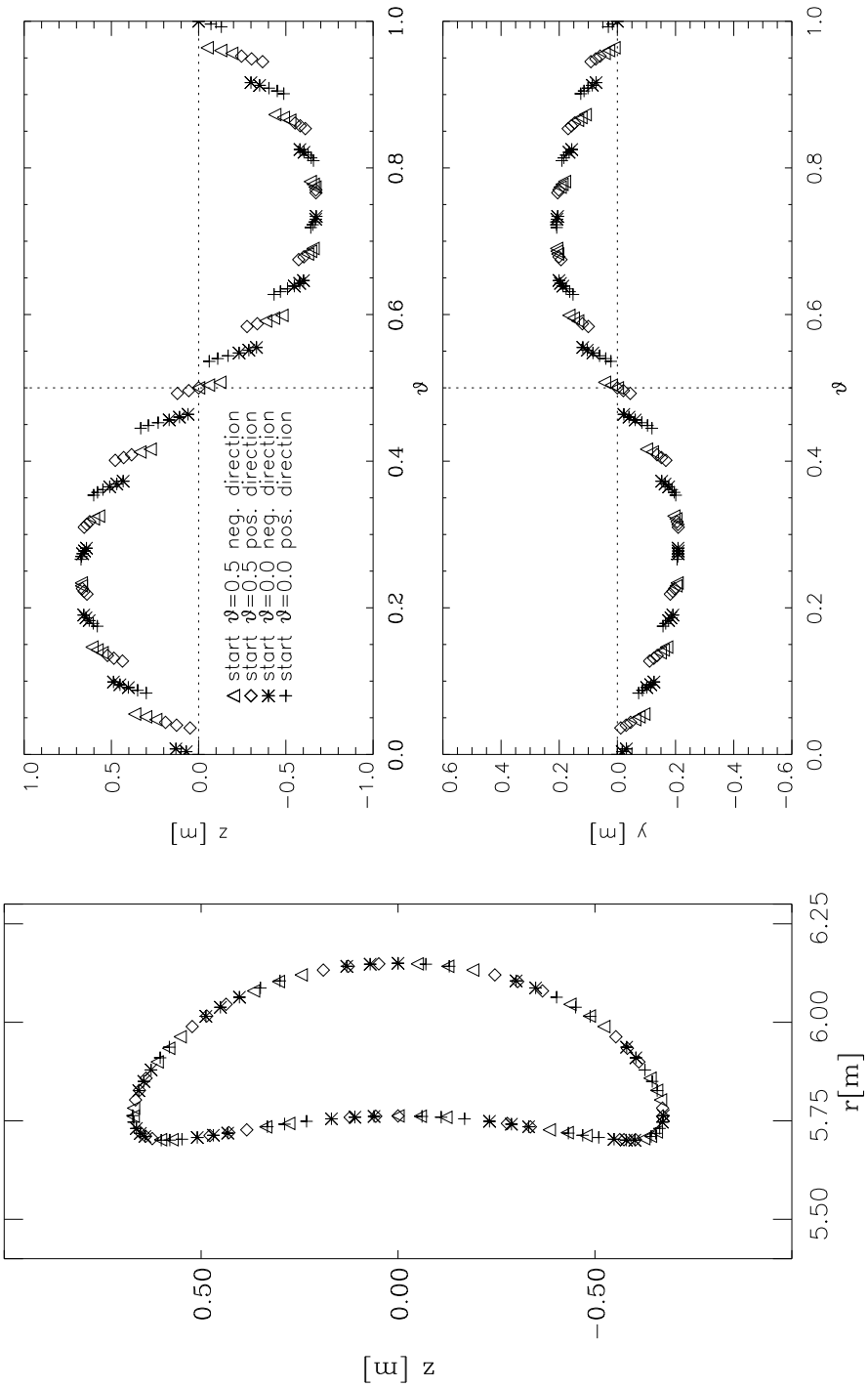

Fig. 2.14 a coordinates of poincareplot z=f(r), z=f(ϑ), y=f(ϑ)

ι= 0.9087 s= 0.3750 startpoints: r_1= 6.1496m r_2= 5.7622m

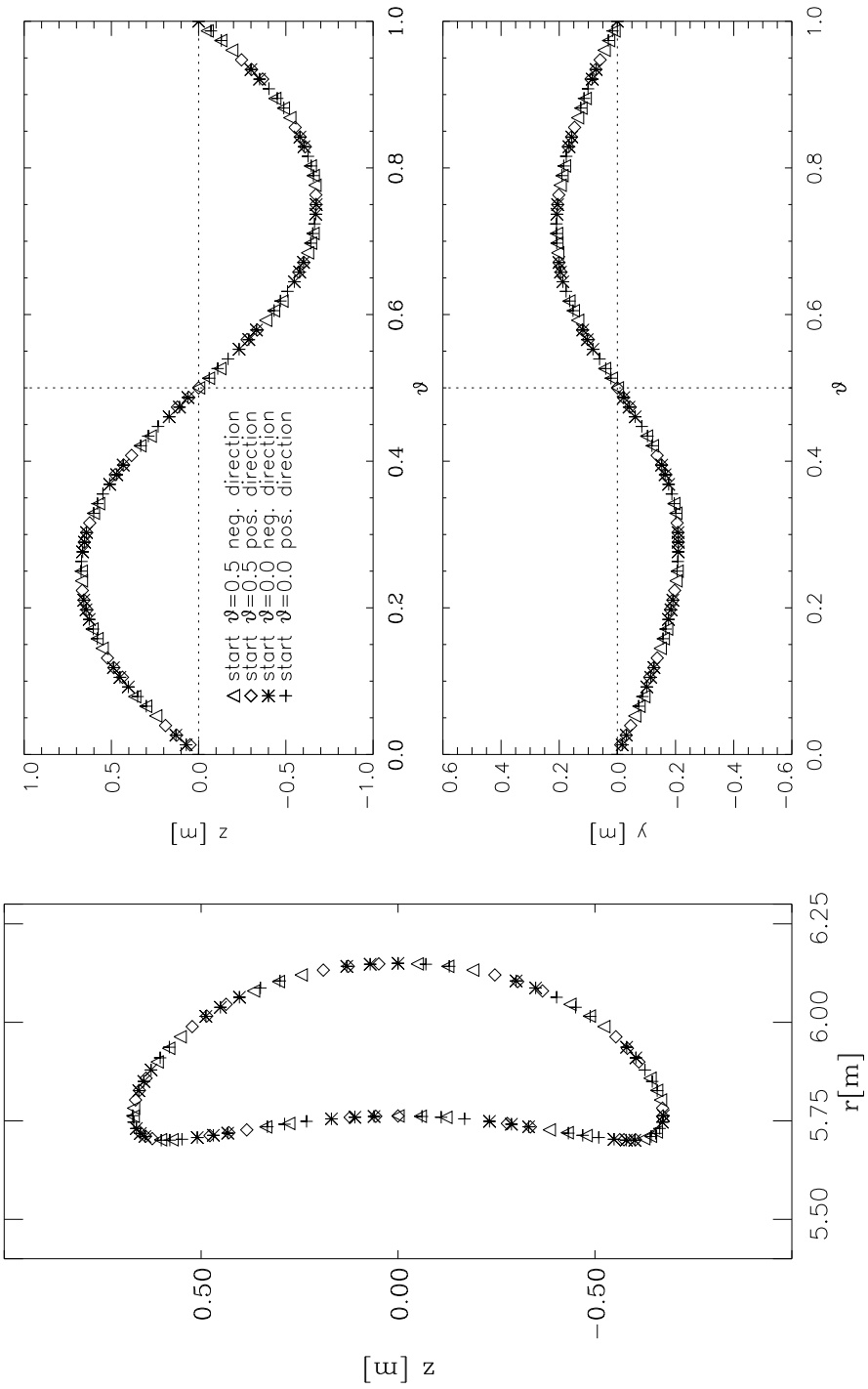

Fig. 2.14 b coordinates of poincareplot z=f(r), z=f(ϑ), y=f(ϑ)

ι= 0.9079 s= 0.3750 startpoints: r_1= 6.1496m r_2= 5.7622m

2.9 Computation of ∇s and g^{ss}

We now follow the Nemov algorithm, see Section 1.11 and Section 1.12, using the Clebsch description of the magnetic field. It is defined:

$$\vec{B} = \nabla\psi \times (\nabla\theta - \iota\nabla\zeta) \tag{2.44}$$

$$P = \frac{\partial\psi}{\partial R}, \quad Q = \frac{\partial\psi}{\partial\varphi}, \quad G = \frac{\partial\psi}{\partial z} \tag{2.45}$$

The following system of differential equations are solved:

$$\frac{dP}{d\varphi} = -\frac{R}{B_\varphi}\left(\frac{\partial B_R}{\partial R}\cdot P + \frac{\partial B_\varphi/R}{\partial R}\cdot Q + \frac{\partial B_z}{\partial R}\cdot G\right) \tag{2.46}$$

$$\frac{dQ}{d\varphi} = -\frac{R}{B_\varphi}\left(\frac{\partial B_R}{\partial \varphi}\cdot P + \frac{1}{R}\frac{\partial B_\varphi}{\partial \varphi}\cdot Q + \frac{\partial B_z}{\partial \varphi}\cdot G\right) \tag{2.47}$$

$$\frac{dG}{d\varphi} = -\frac{R}{B_\varphi}\left(\frac{\partial B_R}{\partial z}\cdot P + \frac{1}{R}\frac{\partial B_\varphi}{\partial z}\cdot Q + \frac{\partial B_z}{\partial z}\cdot G\right) \tag{2.48}$$

The initial conditions are:

$$P_0 = \frac{\partial F_T}{\partial R}, \quad Q_0 = 0, \quad G_0 = 0 \tag{2.49}$$

The values B_x, B_y, B_z and their derivatives were interpolated with the help of the cubic spline method. A local matrix of $12 \times 12 \times 12$ points was used to estimate the values in the centre of the cube.
The modified Euler method is used for the numerical solution of the system of differential equations. This is a Runge-Kutta method of second order.

$$\begin{aligned} F^*_{i+1} &= F_i + F_i^{'}\cdot\Delta x \\ F_{i+1} &= F_i + 0.5\cdot(F_i^{'} + F_{i+1}^{*'})\cdot\Delta x \end{aligned} \tag{2.50}$$

$$\nabla s = \frac{1}{F_T(\Psi_{sep})}\cdot\left(P\cdot\hat{e}_R + \frac{Q}{R}\cdot\hat{e}_\varphi + G\cdot\hat{e}_z\right) \tag{2.51}$$

The coefficient g^{ss} is:

$$g^{ss} = |\nabla s|^2 = \frac{1}{F_T(\Psi_{sep})^2}\cdot\left(P^2 + \frac{Q^2}{r^2} + G^2\right) \tag{2.52}$$

In some cases (near small island chains or at the edge of the ergodic range) the dispersion of the solution of differential equation 2.46 – 2.48 increases strongly with the length of fieldline. Therefore it is necessary to reduce the number of turns and use a weighted averaging, making use of the periodicity of the system, such that the results of the first few turns are weighed more must than the last.
Figures 2.15 a and 2.16 a show the solutions of P, Q, G and g^{ss} along a fieldline (one startpoint in one direction) with 50 turns and without weighting, in the vicinity of the $\iota = 10/11$ island chain. The comparison with `VMEC` results (Figure 2.15 a) shows the bad results for g^{ss}.
Reducing the number of turns, weighting the results and using four fieldlines (two start points in two directions) improves the quality of the solution considerably, see Figures 2.15 b, 2.16 b, 2.15 c and 2.16 c. For the analysis, only ten turns are used and the first five turns are weighted double.
The Figures 2.15 d, 2.15 e, 2.16 d and 2.16 e show results for examples $s = 0.20$ and $s = 0.96$, where the dispersion is small.
Figure 2.17 shows all results of g^{ss}. The influence of the five islands is recognisable in the shape of the curves. The calculation of $g^{ss}(s)$ at a flux surface is independent of the neighbouring flux surface. In comparison with `VMEC` data the values has a good agreement.

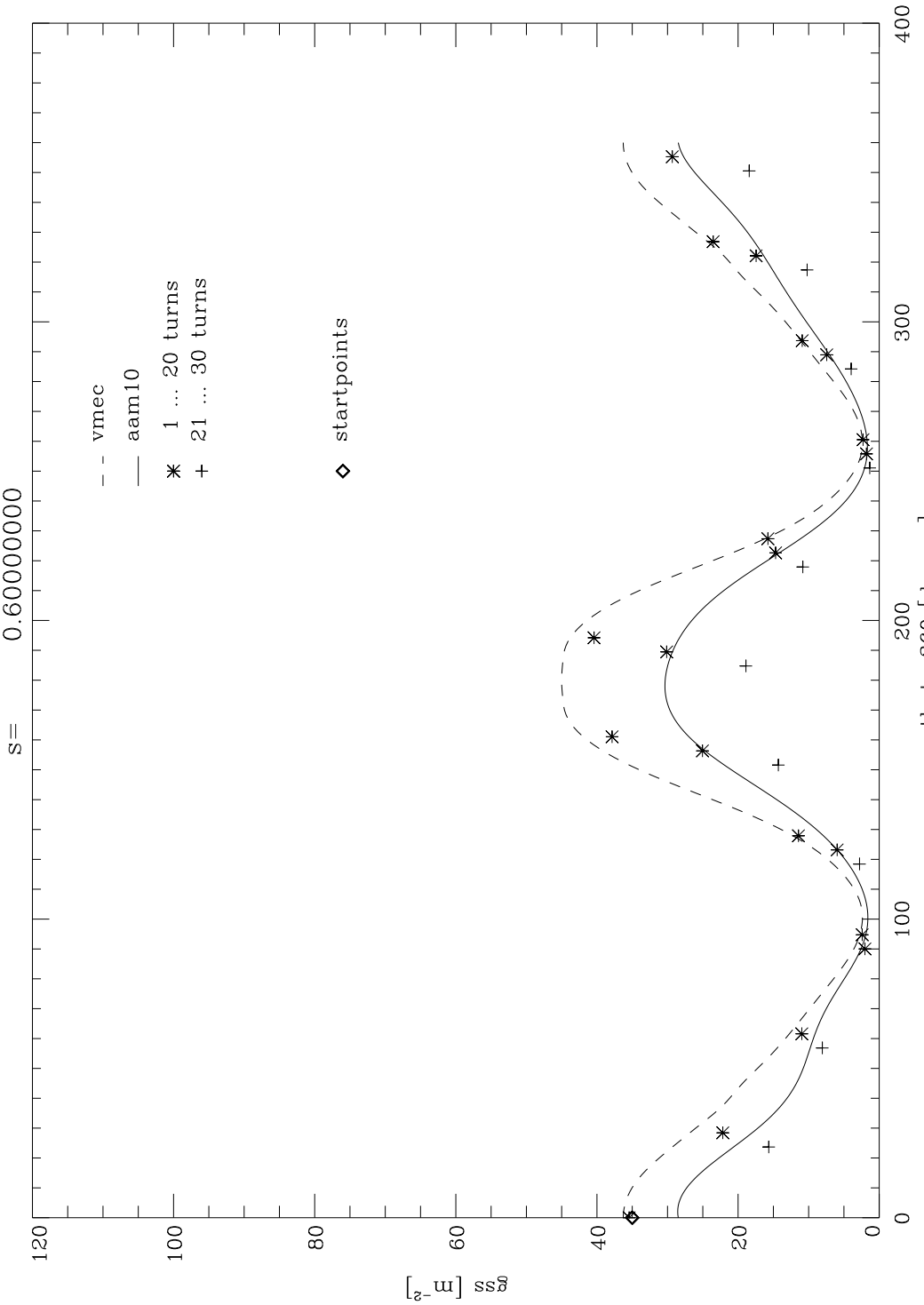

Fig 2.15 a gss $[m^{-2}]$ 1 startpoint (1 x 50 turns) s=0.6000

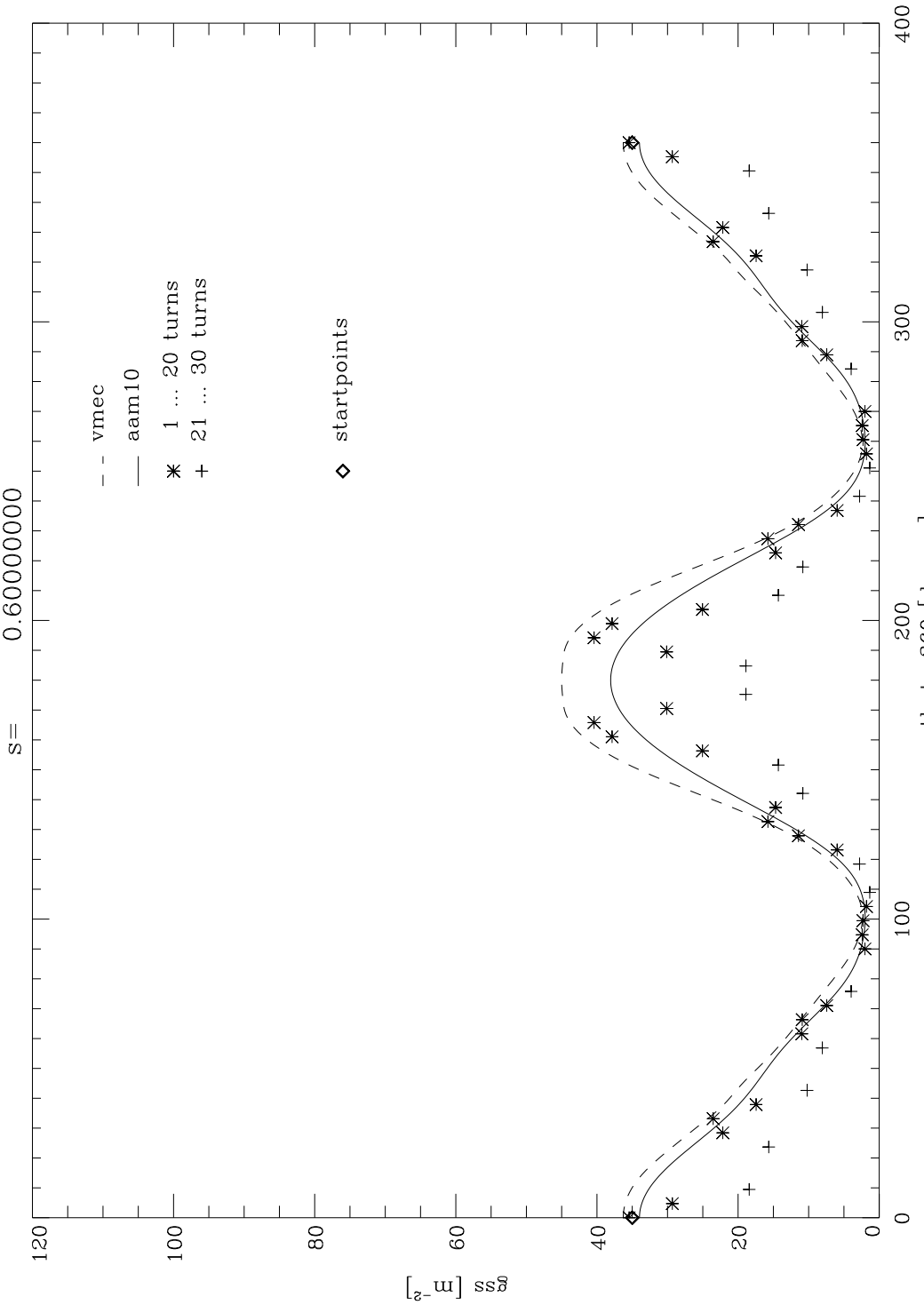

Fig 2.15 b gss $[m^{-2}]$ 2 startpoints (2 x 30 turns) s=0.6000

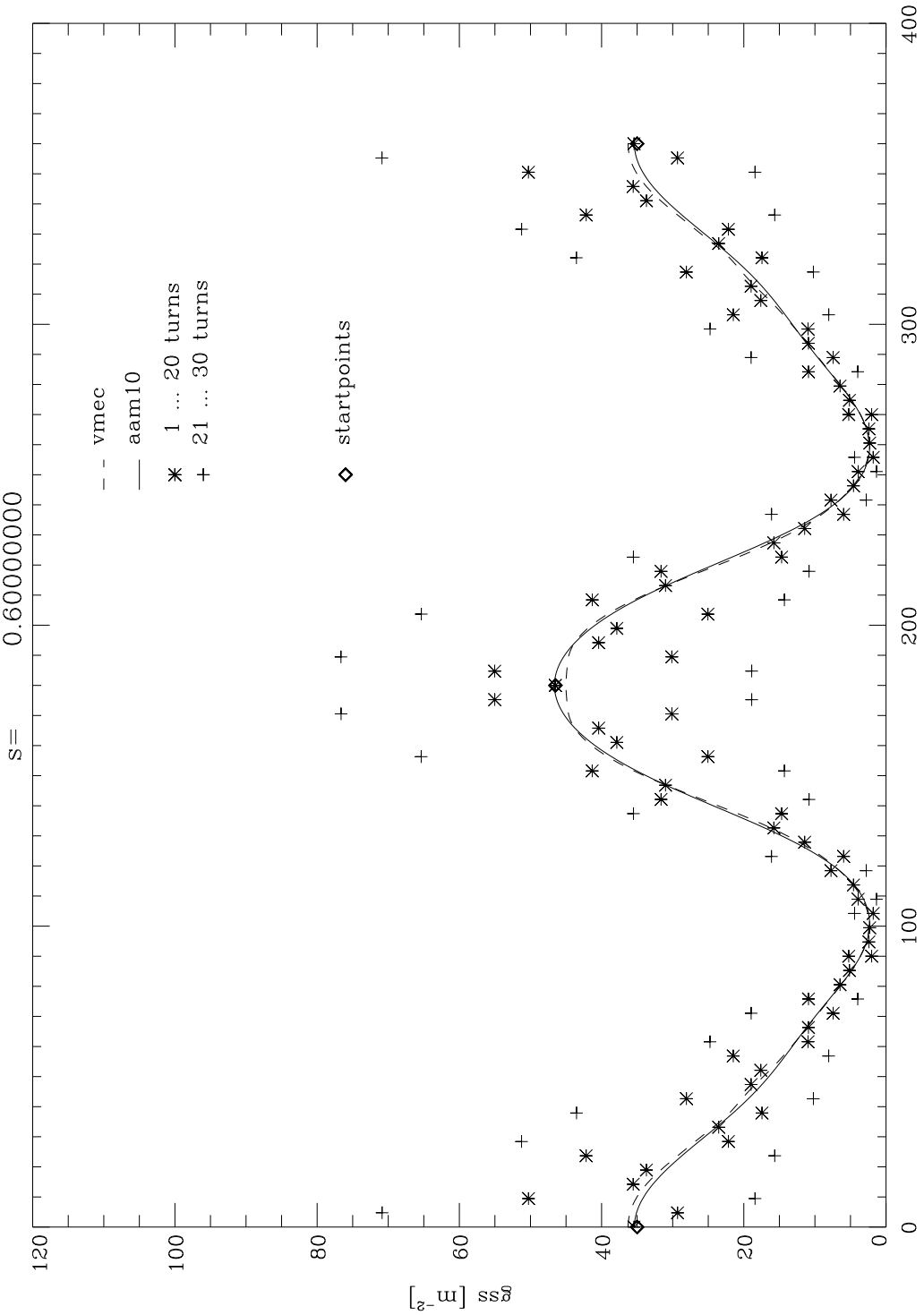

Fig 2.15 c gss $[m^{-2}]$ 4 startpoints (4 x 30 turns) s=0.6000

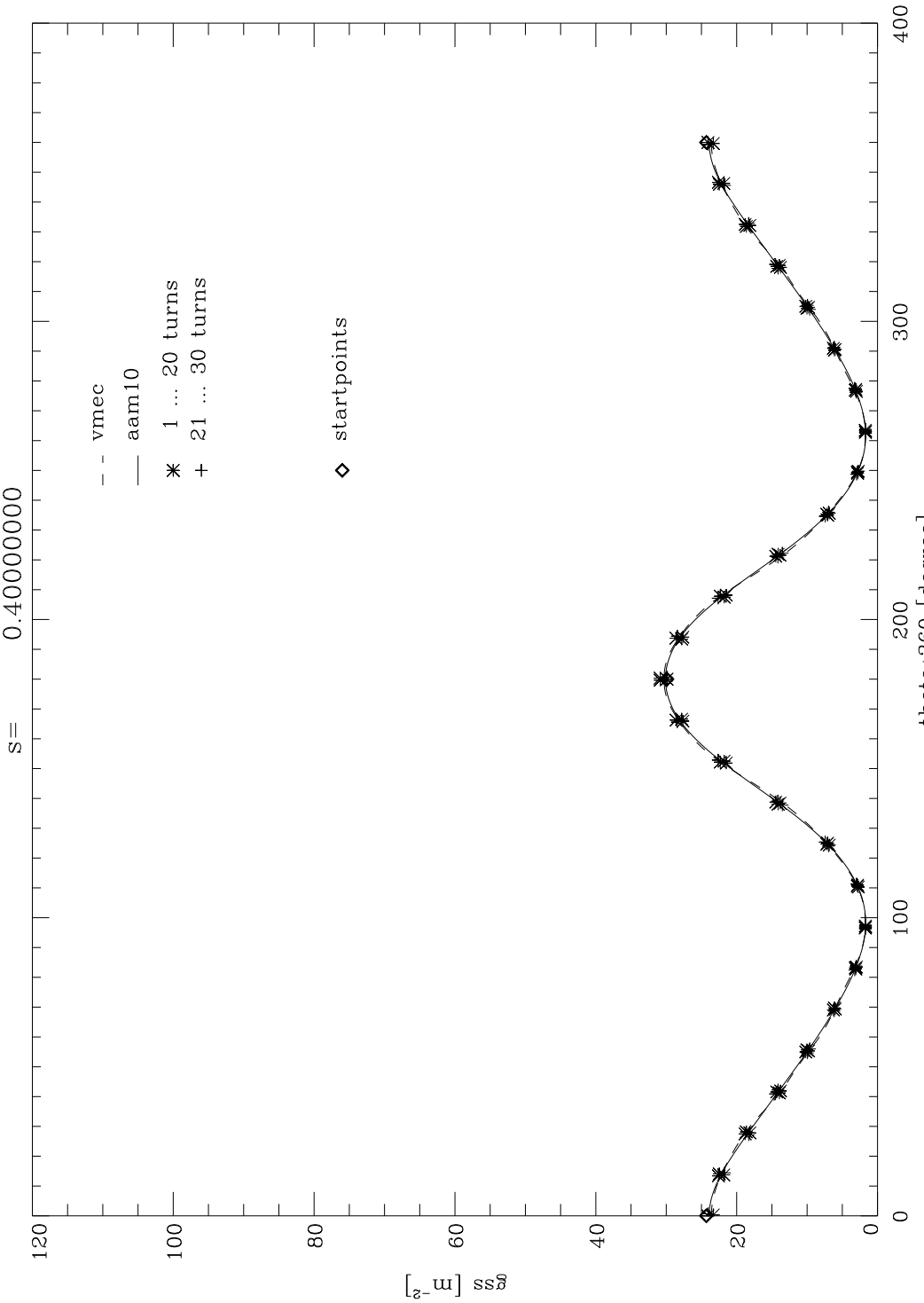

Fig 2.15 d gss $[m^{-2}]$

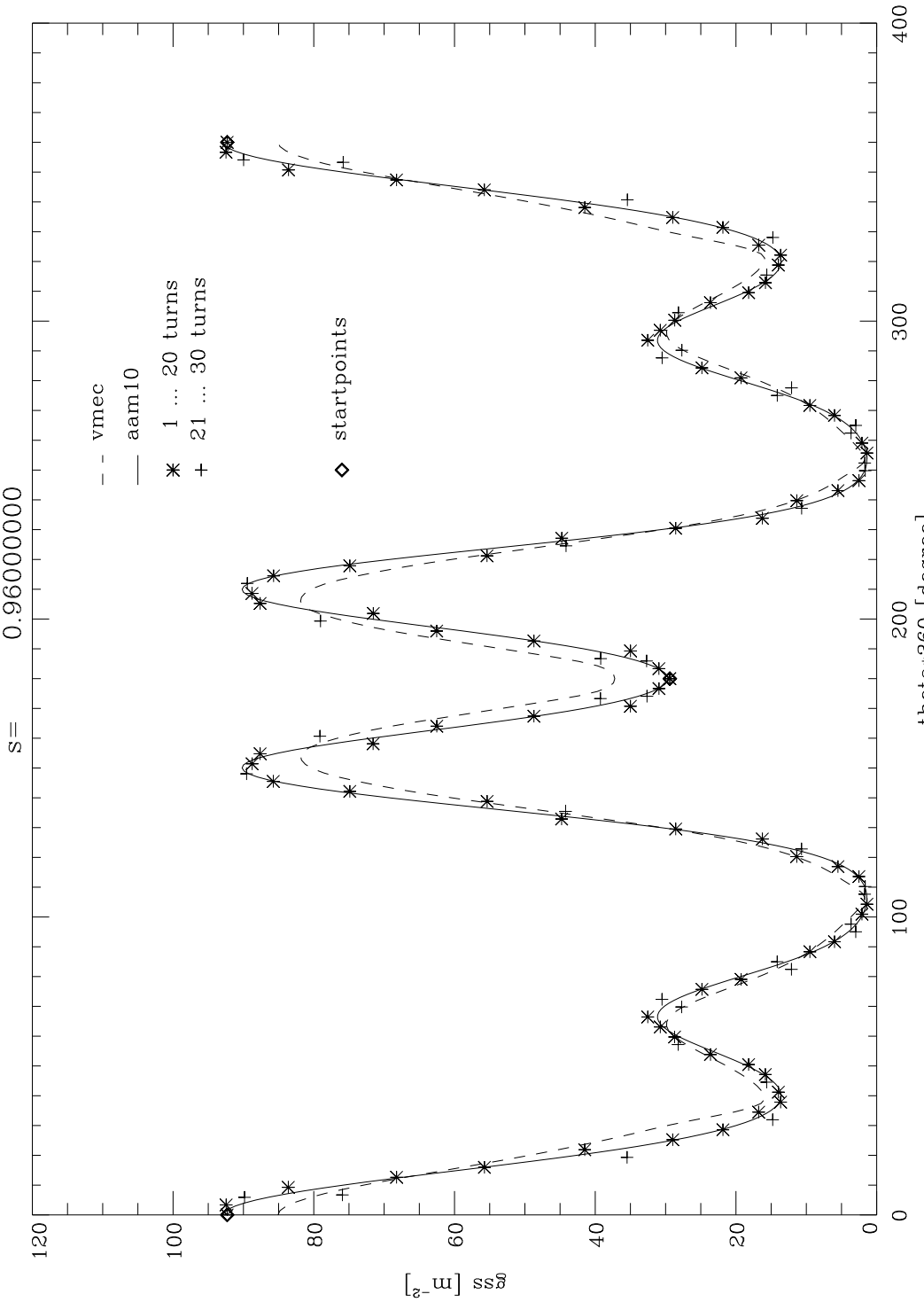

Fig 2.15 e gss $[m^{-2}]$

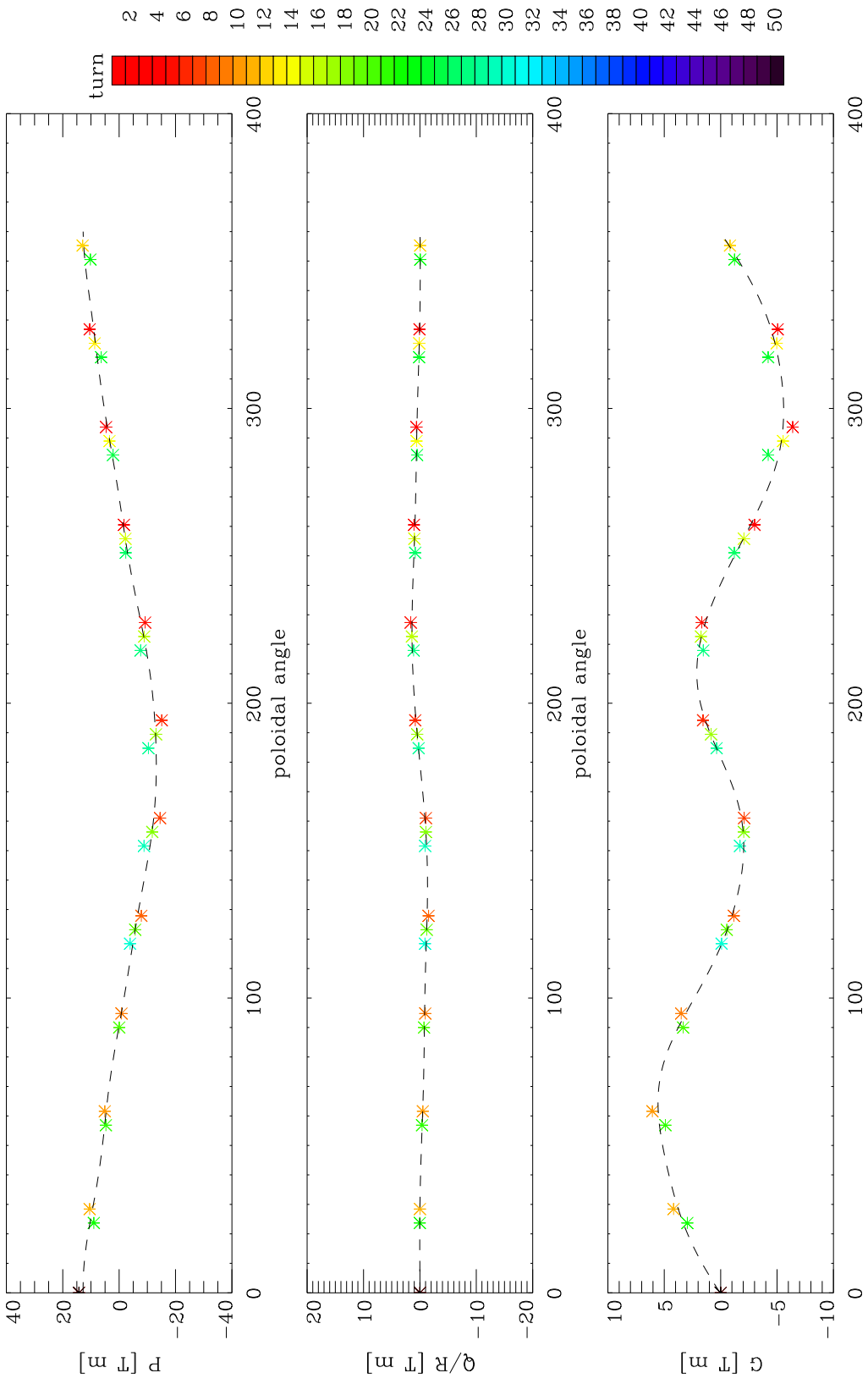

Fig 2.16 a P Q and G, 1 startpoint (1 x 50 turns) s=0.6000

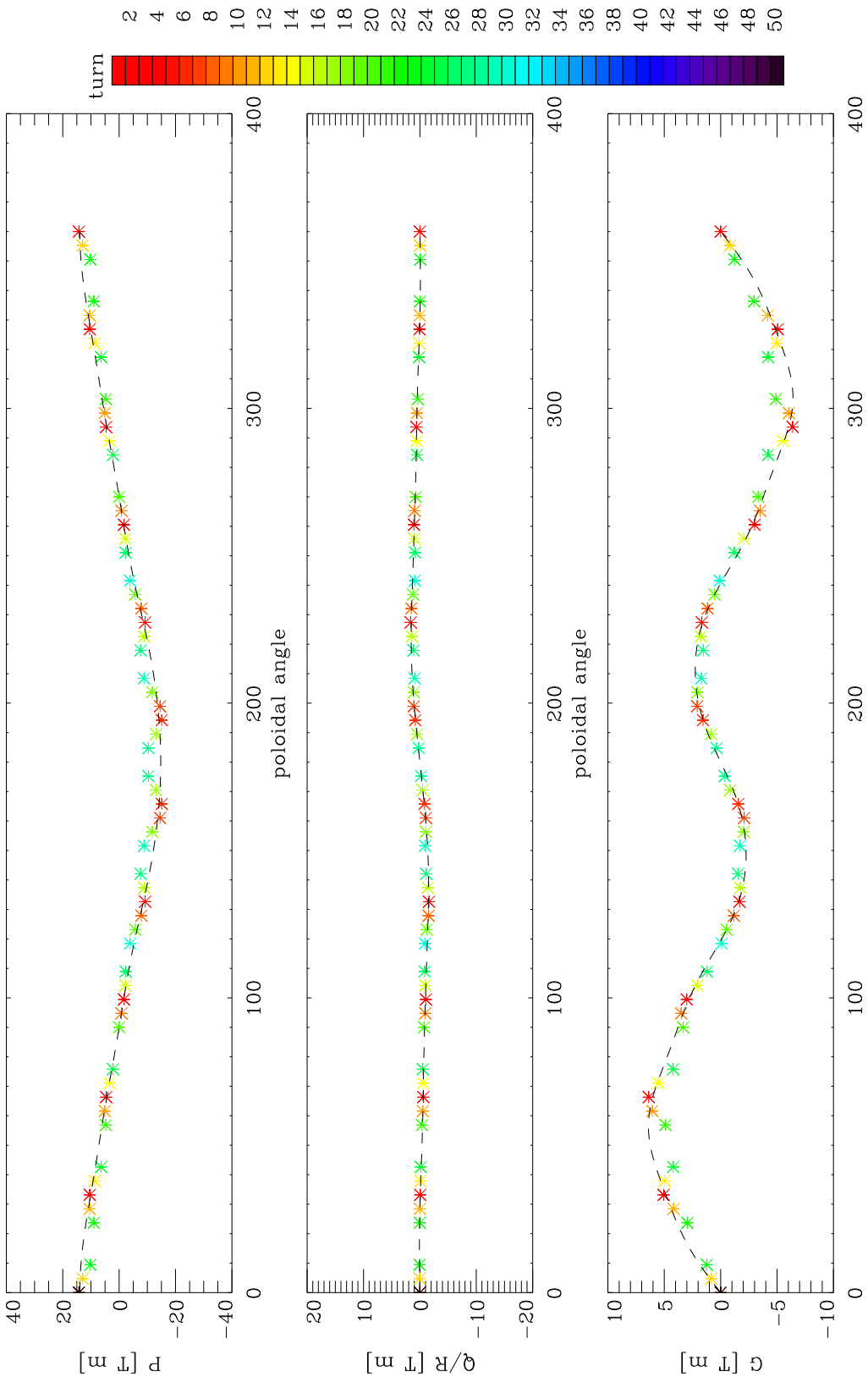

Fig 2.16 b P Q and G, 2 startpoints (2 x 30 turns) s=0.6000

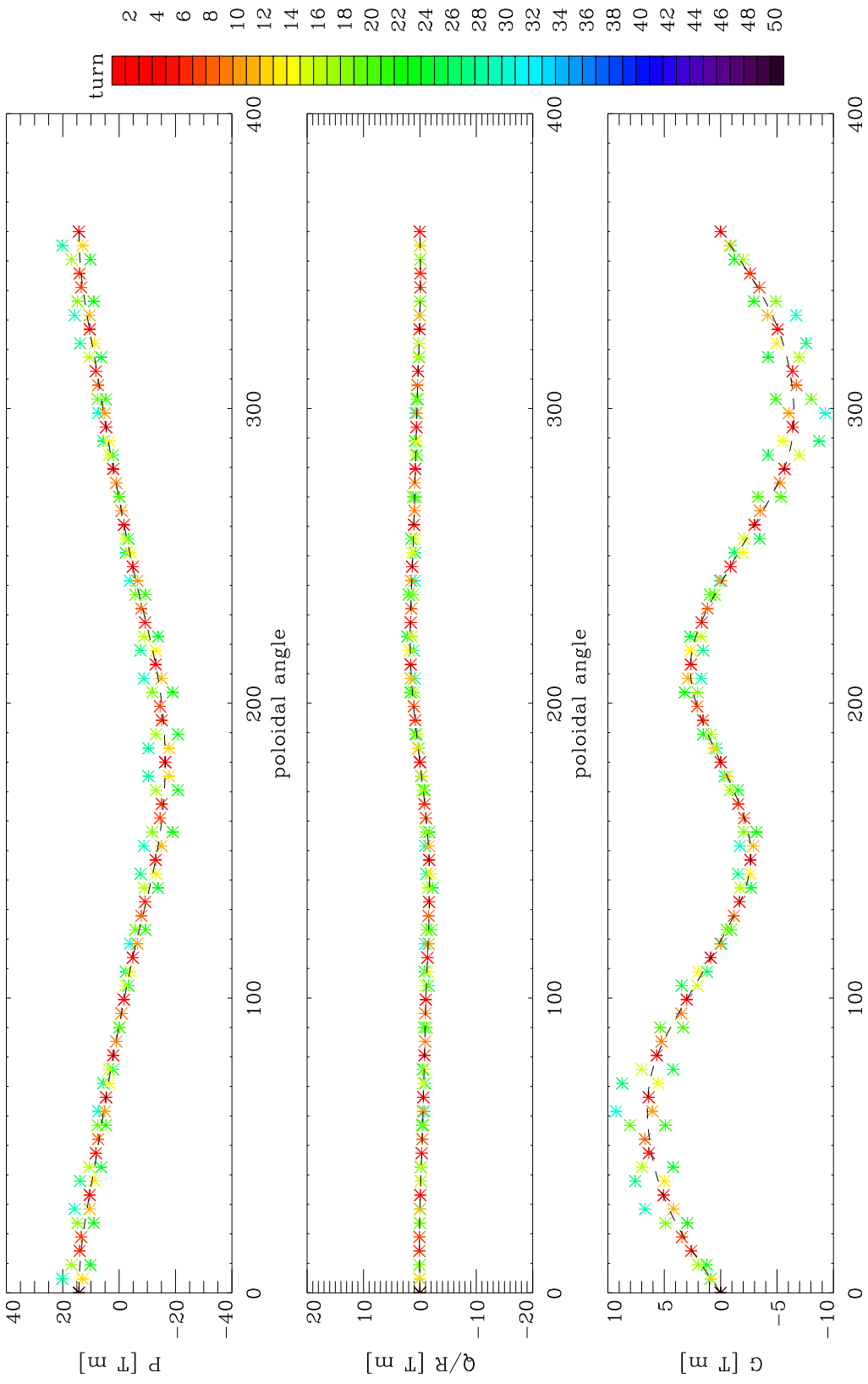

Fig 2.16 c P Q and G, 4 startpoints (4 x 30 turns) s=0.6000

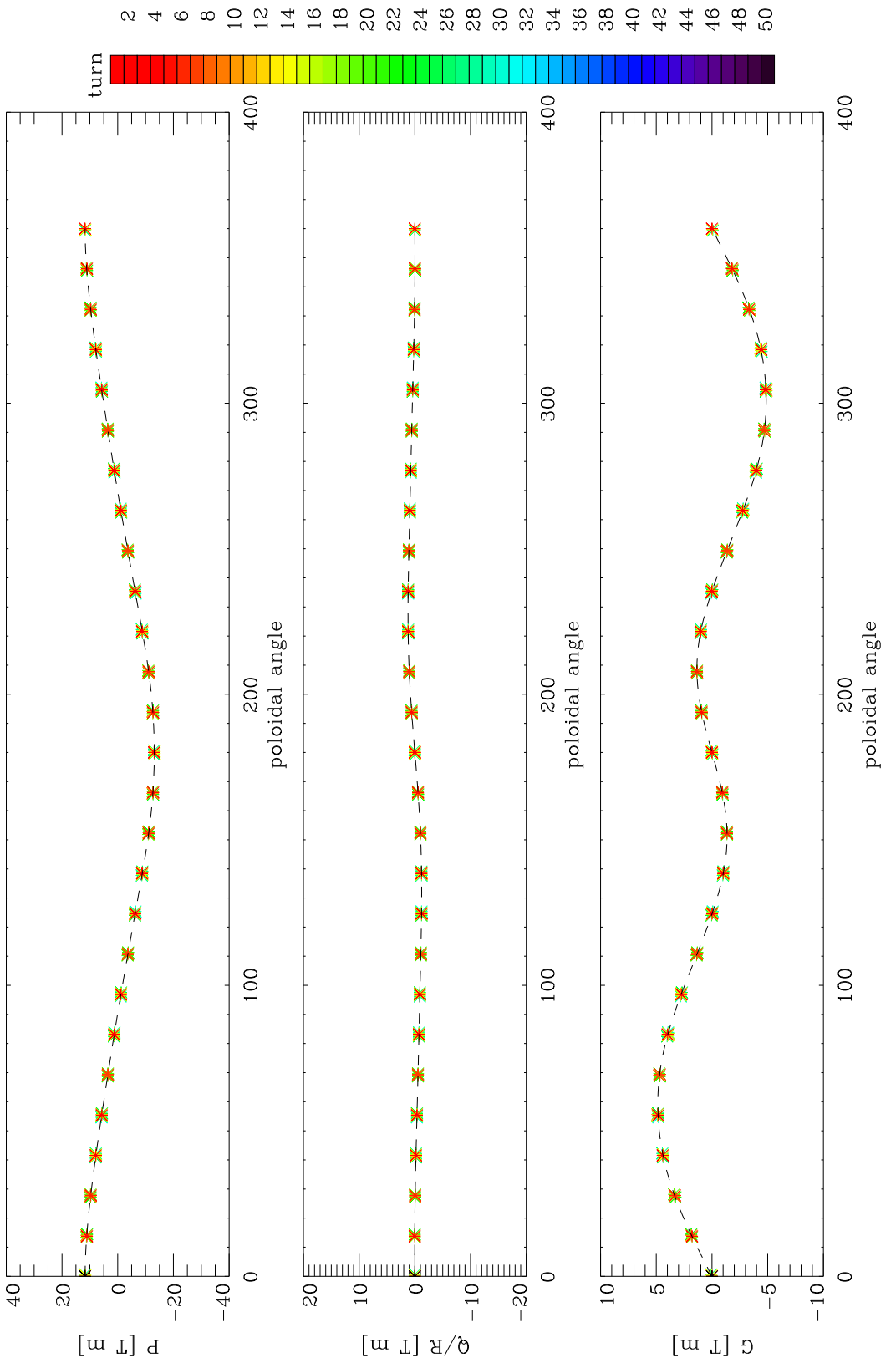

Fig 2.16 d P Q and G s=0.4000

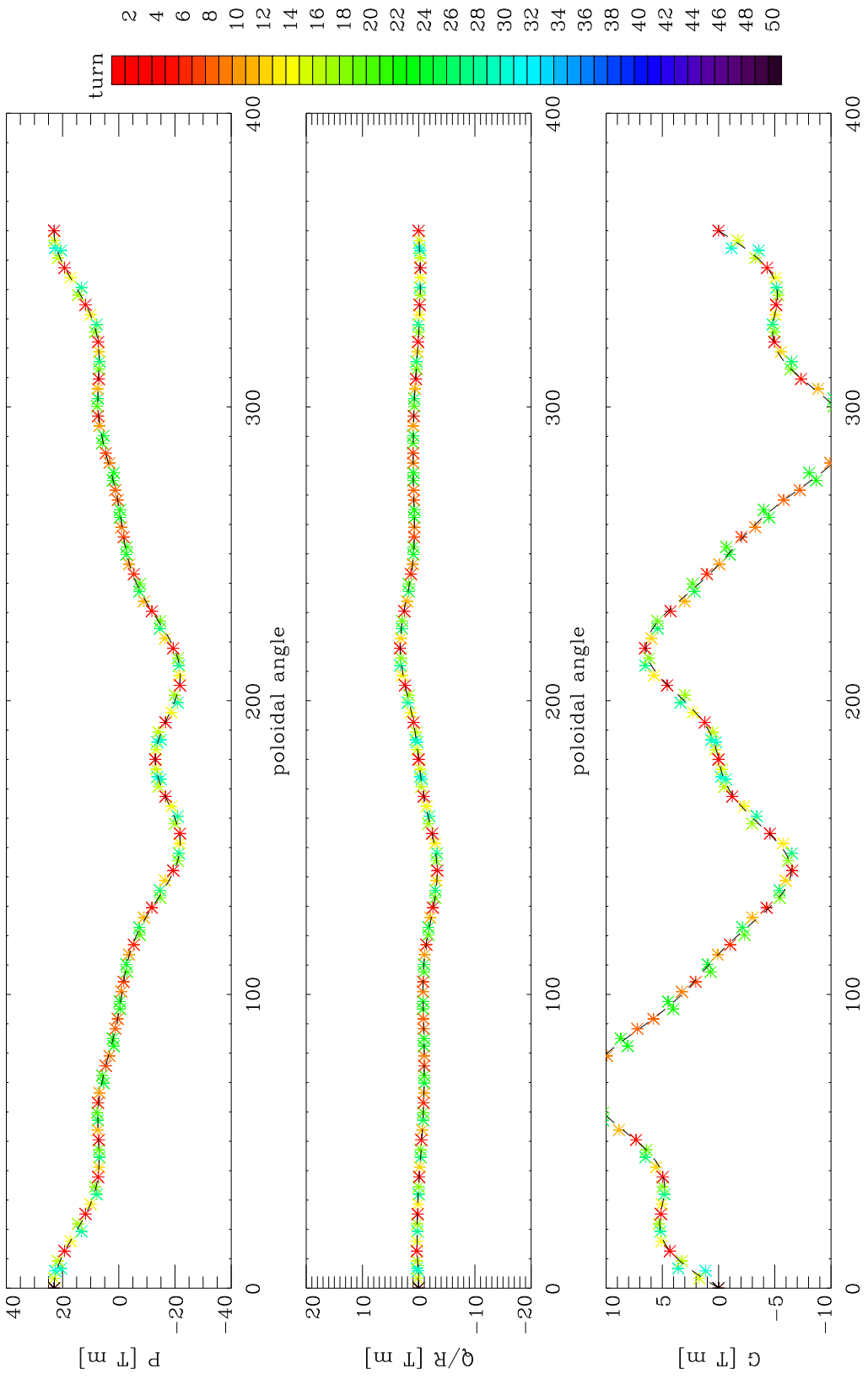

Fig 2.16 e P Q and G s=0.9600

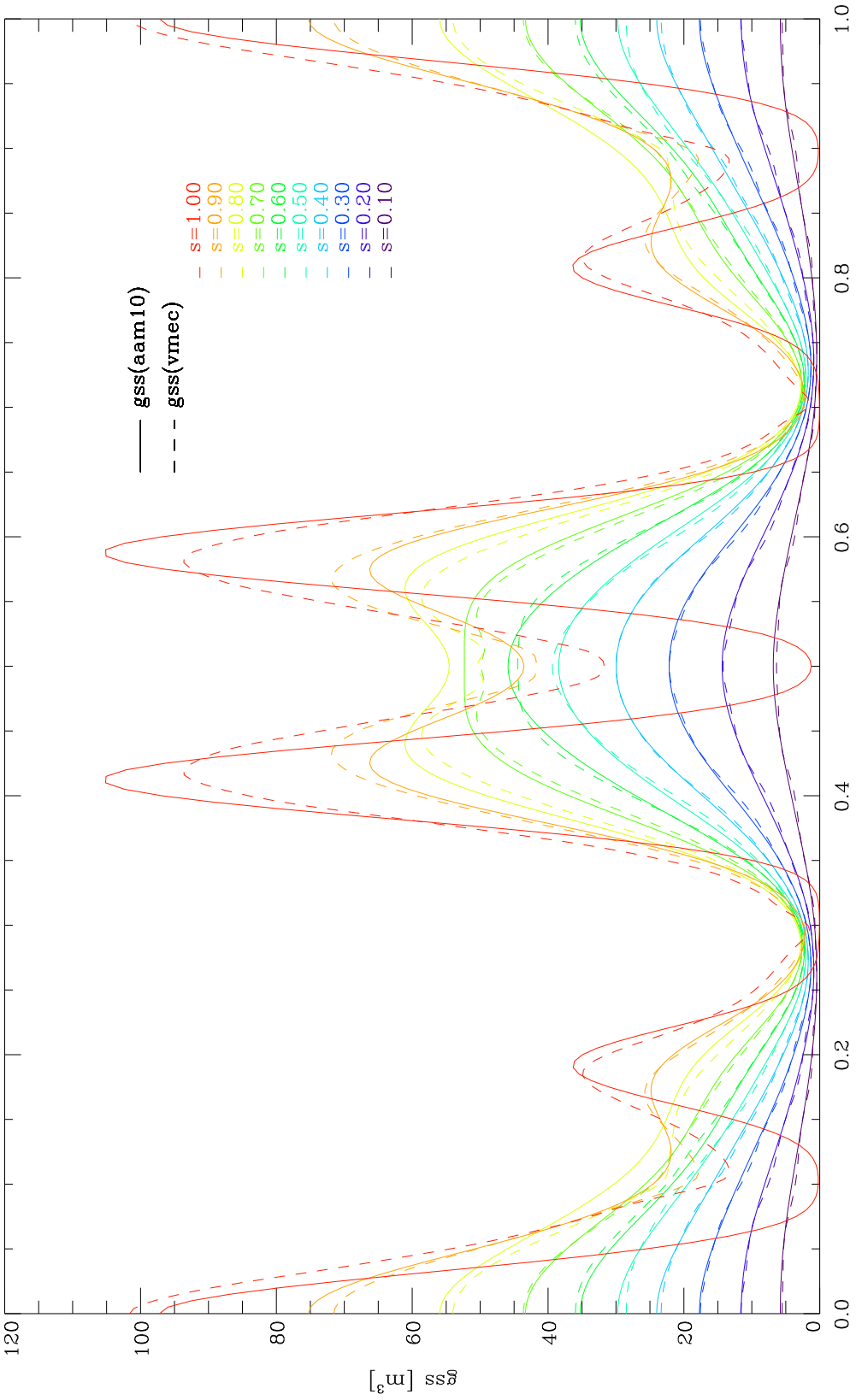

Fig 2.17 g^{ss} $[m^{-2}]$ ϕ=0 vacuum magnetic field

2.10 Calculation of coefficients $\tilde{\sigma}$, $\tilde{\beta}$, $g_{s\vartheta}$, $g^{\phi s}$, $g^{s\vartheta}$

The covariant basis vectors, see Section 1.13, are:

$$\vec{e}_s = \frac{\partial \vec{R}}{\partial s} \tag{2.53}$$

$$\vec{e}_\vartheta = \frac{\partial \vec{R}}{\partial \vartheta} \tag{2.54}$$

$$\vec{e}_\phi = \frac{\partial \vec{R}}{\partial \phi} \tag{2.55}$$

The coefficients $g_{s\vartheta}$ and $g_{s\phi}$, see Section 1.14, are:

$$g_{s\vartheta} = \vec{e}_s \cdot \vec{e}_\vartheta \tag{2.56}$$

$$g_{s\vartheta} = \frac{\partial R}{\partial s} \cdot \frac{\partial R}{\partial \vartheta} + R \cdot \frac{\partial \varphi}{\partial s} \cdot R \cdot \frac{\partial \varphi}{\partial \vartheta} + \frac{\partial z}{\partial s} \cdot \frac{\partial z}{\partial \vartheta} \tag{2.57}$$

$$g_{s\phi} = \vec{e}_s \cdot \vec{e}_\phi \tag{2.58}$$

$$g_{s\phi} = \frac{\partial R}{\partial s} \cdot \frac{\partial R}{\partial \phi} + R \cdot \frac{\partial \varphi}{\partial s} \cdot R \cdot \frac{\partial \varphi}{\partial \phi} + \frac{\partial z}{\partial s} \cdot \frac{\partial z}{\partial \phi} \tag{2.59}$$

Figure 2.18 shows a comparison of the $g_{s\vartheta}$ coefficient with `VMEC` results. For s greater then 0.9 then great differences between the values are found.

The covariant component $\tilde{\beta}$, see Section 1.13, is:

$$\tilde{\beta} = \vec{B} \cdot \vec{e}_s \tag{2.60}$$

$$\tilde{\beta} = B_r \cdot \frac{\partial R}{\partial s} + B_\varphi \cdot R \cdot \frac{\partial \varphi}{\partial s} + B_z \cdot \frac{\partial z}{\partial s} \tag{2.61}$$

or

$$\tilde{\beta} = -\frac{1}{\sqrt{g}} \left(F'_T \cdot g_{s\phi} + F'_P \cdot g_{s\vartheta} \right) \tag{2.62}$$

In the case of vacuum field (zero plasma pressure) $\tilde{\beta}$ is zero.

2 Comparison with numerical results from the VMEC program

A simple way to get the derivatives is to use the function of $r(s,\vartheta,\Phi)$, $\varphi(s,\vartheta,\Phi)$ and $z(s,\vartheta,\Phi)$, see Equations 2.40 – 2.43 and Figures 2.13 b and 2.14 b.

assumption: Φ = constant

$$R(s,\vartheta) = \sum_{i,j} \left(a_{Ri}\cdot s^i\right)\cdot\left(b_{Rj}\cdot sin\left(\vartheta\cdot j\right)+c_{Rj}\cdot cos\left(\vartheta\cdot j\right)\right) \tag{2.63}$$

$$\varphi(s,\vartheta) = \sum_{i,j} \left(a_{pi}\cdot s^i\right)\cdot\left(b_{pj}\cdot sin\left(\vartheta\cdot j\right)+c_{pj}\cdot cos\left(\vartheta\cdot j\right)\right) \tag{2.64}$$

$$z(s,\vartheta) = \sum_{i,j} \left(a_{zi}\cdot s^i\right)\cdot\left(b_{zj}\cdot sin\left(\vartheta\cdot j\right)+c_{zj}\cdot cos\left(\vartheta\cdot j\right)\right) \tag{2.65}$$

$$i = 0,4 \qquad j = 1,8 \tag{2.66}$$

The coefficients a_R, b_R, c_R, a_p, b_p, c_p, a_z, b_z, c_z are calculated with the help of the least-squares approach.
A comparison of results for $\Phi = 0$ is shown in Figure 2.19. For $s < 0.9$ the agreement is good.

The other coefficients, see Section 1.14, can be calculated:

$$\tilde{\sigma} = -\frac{1}{F'_T\cdot B}\left[B^2\cdot g_{s\vartheta}-\mu_0 J\cdot\tilde{\beta}\right] \tag{2.67}$$

$$g^{s\phi} = -\frac{F'_T\cdot\tilde{\beta}\cdot g^{ss}+\mu_0 J\cdot\tilde{\sigma}\cdot B}{\mu_0(F'_T\cdot I+F'_P\cdot J)} \tag{2.68}$$

$$g^{s\vartheta} = -\frac{F'_P\cdot\tilde{\beta}\cdot g^{ss}-\mu_0 I\cdot\tilde{\sigma}\cdot B}{\mu_0(F'_T\cdot I+F'_P\cdot J)} \tag{2.69}$$

$g_{s\phi}$ can also calculate :

$$g_{s\phi} = -\frac{\sqrt{g}\cdot\tilde{\beta}+g^{s\vartheta}\cdot F'_P}{F'_T} \tag{2.70}$$

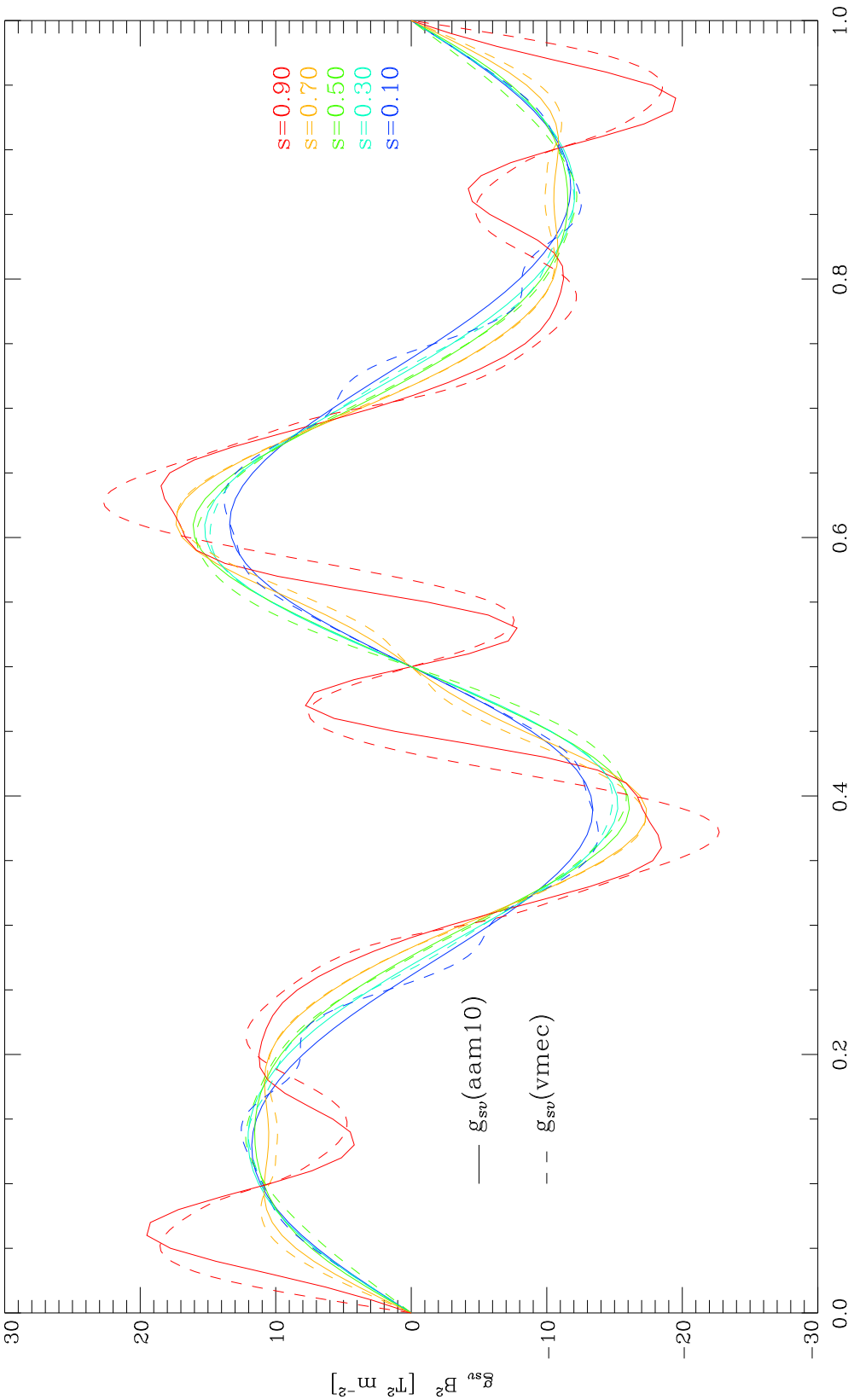

Fig 2.18 $g_{sv} \cdot B^2$ $[T^2\ m^{-2}]$ ϕ=0 vacuum magnetic field

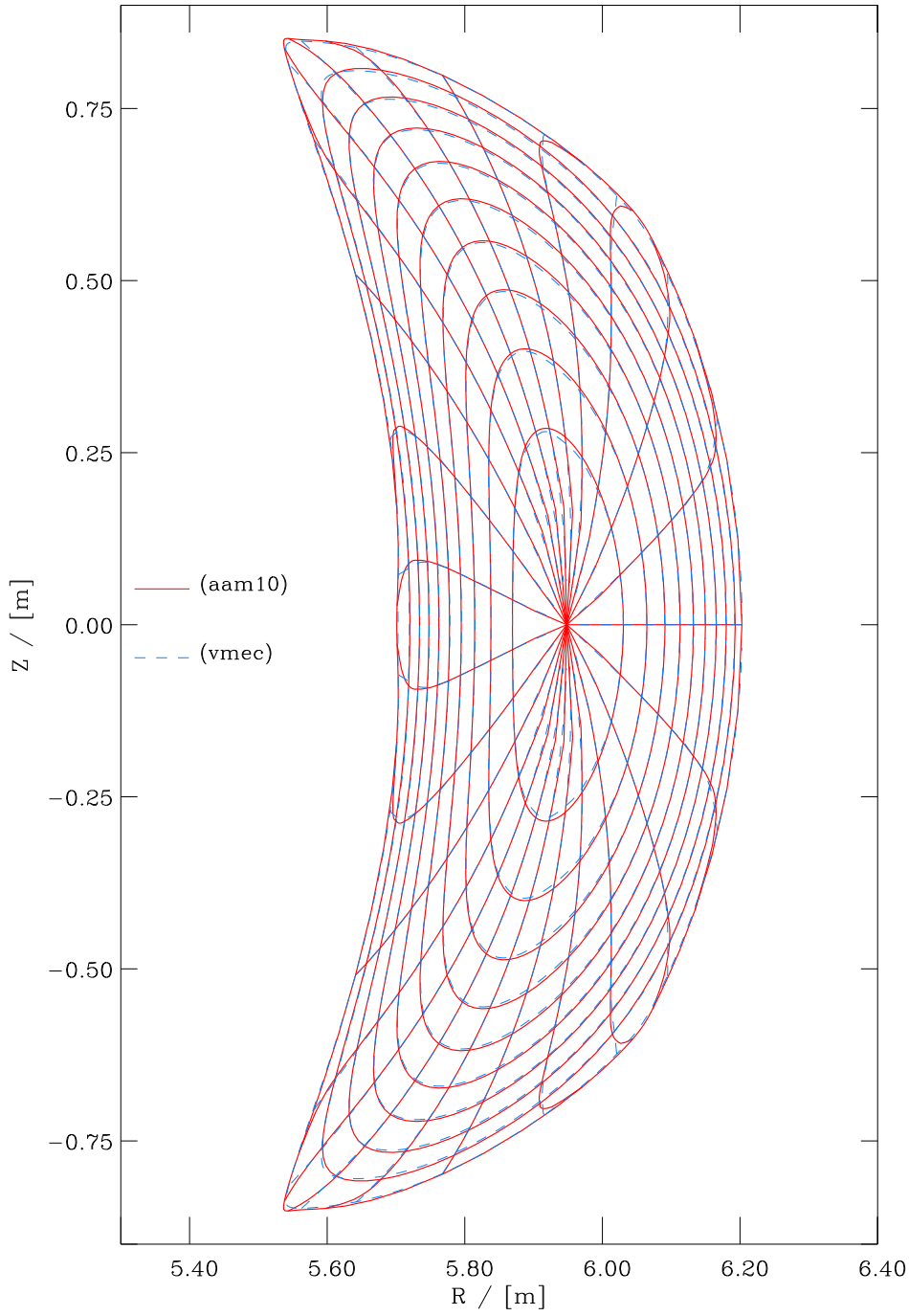

Fig 2.19 Projected R−Z−plane as a function of s and v , ϕ=0

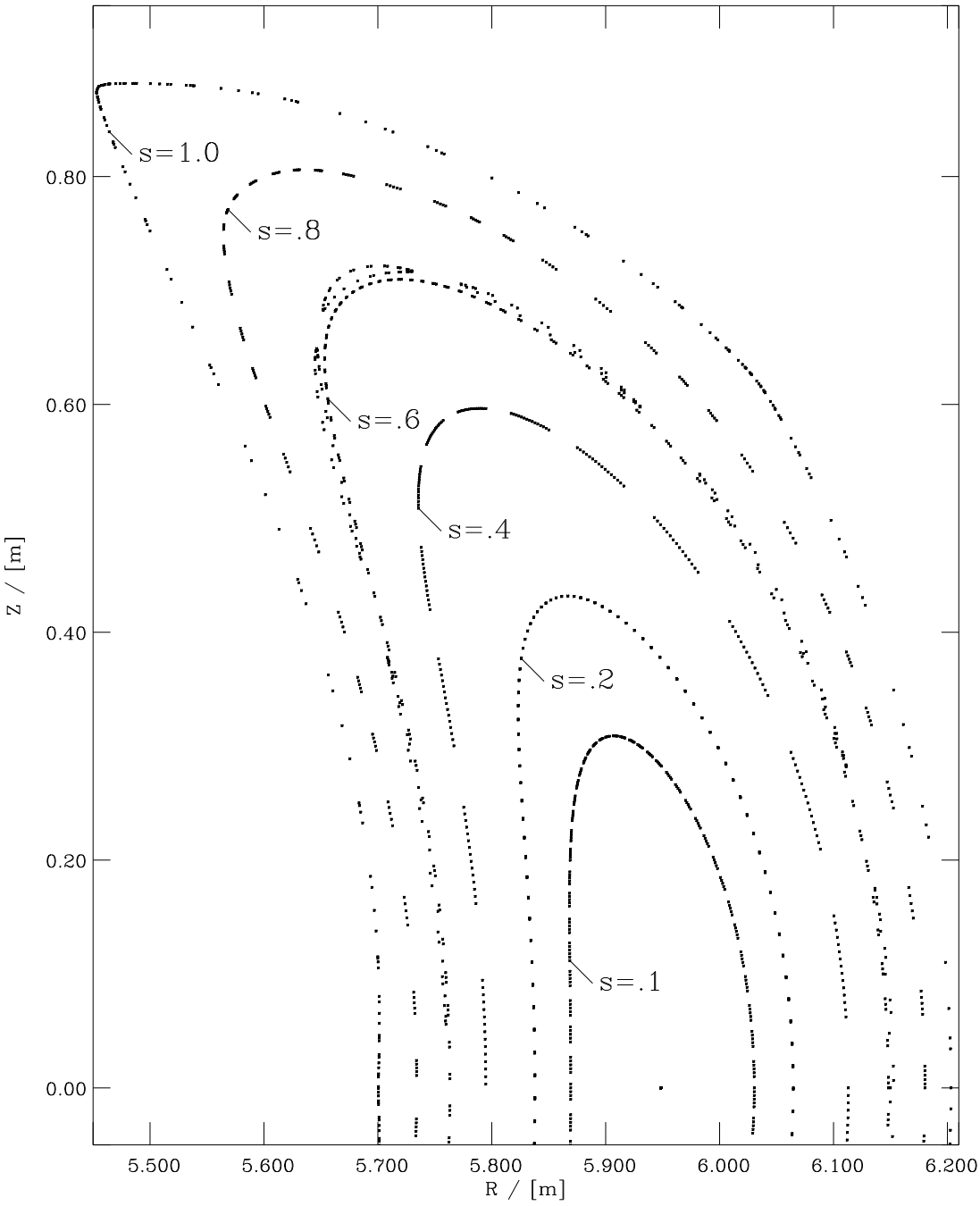

Fig. 2.20 Special poincare–plot vacuum–field φ=0°, 400 turns

3 Comparison with analytical results of a ring magnetic field

3.1 The magnetic field

In order to test this new program, we apply it to the simple case of a circular cross-section system, where the toroidal field is provided by current flowing along a vertical wire at the axis of symmetry, and the toroidal current distribution is a given function of the minor radius ϱ. The components of this analytical ring magnetic field are shown in Figures 3.5 and 3.7.

$$B_\varphi = \frac{B_0}{R} \tag{3.1}$$

$$B_R = \frac{-b \cdot z}{\varrho} \tag{3.2}$$

$$B_z = \frac{b \cdot (R - R_0)}{\varrho} \tag{3.3}$$

$$b = B_1 \cdot \left(\frac{\varrho}{2} - \frac{\varrho^3}{4a^2} \right) \tag{3.4}$$

$$\varrho = \sqrt{(R - R_0)^2 + z^2} \tag{3.5}$$

$$B_0 = 10\ Tm, \quad B_1 = 1\ T/m, \quad R_0 = 6\ m, \quad a = 1\ m \tag{3.6}$$

The input for the program `aam10` was only the magnetic field. The grid resolution of the magnetic field (chosen to match that of the previous Section) is $93 \times 288 \times 93$ points:

- 93 points between R = 5.00 m and R = 7.00 m (ΔR = 0.0271 m)
- 288 points between $\varphi = 0$ and $\varphi = 2\pi/5$ ($R \cdot \Delta\varphi$ = 0.0218 m ... 0.03054 m)
- 93 points between z = -1.00 m and z = 1.00 m (Δz = 0.0271 m)

3.2 Calculation of Poincaré sections

A step value of $h = 0.0005$ for the Runge-Kutta method is used to calculate the fieldlines and points of Poincaré sections.
The Figure 3.1 a shows the Poincaré sections with the Poincaré puncture points at $\varphi = 0°$.

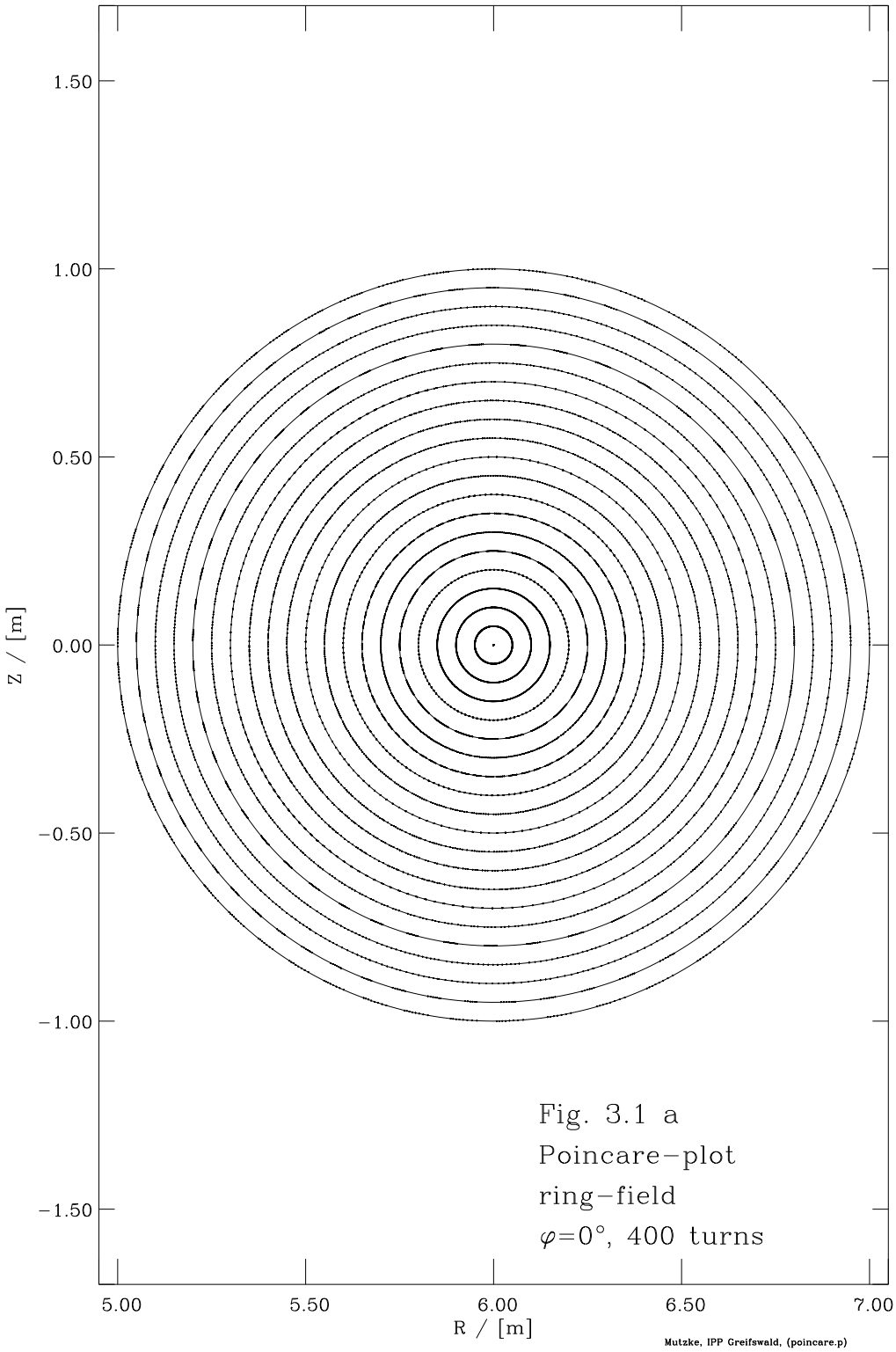

Fig. 3.1 a
Poincare−plot
ring−field
φ=0°, 400 turns

3.3 Calculation of ϑ_{real}, ι and χ

The calculation of rotational transform ι is the same as in 2.3.
If the maximum number of turns is 400 then the rotational transform ι is:

$$\iota_t(\Phi_t) = \frac{\vartheta_{real}(\Phi_t)}{\Phi_t \cdot 360^\circ} \qquad \Phi_t \ldots \text{number of toroidal turns} \tag{3.7}$$

$$\iota = \frac{1}{50} \cdot \sum_{\Phi_t=350}^{400} \iota_t(\Phi_t) \tag{3.8}$$

An approximated analytical solution is :

$$\left(\frac{1}{2} - \frac{\varrho^2}{4a^2}\right) \cdot \sqrt{R_0^2 - \varrho^2} \cdot \frac{R_0}{B_0} \approx \iota - \left(\frac{1}{4} - \frac{\varrho^2}{8a^2}\right) \cdot \frac{\varrho}{B_0 \pi} \cdot \frac{sin(2\pi\iota)}{\iota} \tag{3.9}$$

The analytical results of ι can be found only iteratively.

Figure 3.2 a shows the average angle ϑ_{real} dependent on distance to magnetic axis. The analytical approximation far from the magnetic axis is insufficient.
On the inside of calculated fieldline (400 turns) the poloidal angle has a variation in each turn, see Figure 3.3.
The condition, that all points of the Poincaré section are on a plane φ = constant, is the reason of this result.

The equation to calculate χ is also the same as in 2.3. The average value χ_m is:

$$\chi_t(\Phi_t) = \frac{\chi_{real}}{\Phi_t} \qquad \Phi_t \ldots \text{number of toroidal turns} \tag{3.10}$$

$$\chi_m = \frac{1}{50} \cdot \sum_{\Phi_t=350}^{400} \chi_t(\Phi_t) \tag{3.11}$$

The analytical solution is:

$$\chi_m = 2\pi \cdot B_0 + 2\pi \cdot \iota \cdot \varrho \cdot \left(\frac{\varrho}{2} - \frac{\varrho^3}{4a^2}\right) \cdot B_1 \tag{3.12}$$

The average values χ after 400 turns and the analytical results are shown in Figure 3.2.

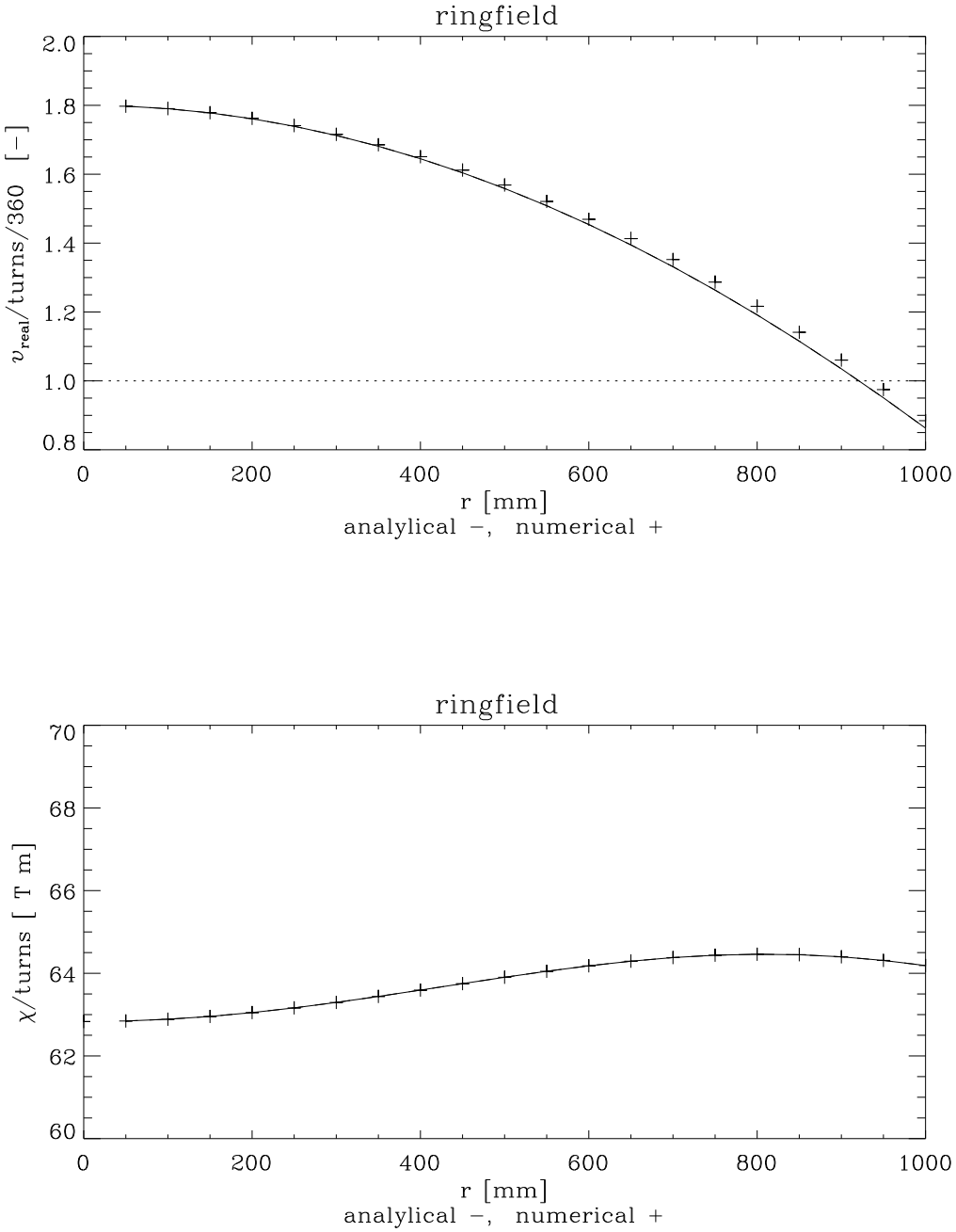

Fig. 3.2 v_{real}/turns and χ_{real}/turns ring magnetfield
step: h=0.0005, 400 turns (93x288x93, ca. 2.5cm)

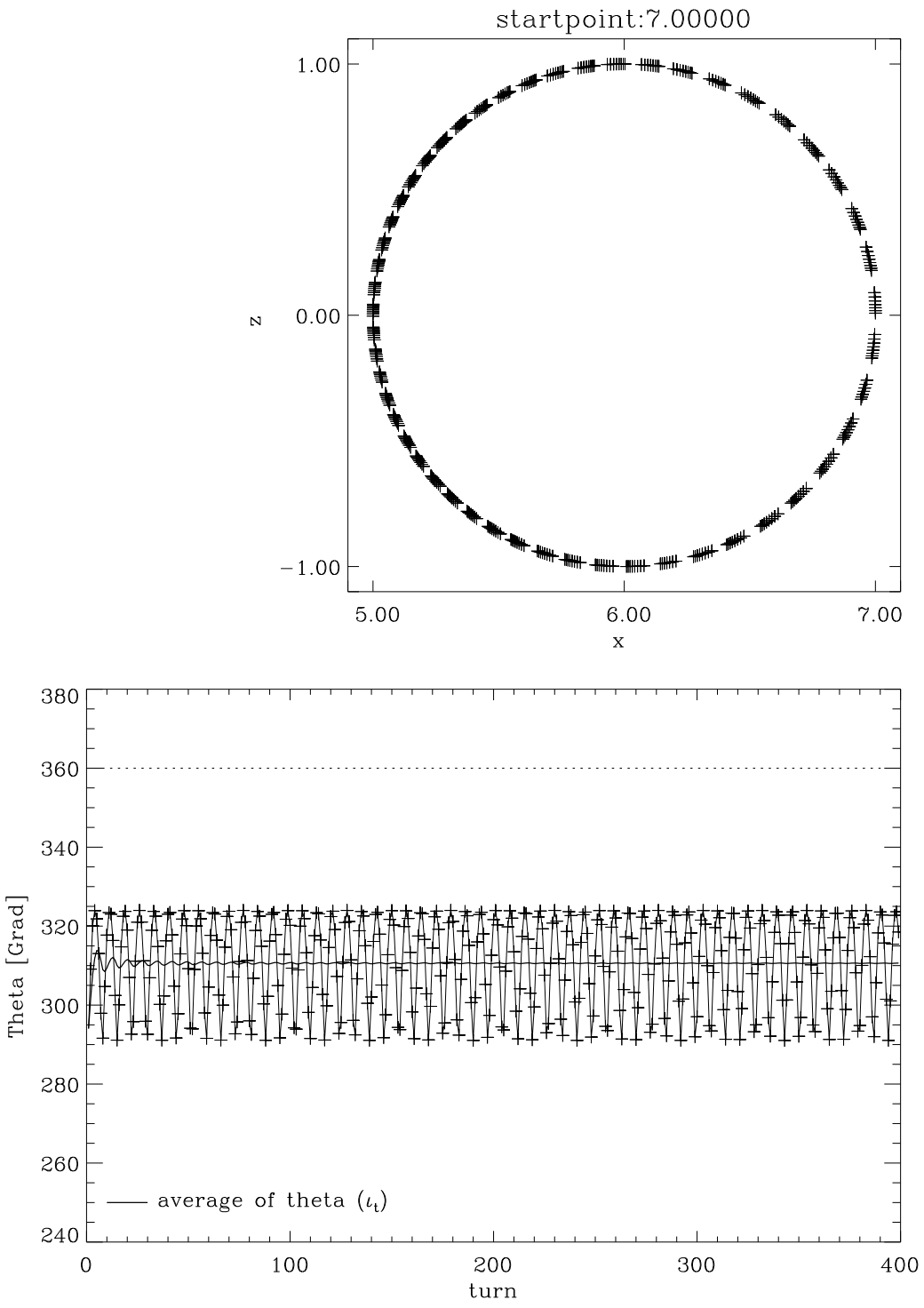

Fig. 3.3 Variation of theta per turn, $\varphi = 0°$

Step: h=0.0005, 400 turns (93x288x93, ca. 2.5 cm)

3.4 Calculation of the flux functions F_T, F'_T, F_P, F'_P and magnetic coordinate s

F_T and F_{Tr}, see also 2.4, are determined by:

$$F_T = \oint \vec{B} \cdot d\vec{A} \quad \vec{A} \ \ldots \text{ normal area to Poincaré sections} \tag{3.13}$$

$$F_{Tr} = \frac{dF_T}{dr} \tag{3.14}$$

Figure 3.5 shows the components of magnetic field B_y with Poincaré sections.
The values of $F_T(r)$ and $F_{Tr}(r)$ may be found in Figure 3.6 a. The values $r > 0$ (r^+) are the startpoint of the fieldline. The values $r < 0$ (r^-) are the second intersection of the Poincaré section with the x axis. These points are on the left side of the magnetic axis, therefore is r negative. The derivatives F_{Tr} were calculated with the help of the centred finite difference quotient (+ sign) and the derivative of a polynomial (line). Both methods to estimate the derivatives have the same accuracy in this case, see Figure 3.6 a.

The magnetic coordinate s and its derivative are calculated :

$$s = \frac{F_T}{F_T(\Psi_{sep})} \tag{3.15}$$

$$F'_T = \frac{dF_T(s)}{ds} \tag{3.16}$$

$F_T(\Psi_{sep})$ is the end value of the curve for F_T.

The analytical solution is :

$$F_T(\varrho) = 2\pi \cdot B_0 \cdot \left(R_0 - \sqrt{R_0^2 - \varrho^2} \right) \tag{3.17}$$

$$s = \frac{\left(R_0 - \sqrt{R_0^2 - \varrho^2} \right)}{\left(R_0 - \sqrt{R_0^2 - a^2} \right)} \tag{3.18}$$

$$F_T(s) = 2\pi \cdot B_0 \cdot \left(R_0 - \sqrt{R_0^2 - a^2} \right) \cdot s \tag{3.19}$$

$$F'_T = 2\pi \cdot B_0 \cdot \left(R_0 - \sqrt{R_0^2 - a^2} \right) \tag{3.20}$$

The comparison of values $F_T(s)$ and F'_T calculated with program `aam10` and the analytical solution may be found in Figure 3.6 c.

$$F_P = F_T \cdot \iota \tag{3.21}$$

$$F'_P = F'_T \cdot \iota \tag{3.22}$$

The values of $F_P(s)$ and F'_P may be found in Figure 3.6 d.
The values of rotational transform ι and χ (see Section 3.3) and their spline approximation may be found in Figure 3.6 f.
Figure 3.6 g shows the dependence of r on s. The line is the spline approximation.
Figure 3.6 g shows the comparison of value F_{Tr} dependent on s calculated with program `aam10` and analytic solution. The values are the same.

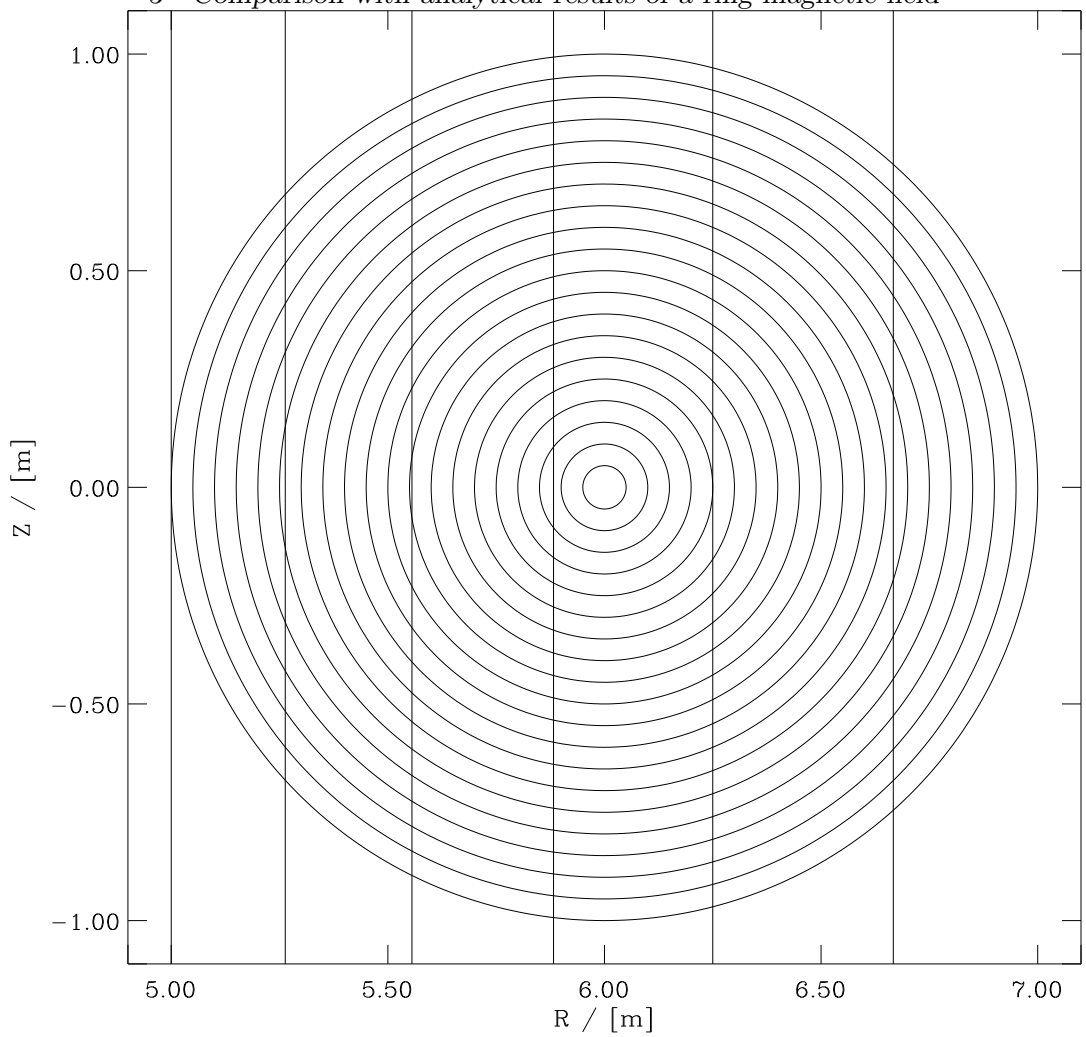

Fig. 3.5 Poincare−plots with By of vacuum magnetic field, φ =0°
Step: h=0.0005, 400 turns (resolution: 93x288x93, ca. 2.2 cm)

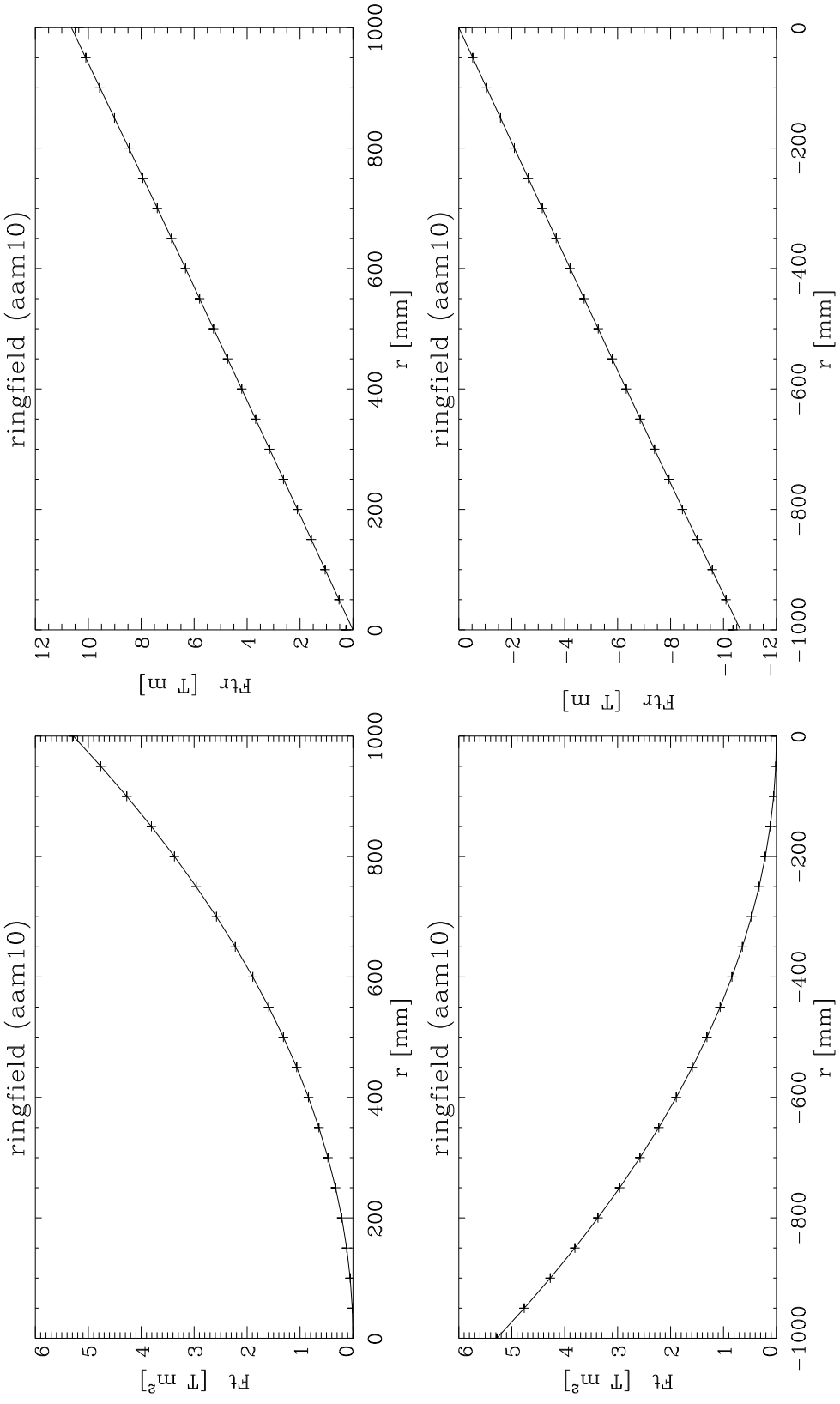

Fig. 3.6 a $\quad Ft_r = d\left(\int By\ dx\ dz\right)/dr \qquad Ft = \int By\ dx\ dz$

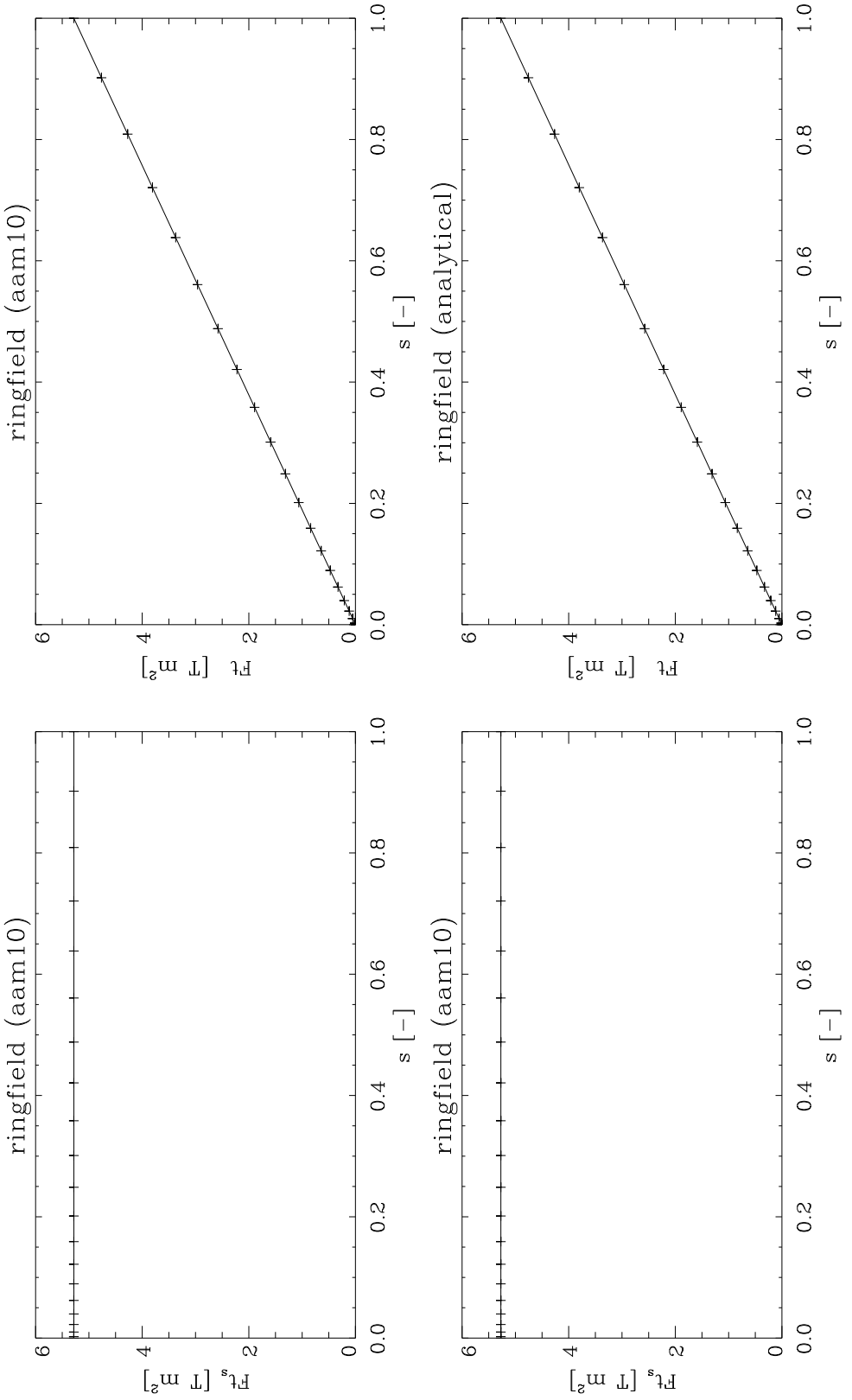

Fig. 3.6 c Compare of $Ft_s(s)$ and Ft(s)

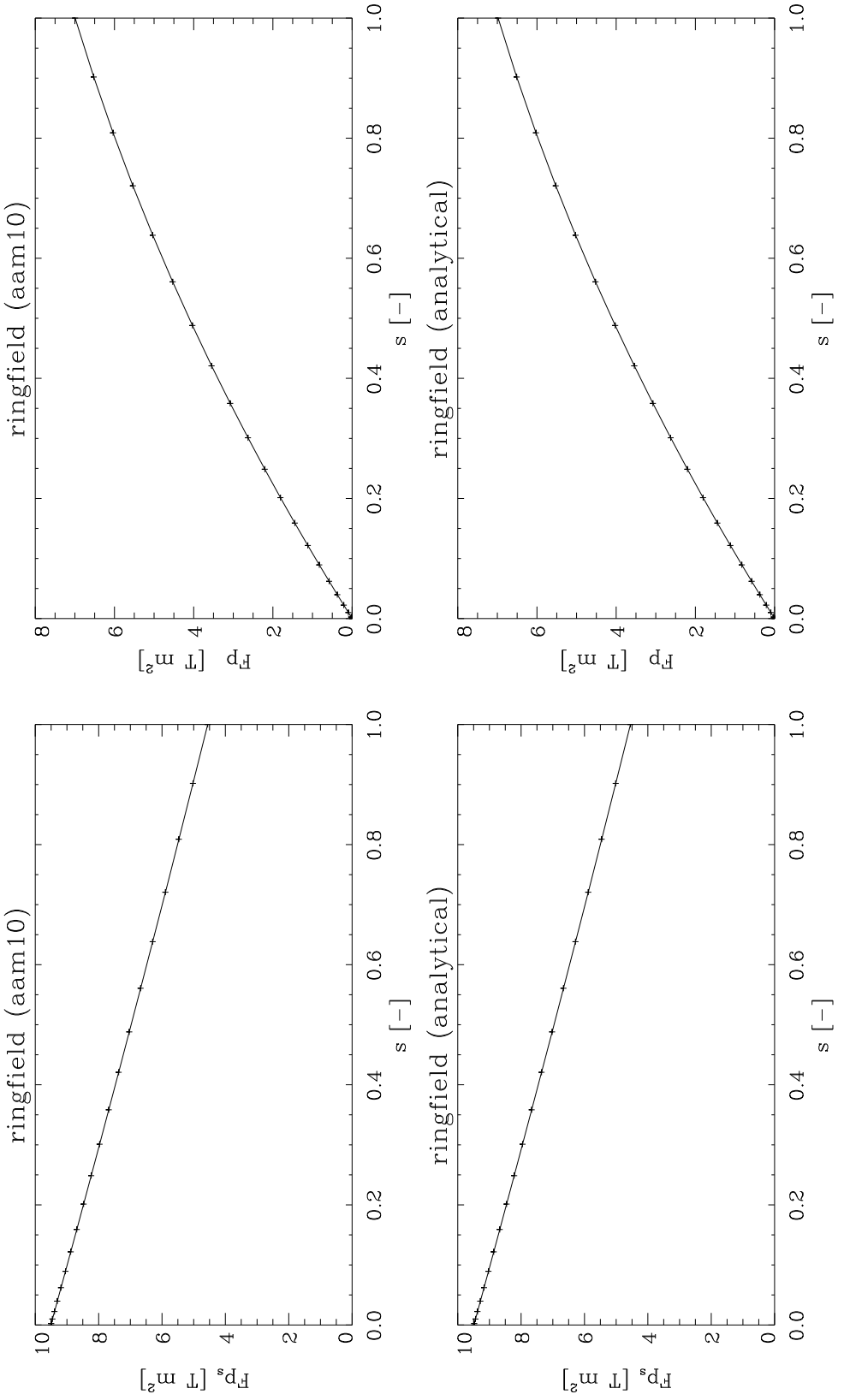

Fig. 3.6 d Compare $Fp_s(s)$ and $Fp(s)$

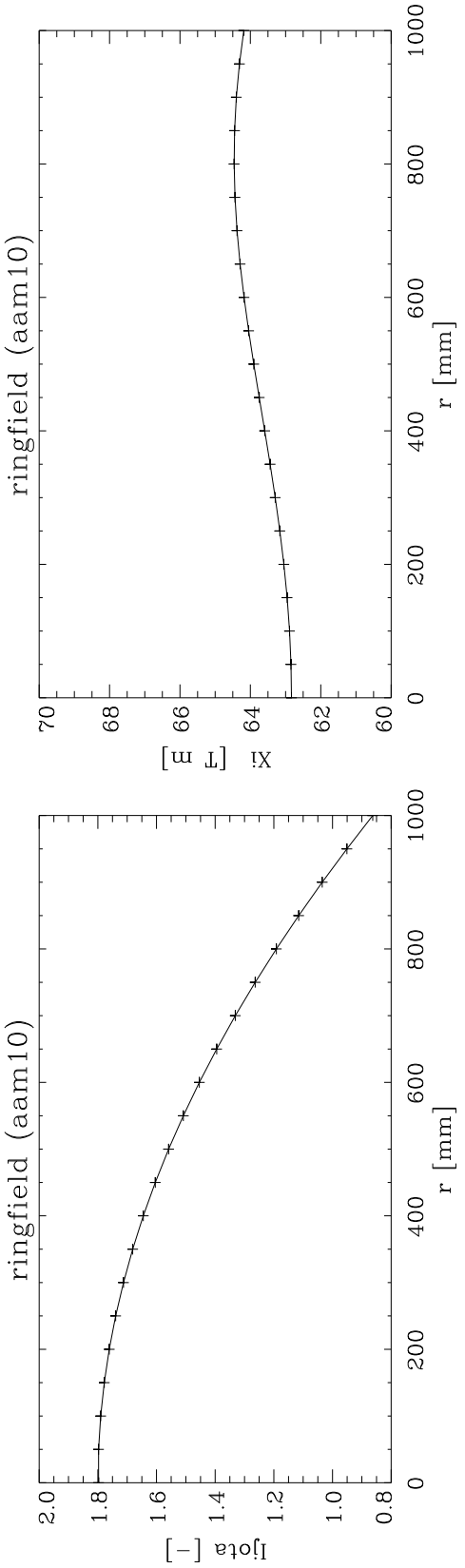

Fig. 3.6 f Ijota(r,φ=0,z=0) Xi(r,φ=0,z=0)

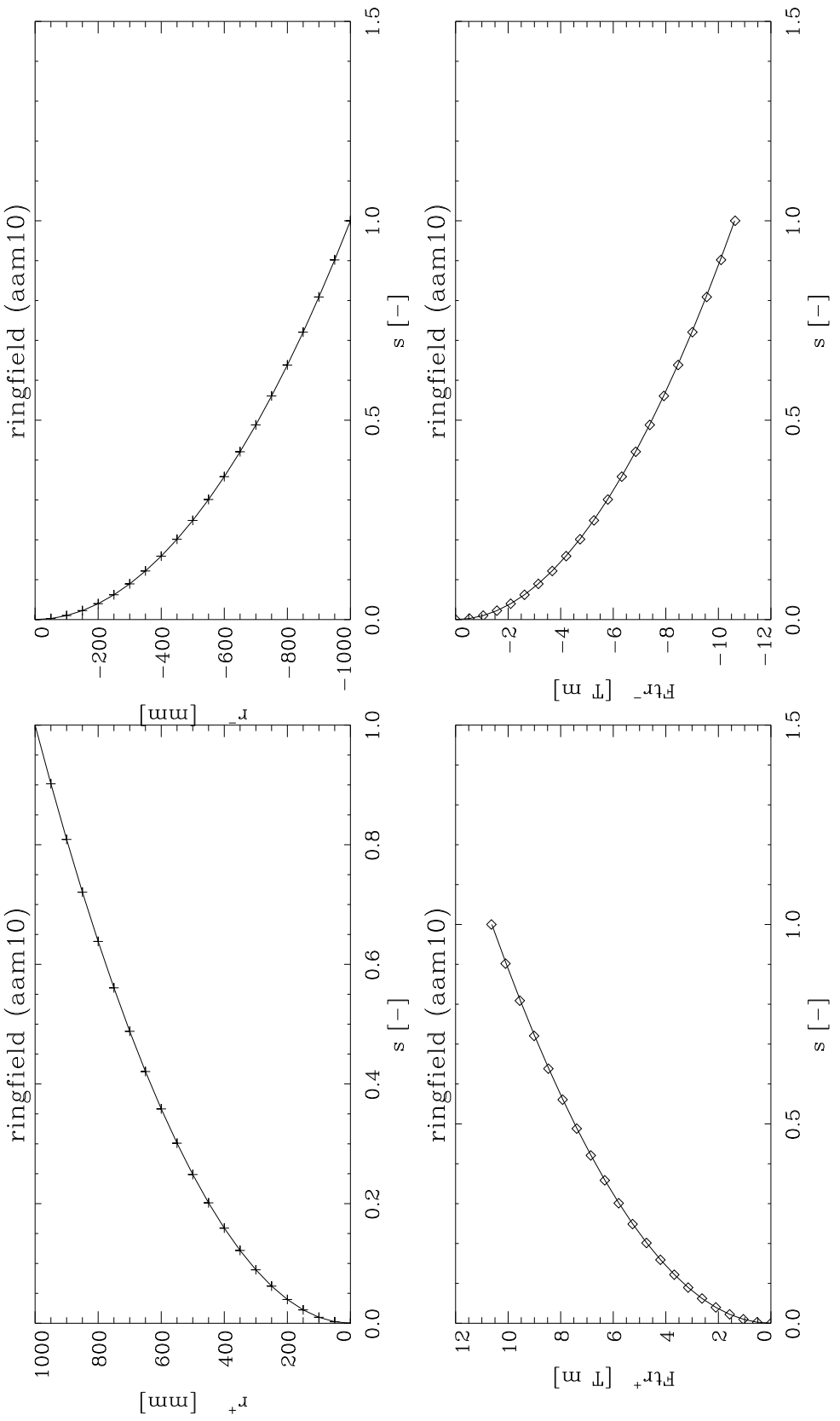

Fig. 3.6 g $r|_{\varphi=0,z=0} = f(s)|_{v=0,\phi=0}$, compare Ft_r=f(s) [analytical(–) numerical(◇)]

3.5 Compute the toroidal current J

The next step is the calculation of values toroidal current J:

$$J \cdot \mu_0 = \oint \vec{B} \cdot d\vec{\ell} \quad \vec{\ell} \ \ldots \text{ along the Poincaré section} \tag{3.23}$$

The numerical formulation is:

$$J = \frac{1}{\mu_0} \sum \left(B_x \cdot \Delta x + B_z \cdot \Delta z \right) \tag{3.24}$$

The analytical solution is :

$$J = \frac{2\pi}{\mu_0} \cdot B_1 \cdot \left(\frac{\varrho^2}{2} - \frac{\varrho^4}{4a^2} \right) \tag{3.25}$$

The components of magnetic field B_x and B_z with Poincaré sections are shown in Figure 3.7. The comparison of values J calculated with program `aam10` and the analytic solution may be found in Figure 3.8. The values of J are the same.

3.6 Compute the current I

I is a sum of 2 integrals. The total path of these integrals is closed.

$$I \cdot \mu_0 = \int \vec{B} \cdot d\vec{\ell_1} + \int \vec{B} \cdot d\vec{\ell_2} \tag{3.26}$$

ℓ_1 along the fieldline (toroidally) from start-point to the end point of one turn

ℓ_2 along the Poincaré sections (poloidally backwards) from the end point to the start point

The first integral is χ (see Section 3.3) for one turn. The second integral is a part of J (see Section 3.5).
The numerical formulation is:

$$I = \frac{1}{\mu_0} \Big[\sum \left(B_x \cdot \Delta x + B_y \cdot \Delta y + B_z \cdot \Delta z \right) \mid \ell_1 + \sum \left(B_x \cdot \Delta x + B_z \cdot \Delta z \right) \mid \ell_2 \Big]$$

The analytic solution is:

$$I = \frac{2\pi}{\mu_0} \cdot B_0 \tag{3.27}$$

Figure 3.9 shows the calculated current I. The analytical and the numerical resolution are the same.

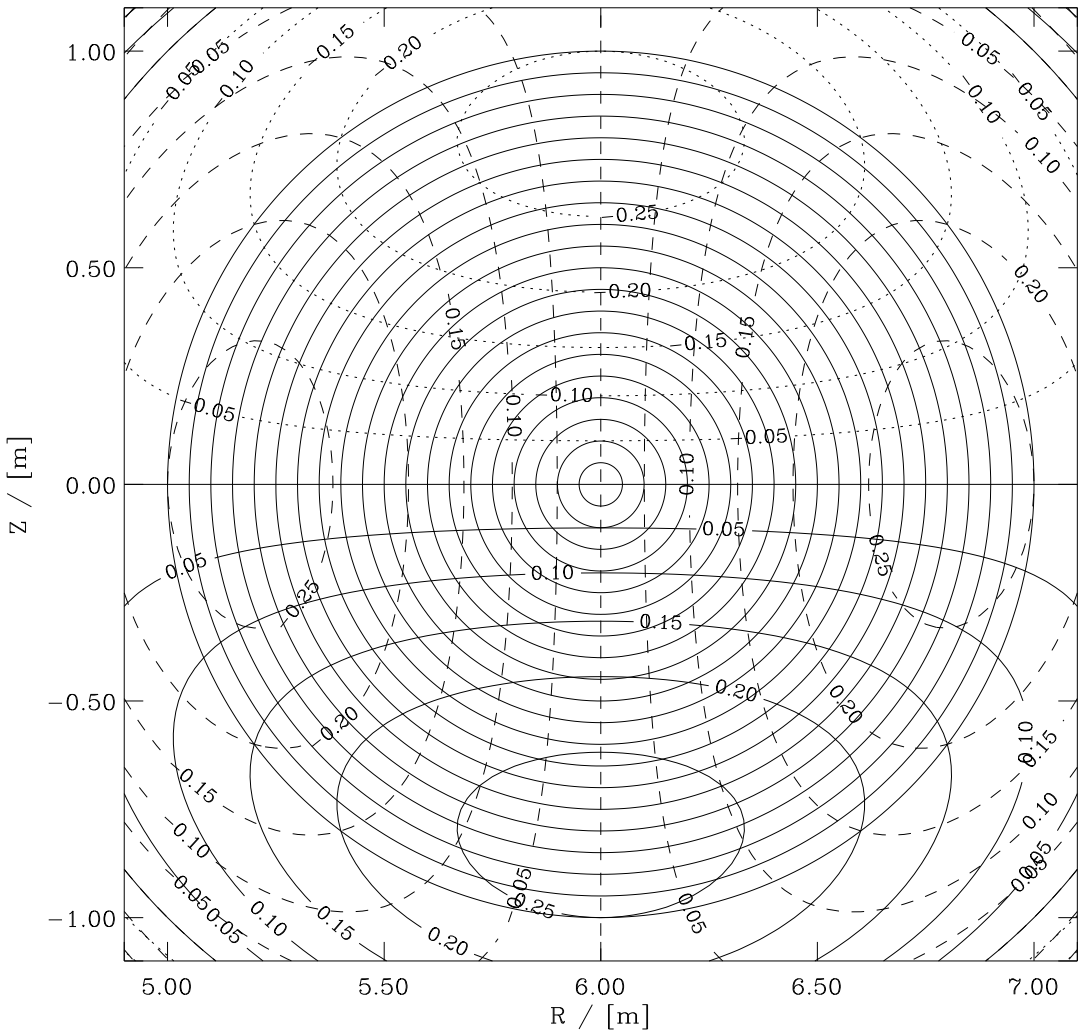

Fig. 3.7 Poincare−plots with Bx and Bz of magnetic field, φ =0°
step: h=0.0005, 400 turns (93x288x93, ca. 2.2 cm)

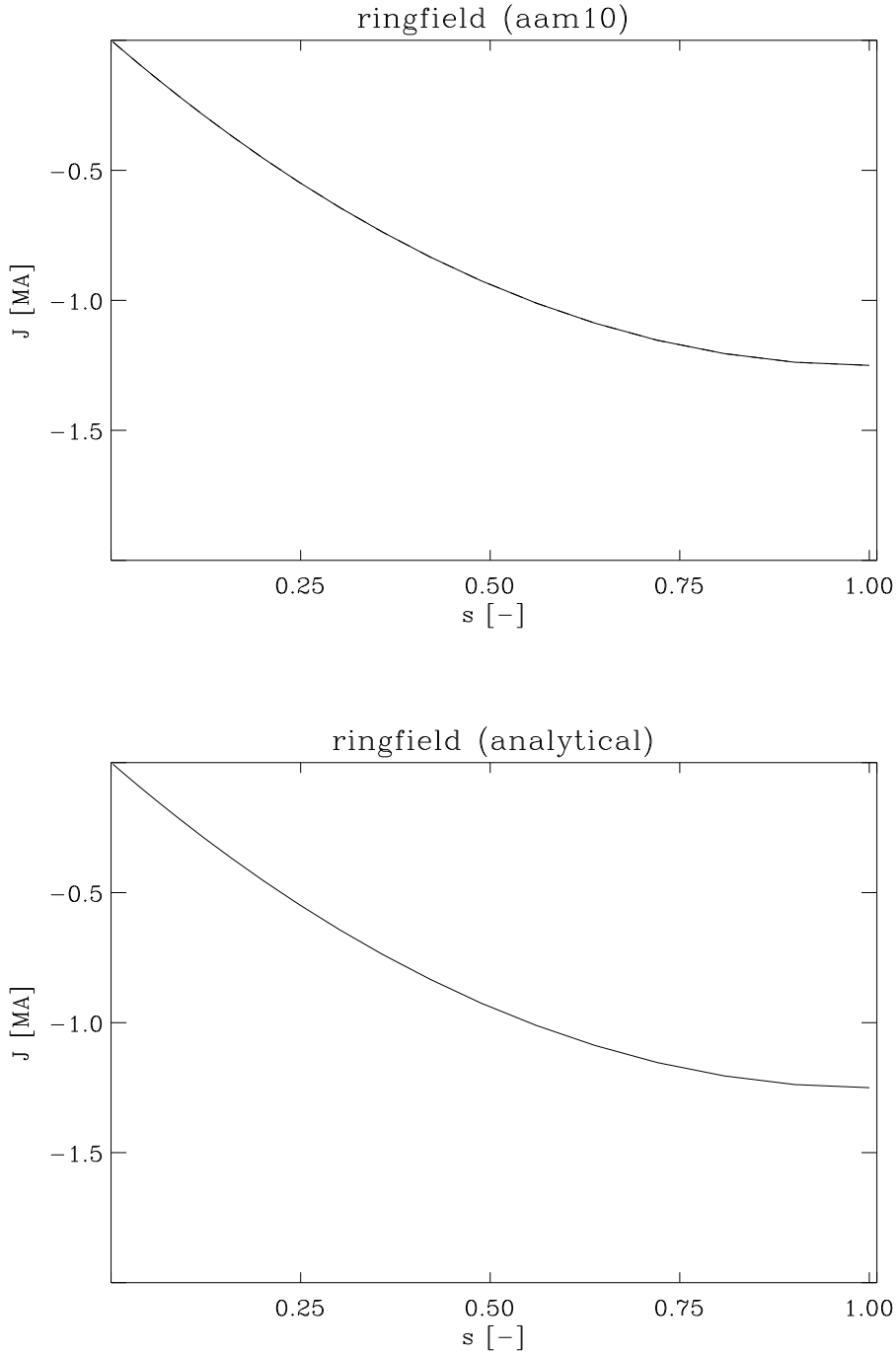

Fig. 3.8 Compare current J

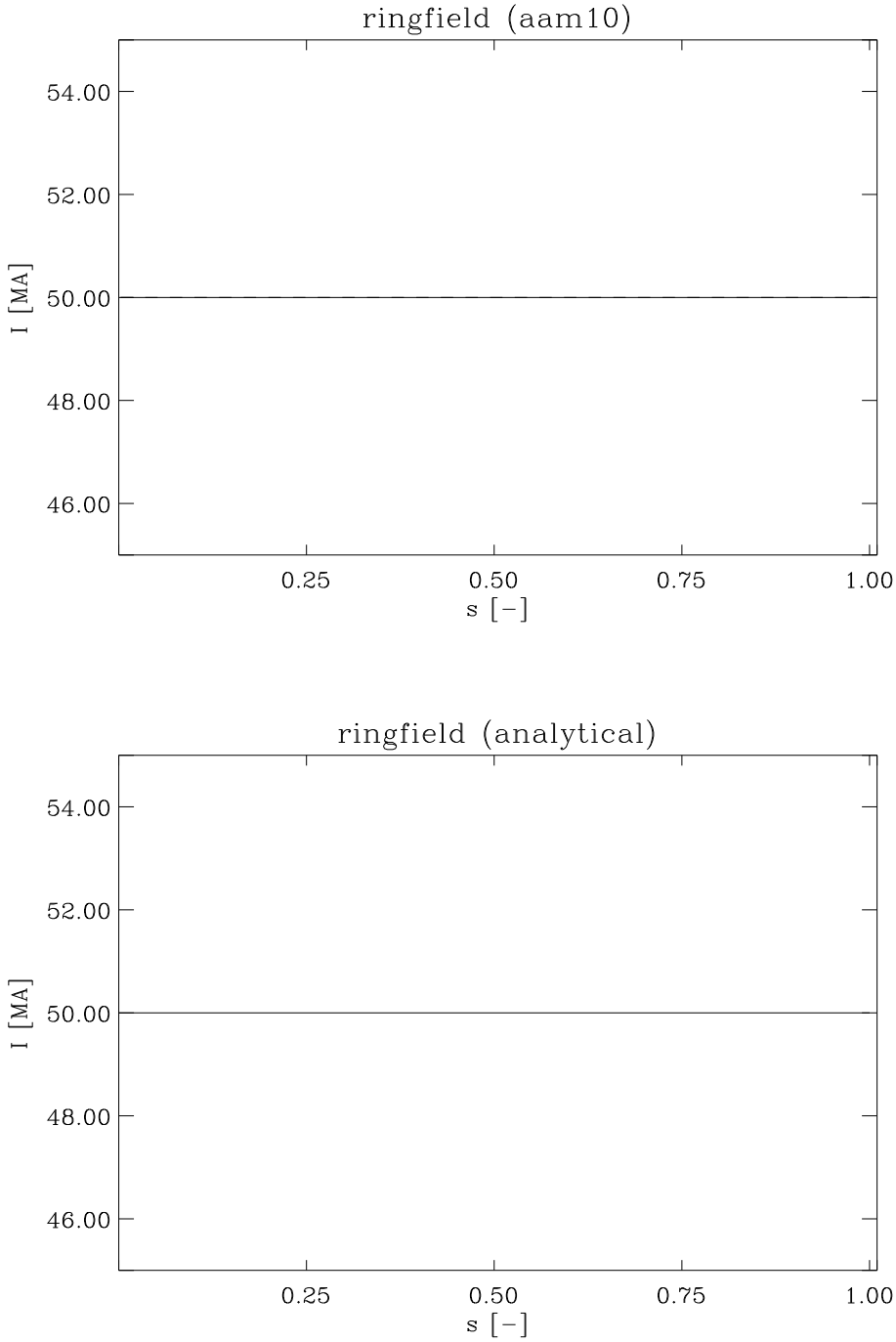

Fig. 3.9 Compare current I

3.7 Comparison of coefficient $\sqrt{g}$

The coefficient $\sqrt{g}$ is:

$$\sqrt{g}(\varphi, R, z) = \frac{[I(r_p) \cdot \mu_0 + \iota(r_p) \cdot J(r_p) \cdot \mu_0] \cdot F_T(\Psi_{sep})}{4\pi^2 \cdot B^2(\varphi, R, z)}, \tag{3.28}$$

or

$$\sqrt{g}(\vartheta, s, \Phi) = \frac{[I(s) \cdot \mu_0 + \iota(s) \cdot J(s) \cdot \mu_0] \cdot F_T(\Psi_{sep})}{4\pi^2 \cdot B^2(\vartheta, s, \Phi)}. \tag{3.29}$$

The coefficients I, J, ι, and $F_T(\Psi_{sep})$ were compared with the analytical solution. The magnetic field is given. Therefore the comparison of $\sqrt{g}$ is omitted.

3.8 Calculation of magnetic coordinates

Given is the start point in magnetic coordinates $r_p(s,\ \vartheta = 0,\ \Phi = 0)$. The equivalent real coordinates are $r_p(R,\ \varphi = 0,\ z = 0)$.
The algorithm to calculate the magnetic coordinates ϑ and Φ is:

$$\vartheta(\ell) = \frac{\iota(s) \cdot \chi(\ell)}{\mu_0 \cdot [I(s) + \iota(s) \cdot J(s)]} \pmod 1 \quad \ell \ \ldots \text{ along a fieldline} \tag{3.30}$$

$$\Phi(\ell) = \frac{\chi(\ell)}{\mu_0 \cdot [I(s) + \iota(s) \cdot J(s)]} \pmod 1 \quad \ell \ \ldots \text{ along a fieldline} \tag{3.31}$$

or

$$\vartheta(\ell) = \frac{\iota(s) \cdot \chi(\ell)}{\chi_m(s)} \pmod 1 \quad \ell \ \ldots \text{ along a fieldline} \tag{3.32}$$

$$\Phi(\ell) = \frac{\chi(\ell)}{\chi_m(s)} \pmod 1 \quad \ell \ \ldots \text{ along a fieldline} \tag{3.33}$$

Now it is possible to estimate the real coordinates R, φ and z for given magnetic coordinates s, ϑ, Φ .
To reduce the length of the fieldline it was started at two points into two directions. The start points are the intersections of Poincaré curve with x axis and the directions are towards positive φ and negative φ.
The Figures 3.14 show the points of Poincaré section at (R, z) plane, the z values dependent on ϑ and the y values dependent on ϑ. The quality of all sections is good.

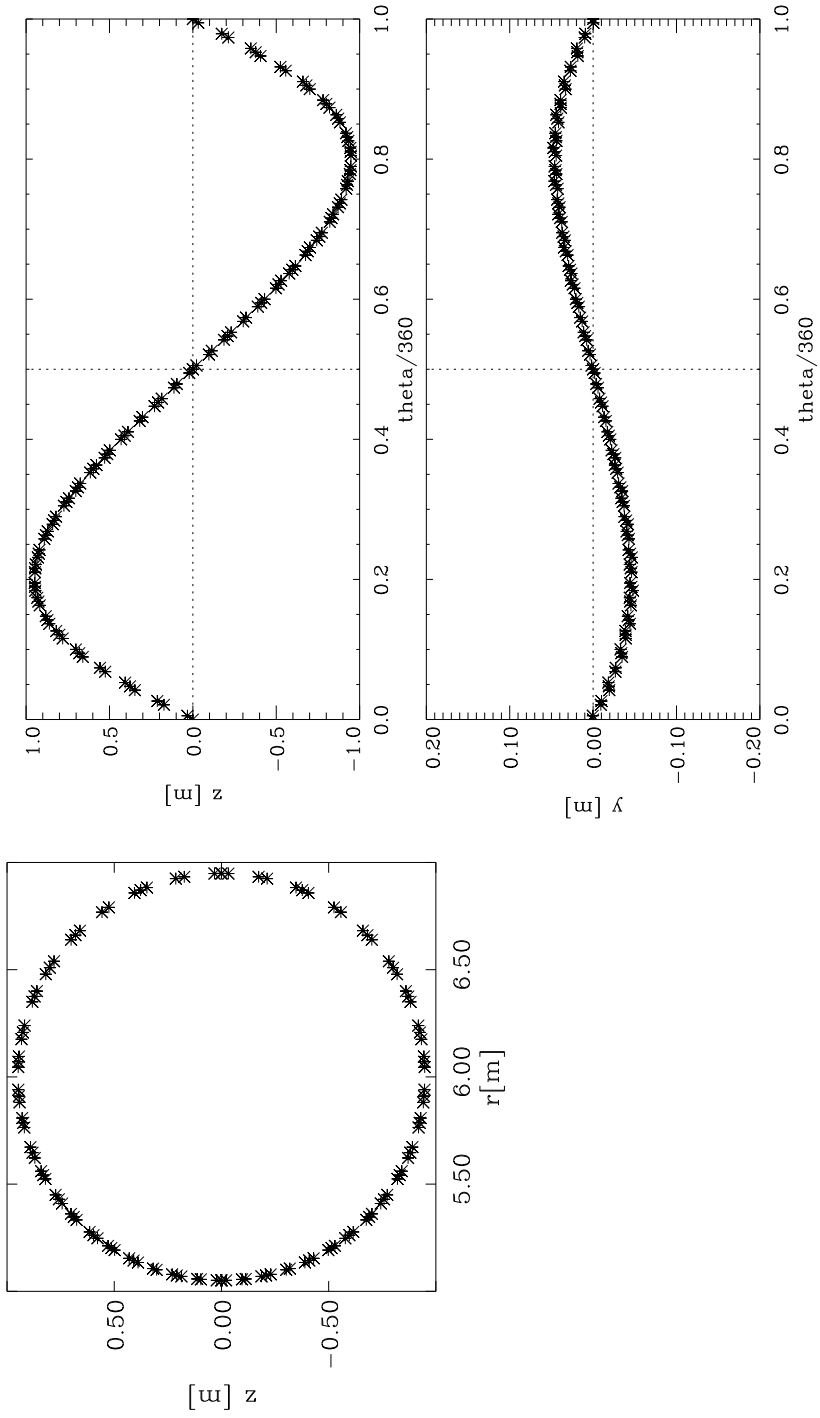

Fig. 3.14 coordinates of poincareplot z=f(r), z=f(theta), y=f(theta)

ι= 0.9526 s= 0.9000 startpoints: r_1= 6.9490m r_2= 5.0510m

3.9 Computation of ∇s and g^{ss}

We now follow the Nemov algorithm, see Section 1.11 and 1.12 , using the Clebsch description of magnetic field, see also Section 2.9

$$\vec{B} = \nabla\psi \times (\nabla\theta - \iota\nabla\zeta) \tag{3.34}$$

$$P = \frac{\partial\psi}{\partial R}, \quad Q = \frac{\partial\psi}{\partial\varphi}, \quad G = \frac{\partial\psi}{\partial z} \tag{3.35}$$

The following system of differential equations are solved:

$$\frac{dP}{d\varphi} = -\frac{R}{B_\varphi}\left(\frac{\partial B_R}{\partial R}\cdot P + \frac{\partial B_\varphi/R}{\partial R}\cdot Q + \frac{\partial B_z}{\partial R}\cdot G\right) \tag{3.36}$$

$$\frac{dQ}{d\varphi} = -\frac{R}{B_\varphi}\left(\frac{\partial B_R}{\partial \varphi}\cdot P + \frac{1}{R}\frac{\partial B_\varphi}{\partial \varphi}\cdot Q + \frac{\partial B_z}{\partial \varphi}\cdot G\right) \tag{3.37}$$

$$\frac{dG}{d\varphi} = -\frac{R}{B_\varphi}\left(\frac{\partial B_R}{\partial z}\cdot P + \frac{1}{R}\frac{\partial B_\varphi}{\partial z}\cdot Q + \frac{\partial B_z}{\partial z}\cdot G\right) \tag{3.38}$$

The initial conditions are:

$$P_0 = \frac{\partial F_T}{\partial R}, \quad Q_0 = 0, \quad G_0 = 0 \tag{3.39}$$

The values B_x, B_y, B_z and their derivatives were interpolated with the help of cubic spline method. The modified Euler method is used for the numerical solution of the system of differential equations. This is a Runge-Kutta-method second order, see 2.9.

The analytical solution is :

$$P = 2\pi\cdot B_0\cdot\frac{R-R_0}{\sqrt{R_0^2 - z^2 - (R-R_0)^2}} \tag{3.40}$$

$$Q = 0 \tag{3.41}$$

$$G = 2\pi\cdot B_0\cdot\frac{z}{\sqrt{R_0^2 - z^2 - (R-R_0)^2}} \tag{3.42}$$

The analytical coefficient g^{ss} is:

$$g^{ss} = |\nabla s|^2 = \frac{P^2 + (Q/R)^2 + G^2}{F_T(\Psi_{sep})^2} = \frac{\varrho^2}{\left(R_0^2 - \varrho^2\right)\left(R_0 - \sqrt{R_0^2 - a^2}\right)^2}. \tag{3.43}$$

Figures 3.15 and 3.16 show the analytical solutions and the numerical results (asterisks) of P, Q, G and g^{ss} at $s = 0.9$. Figure 3.17 shows all results of g^{ss}. The numerical and the analytical results are the same.

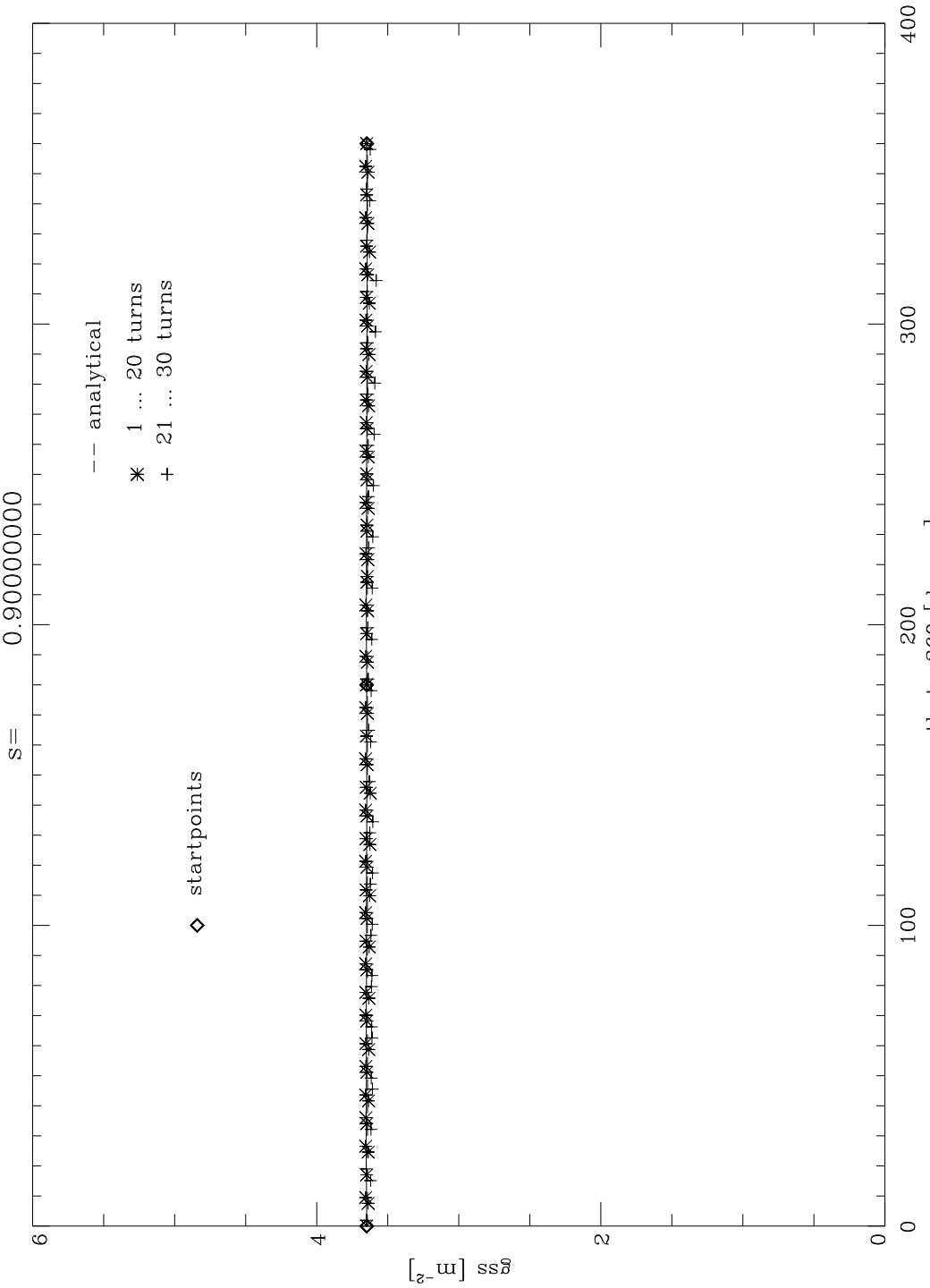

Fig 3.15 gss $[m^{-2}]$ ring field s=0.9000

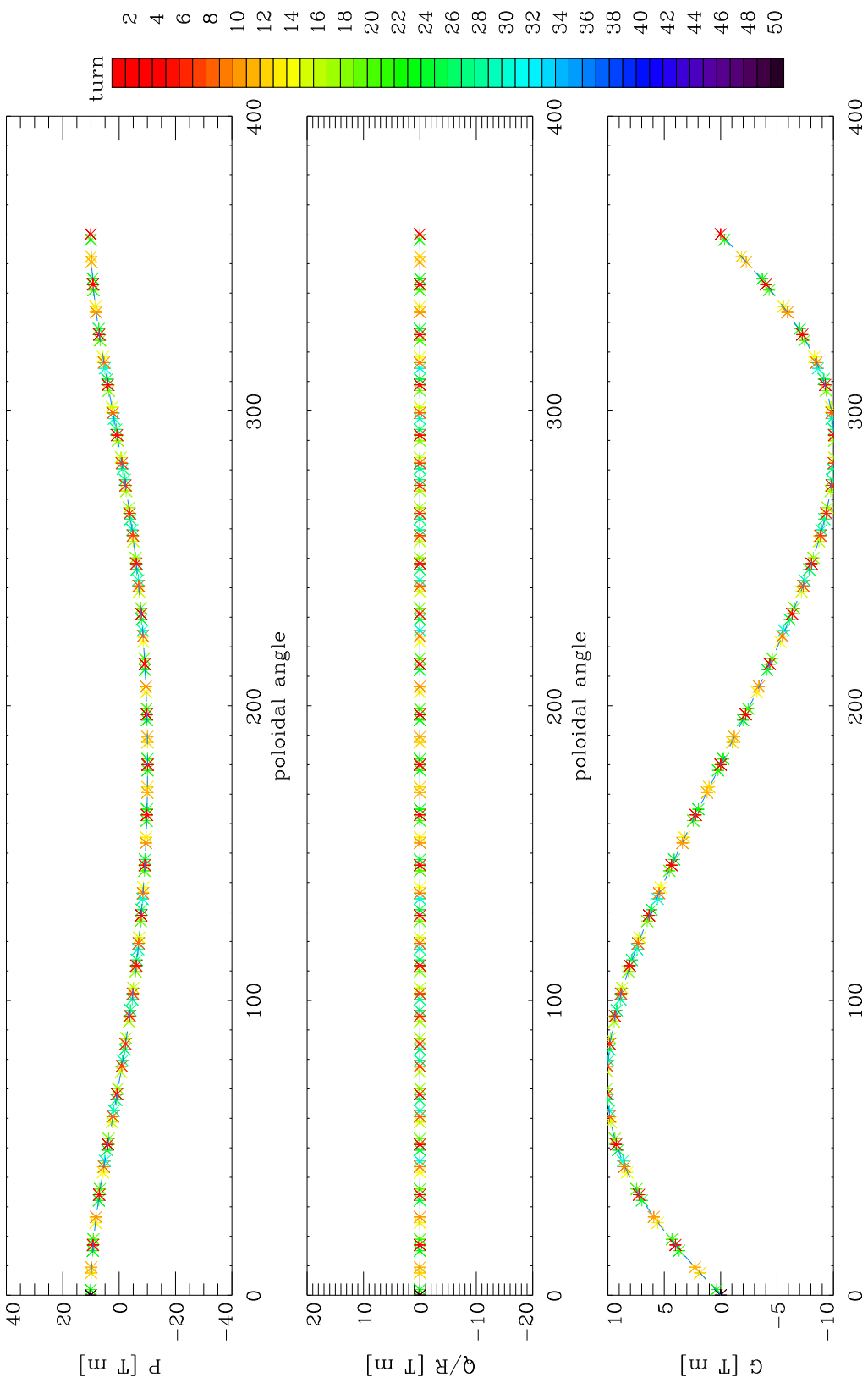

Fig 3.16 P Q and G, ring field, blue analytical

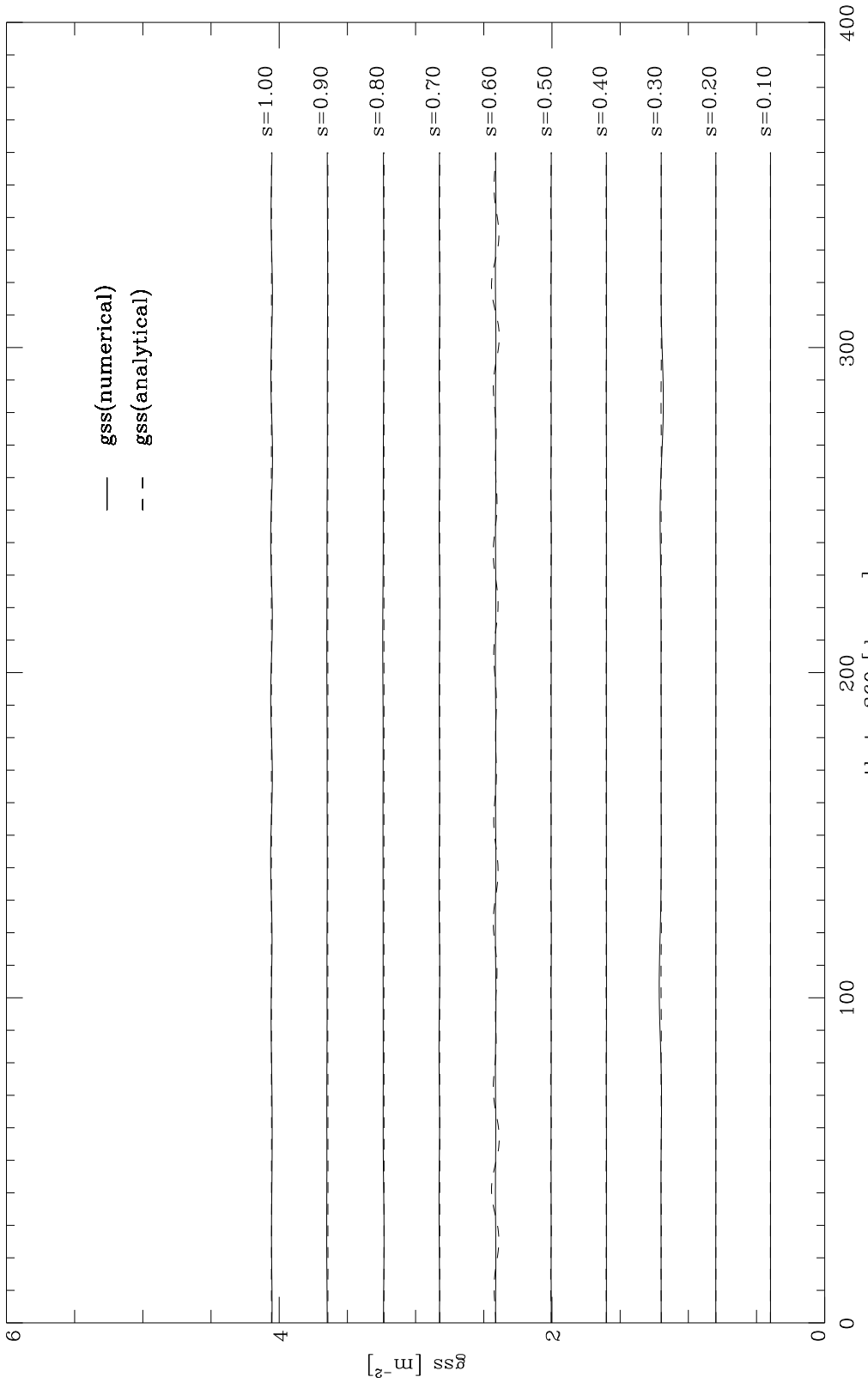

Fig 3.17 g^{ss} $[m^{-2}]$ ϕ=0 ring field

4 Units of physical terms

$$
\begin{aligned}
\mu_0 &= 1.256637 \cdot 10^{-6}\ \frac{V \cdot s}{A \cdot m} = 1.256637 \cdot 10^{-6}\ \frac{T}{A} \cdot m = 4\pi \cdot 10^{-7}\ \frac{T}{A} \cdot m \\
[B] &= T = \frac{V \cdot s}{m^2} \\
[\ell] &= m \\
[F_T] &= T \cdot m^2 = \frac{V \cdot s}{m^2} \cdot m^2 = V \cdot s \\
[F_{Tr}] &= T \cdot m \\
[F'_T] &= T \cdot m^2 \\
[F_P] &= T \cdot m^2 \\
[F'_P] &= T \cdot m^2 \\
[J \cdot \mu_0] &= T \cdot m = \frac{V \cdot s}{m^2} \cdot m = \frac{V \cdot s}{m} \\
[I \cdot \mu_0] &= T \cdot m = \frac{V \cdot s}{m^2} \cdot m = \frac{V \cdot s}{m} \\
[J] &= T \cdot m \cdot \frac{A \cdot m}{V \cdot s} = \frac{V \cdot s}{m^2} \cdot m \cdot \frac{A \cdot m}{V \cdot s} = A \\
[I] &= T \cdot m \cdot \frac{A \cdot m}{V \cdot s} = \frac{V \cdot s}{m^2} \cdot m \cdot \frac{A \cdot m}{V \cdot s} = A \\
[\sqrt{g}] &= \frac{(T \cdot m) \cdot (T \cdot m^2)}{T^2} = m^3 \\
[P] &= T \cdot m \\
[Q] &= T \cdot m^2 \\
[G] &= T \cdot m \\
[g^{ss}] &= \frac{1}{T^2 \cdot m^4} \cdot \left(T^2 \cdot m^2 + \frac{T^2 \cdot m^4}{m^2} + T^2 \cdot m^2 \right) = \frac{1}{m^2} \\
[\tilde{\sigma}] &= - \\
[\tilde{\beta}] &= T \cdot m \\
[g_{s\vartheta}] &= m^2 \\
[g^{\phi s}] &= \frac{1}{m^2} \\
[g^{\vartheta s}] &= \frac{1}{m^2}
\end{aligned}
$$

5 Acknowledgements

We would like to thank Dr. C. Nührenberg for providing and detailing the `VMEC` calculation for the W7–X vacuum field. Helpful discussions with Drs. H. Wobig and A. Boozer are also gratefully acknowledged.

References

[1] M. Borchardt, A. Mutzke, J. Nührenberg, J. Riemann, R. Schneider, S. Weber, *Towards a 3-D Plasma Fluid Modelling for the W7–X Divertor*, Proc. 26^{th} EPS Conf. Control. Fusion and Plasma Phys., Maastrich 1999, ECA **23** J, Phys. Soc., Geneva 1999, 1501–1504.

[2] V.V. Nemov, *Calculations of the Magnetic Surface Function Gradient and Associated Quantities in a Torsatron*, Nuclear Fusion **28** (1988) 1727–1736.

[3] X. Bonnin, *Magnetic coordinates algorithm*, work report, IPP-Greifswald (2000), unpublished.

[4] A. Mutzke, *Bestimmung von Poincaré Plots aus gegebenen Magnetfeldern*, work report, IPP-Greifswald (1999), unpublished.